Technical Report Documentation Page

1. REPORT No.
FHWA/CA/ESC-99/13

2. GOVERNMENT ACCESSION No.

3. RECIPIENT'S CATALOG No.

4. TITLE AND SUBTITLE
Non-Destructive Estimate of the Rate of Change of Structural Degradation of the Lavic Road Overcrossing

5. REPORT DATE
October 1999

6. PERFORMING ORGANIZATION

7. AUTHOR(S)
N. Stubbs, S. Park, R.W. Bolton, S. Choi, and C. Sikorsky

8. PERFORMING ORGANIZATION REPORT No.
FHWA/CA/ESC/TEES 1-9/99

9. PERFORMING ORGANIZATION NAME AND ADDRESS
Texas Engineering Experimental Station
College Station, Texas 77843

10. WORK UNIT No.

11. CONTRACT OR GRANT No.
59A0022

12. SPONSORING AGENCY NAME AND ADDRESS
California Department of Transportation,
Engineering Service Center

13. TYPE OF REPORT & PERIOD COVERED
Final 6/1/97 - 10/30/98

14. SPONSORING AGENCY CODE

15. SUPPLEMENTARY NOTES

16. ABSTRACT

The objective of this study is to quantitatively evaluate, using recent work in nondestructive damage evaluation (NDE) and systems identification at Caltrans, the rate of possible structural stiffness deterioration of the Lavic Road Overcrossing (Bridge #54 -734). The structure is suspected of having being constructed with reactive aggregates. To meet this objective, the following eight tasks were performed. First, a modal test was performed on the bridge in December 1997. Second, a modal analysis was performed on the test data and selected modal parameters of the bridge were extracted. Third, a 3-dimensional finite element model of the superstructure and substructure of the bridge was developed. Fourth, using the finite element model and the frequency modal parameters extracted from the field data, baseline modal parameters for the bridge and mass and elastic parameters of the deck, column, and abutments were generated. Fifth, using the field modal parameters and the baseline modal parameters, potential damage in the structure at the member level was localized. Sixth, using the field modal parameters and a knowledge of the location of damage, a damage severity was assigned to each of the identified members. Seventh, using the location and severity of the damage along with the baseline model, the detailed structural properties of the existing bridge were estimated. Finally, each of the previous seven tasks were repeated nine months later (September 1998) and the magnitude of deterioration of the structural members was quantified for the elapsed period of time.

17. KEYWORDS
modal parameter, systems identification, nondestructive damage evaluation, estimation of structural properties

18. No. OF PAGES:
152

19. DRI WEBSITE LINK
http://www.dot.ca.gov/hq/research/researchreports/1997-2001/overcrossing.pdf

20. FILE NAME
overcrossing.pdf

Technical Report Documentation Page

1. Report No.	2. Government Accession No.	3. Recipient's Catalog No.
FHWA/CA/ESC-99/13		

4. Title and Subtitle	5. Report Date
Non-Destructive Estimate of the Rate of Change of Structural Degradation of the Lavic Road Overcrossing	October 1999
	6. Performing Organization Code
7. Author's	8. Performing Organization Report No.
N. Stubbs, S. Park, R.W. Bolton, S. Choi, and C. Sikorsky	FHWA/CA/ESC/TEES 1-9/99
9. Performing Organization Name and Address	10. Work Unit No. (TRAIS)
Texas Engineering Experimental Station College Station, Texas 77843	11. Contract or Grant No. 59A0022
	13. Type of Report and Period Covered
12. Sponsoring Agency Name and Address	FINAL 6/1/97 - 10/30/98
California Department of Transportation, Engineering Service Center 1801 30th Street, Sacramento, CA 95816	14. Sponsoring Agency Code -F 97 SD 06

15. Supplementary Notes

16. Abstract

The objective of this study is to quantitatively evaluate, using recent work in nondestructive damage evaluation (NDE) and systems identification at Caltrans, the rate of possible structural stiffness deterioration of the Lavic Road Overcrossing (Bridge #54-734). The structure is suspected of having being constructed with reactive aggregates. To meet this objective, the following eight tasks were performed. First, a modal test was performed on the bridge in December 1997. Second, a modal analysis was performed on the test data and selected modal parameters of the bridge were extracted. Third, a 3-dimensional finite element model of the superstructure and substructure of the bridge was developed. Fourth, using the finite element model and the frequency modal parameters extracted from the field data, baseline modal parameters for the bridge and mass and elastic parameters of the deck, column, and abutments were generated. Fifth, using the field modal parameters and the baseline modal parameters, potential damage in the structure at the member level was localized. Sixth, using the field modal parameters and a knowledge of the location of damage, a damage severity was assigned to each of the identified members. Seventh, using the location and severity of the damage along with the baseline model, the detailed structural properties of the existing bridge were estimated. Finally, each of the previous seven tasks were repeated nine months later (September 1998) and the magnitude of deterioration of the structural members was quantified for the elapsed period of time.

17. Key Words	18. Distribution Statement
modal parameter, systems identification, nondestructive damage evaluation, estimation of structural properties	No restrictions. This document is available to the public through the National Technical Information Service, Springfield, Virginia 22161

19. Security Classif. (of this report)	20. Security Classif. (of this page)	21. No. of Pages	22. Price
Unclassified	Unclassified	147	

DISCLAIMER: The opinions, findings, and conclusions expressed in this publication are those of the authors and not necessarily those of the STATE OF CALIFORNIA

TABLE OF CONTENTS

LIST OF TABLES

LIST OF FIGURES

FIGURE Page

1. INTRODUCTION

1.1 Objectives and Methodology

The objective of this study is to quantitatively evaluate, using recent work in nondestructive damage evaluation (NDE) and systems identification at Caltrans, the rate of possible structural stiffness deterioration of the Lavic Road Overcrossing (Bridge #54-734). The structure is suspected of having been constructed with reactive aggregates. To meet this objective, the following eight tasks were performed. First, a modal test was performed on the bridge in December 1997. Second, a modal analysis was performed on the test data and selected modal parameters of the bridge were extracted. Third, a 3-dimensional finite element model of the superstructure and substructure of the bridge was developed. Fourth, using the finite element model and the frequency modal parameters extracted from the field data, baseline modal parameters for the bridge and mass and elastic parameters of the deck, column, and abutments were generated. Fifth, using the field modal parameters and the baseline modal parameters, potential damage in the structure at the member level was localized. Sixth, using the field modal parameters and a knowledge of the location of damage, a damage severity was assigned to each of the identified members. Seventh, using the location and severity of the damage along with the baseline model, the detailed structural properties of the existing bridge were estimated. Finally, each of the previous seven tasks were repeated nine months later (September 1998) and the magnitude of deterioration during that period of time of structural members was quantified.

1.2 Organization of the Report

The remainder of the report is organized into six (6) sections. In Section 2, a brief description of the structure is presented. In Section 3, the estimation of the

structural stiffness properties of the existing structure as of December 1997 is described. In Section 4, the estimation of the structural stiffness properties of the existing structure as of September 1998 is next described. In Section 5, estimates are made of the rate of deterioration of the structural stiffness of various portions of the structure. In Section 6, other evidence to corroborate the predictions of NDE and systems identification is discussed. Finally, in Section 7, the major findings of the study are summarized.

2. DESCRIPTION OF THE STRUCTURE

The Lavic Road Overcrossing (Bridge #54-734) is located in San Bernardino County, California and passes over Interstate I-40 approximately 7 miles west of the town of Ludlow. The structure was completed in 1968. The general layout of the structure is shown in Figure 2.1. The structure is oriented in a North-South direction and spans the four-lane interstate highway. The south span is 123 ft. long while the north span is 118 ft. long. The superstructure is a 7 ft. deep reinforced concrete triple box girder which includes a 34 ft. wide deck (including overhangs) and four 8-inch wide webs spaced at 8 ft. 9 inches. The structure is supported at the South end by Abutment #1 and at the North end by Abutment #3. The bridge is supported approximately at mid-span by Bent #2 which consists of a 5 ft. diameter column which in turn is supported on a spread footing resting on sand. The abutments essentially consist of a end diaphragm supported by a beam resting on a strip footing. Details of Bent #2 and Abutments #1 and #3 are provided in Figure 2.2.

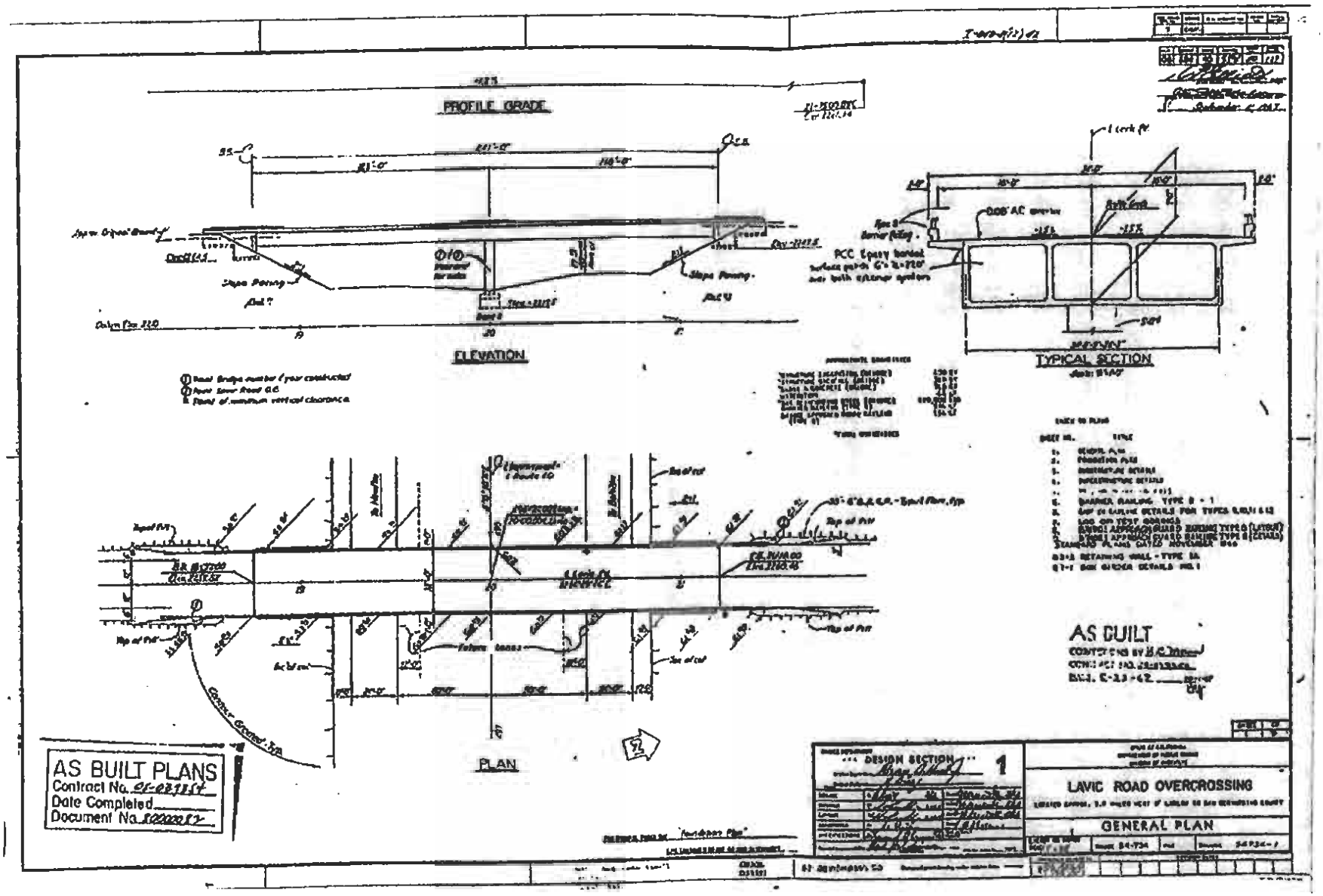

Figure 2.1 General Plan of Lavic Road Overcrossing

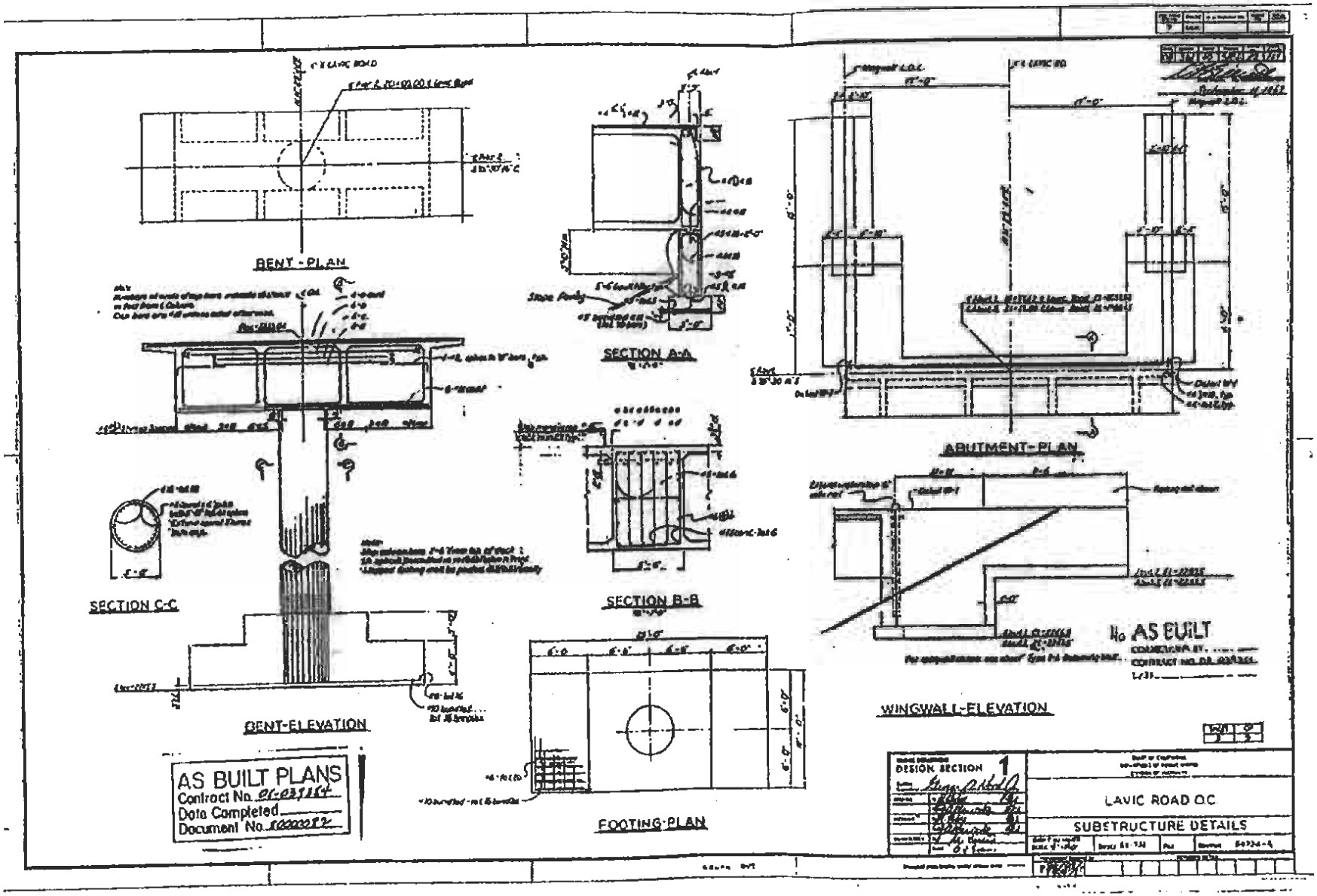

Figure 2.2 Details of Bent and Abutment

3. IDENTIFICATION OF THE EXISTING STRUCTURE AS OF DECEMBER 1997

3.1 Overview

The objective of this section is to generate an estimate of the appropriate stiffness properties of the Lavic Road Overcrossing with the field measurements taken on 22 December 1997. By appropriate stiffness properties we mean the various geometric parameters and material properties that a structural engineer would need to perform a static or dynamic analysis of the structure. Geometric parameters of interest here include cross sectional areas and second moment of areas of sections. Material properties include the effective modulus of elasticity of the structural members and the equivalent one-dimensional spring stiffnesses that model the abutments or soil-structure interaction.

A schematic of the approach used here to develop the stiffness properties of the existing structure is shown in Figure 3.1. The modal parameters of the existing structure are combined with information provided on as-built plans of the structure and a sensitivity-based systems identification (SID) procedure to generate a set of modal parameters for an idealized pristine (baseline/as-built) structure. The measured modal parameters of the existing structure and the theoretically-generated modal parameters of the pristine structure are used in combination with a proven damage detection method to generate possible locations and severity of damage in the existing structure relative to the pristine structure. Finally, by combining the location and severity of the damage in the existing structure with the pristine structure using a simple updating algorithm, the stiffness properties of the existing structure are identified. These properties can now be used to analyze the response of the existing structure. Note that the systems identification technique and the damage detection scheme mentioned above have been described in great detail elsewhere [Stubbs and Kim (1996),

Stubbs et al. (1992)]. For the convenience of the readers, summaries of these approaches are provided in Appendix A.

3.2 Summary of Modal Analysis

A modal test was performed on the Lavic Road Overcrossing on 22 December 1997. When the vibration measurements were made, temperatures ranged from a low of 40 degrees Fahrenheit to a high of 50 degrees Fahrenheit and no significant wind was observed. The objective of the field testing was to extract at least three of the lower modes of the structure. For each mode, we desired an estimate of the frequency as well as a description of the mode shape. The apparatus used in the modal test consisted of an eight-channel signal analyzer, seven accelerometers, an impact hammer, and a commercial software package to perform the modal analysis. The accelerometer layout for the test is shown in Figure 3.2. The responses of the structure were measured at 30 locations: 26 locations on the deck (E1-E13 and W1-W13) and 4 locations on the column (C1-C4). For all readings, the structure was impacted in the Z-direction using a specially designed instrumented hammer at the midpoint between accelerometers E3 and E4.

Acceleration responses in the Y- and Z-directions were recorded at locations W1-W13. Only responses in the Z-direction were taken at locations E1-E13. Responses were taken in the X- and Y-directions at locations C1-C4. A standard modal analysis was performed on the collected data and resonant frequencies and mode shapes were extracted. A detailed description of the field testing and the modal analysis are provided in the Appendix B.

Although many modes were available, only the lower five modes were selected from the measurements in December 1997. These modes were earlier identified in an accompanying finite element model of the structure. The details of the finite element model are provided in the next section. The selected modes can

be described as follows: (1) the first bending mode of the deck about the Y-axis; (2) the first lateral bending mode of the deck about the Z-axis; (3) the second bending mode of the deck about the Y-axis; (4) the first torsional mode of the deck about the X-axis; and (5) the second lateral bending mode of the deck about the Z-axis. The frequencies associated with these modes are listed in Table 3.1.

The modal amplitudes of these modes at each accelerometer location are listed in Tables 3.2 to 3.6. Note that visualizations of the modes are provided in Figures 3.3 to 3.7.

3.3 Development of the Baseline Model

Since only modal parameters of the existing structure are available, the first problem is to generate an estimate of the baseline structure. To develop such a baseline model, a finite element (FE) model of the reinforced concrete box girder bridge was developed (ABAQUS 1994). A schematic of the FE model for the bridge is shown in Figure 3.8. The flanges, webs, and diaphragms of the deck were modeled using 976 plate elements. Bent #2 was modeled using 240 brick elements. Abutment #1 (south end) and Abutment #3 (north end) were modeled in the following manner. Each abutment system was modeled using four vertical axial springs in the Z-direction and four horizontal axial springs in the Y-direction (See Figure 3.9). These springs represent the behavior of abutment and the soil-structure interaction between the abutment and the soil. The dimensions of Bent #2 were taken from the as-built plans (Figure 2.2) and the soil-structure interaction between the footing of the column and the soil was modeled using a total of 105 axial springs (35 in the X-direction, 35 in the Y-direction, and 35 in the Z-direction) [See Figure 3.8]. In all the FE model contained 5925 degrees of freedom.

To develop the baseline model, each member of the FE model shown in Figure 3.8 was assigned to one of three groups: Group 1, which included all elements in the deck; Group 2, which included the column and footing of Bent #2;

and Group 3, which included the abutment-soil systems. Note that even though the elastic properties for each group is constant, the geometric properties for various sections in that group may vary. For example, the deck is comprised of sections with six different values for the second moment of area.

Initial material properties for the FE model were generated as follows: (1) reinforced concrete was assumed to have a mass density of ρ = 6.2 lb-s^2/ft^4, Poisson's ratio of ν = 0.15, and the elastic modulus (E) listed in Table 3.7; (2) the soil was assumed to have a modulus of subgrade reaction of k_s = 480 kcf (medium dense sand). Note that the spring stiffnesses were obtained from the modulus of subgrade reaction by multiplying by the appropriate area (see Table 3.7).

Note that in order to define the characteristics of the system to accommodate the extreme climatic conditions, the systems identification procedures accounted for both changes in mass and stiffness during the period of interest. With the initial estimates of material properties and with the appropriate group stiffness reduced by a known amount, the stiffness sensitivity matrix, F, which relates changes in element stiffness to changes in resonant frequencies (See Appendix A for details), was developed. In similar manner, the mass sensitivity matrix, G, which relates changes in element mass to changes in resonant frequencies (See Appendix A for details), was developed. The elements of the stiffness sensitivity matrix F and the mass sensitivity matrix G are listed in Table 3.8 and Table 3.9, respectively. To develop the baseline model, the seven-step algorithm (See Appendix A for details) was utilized until the system converged. Note that the convergence of the system identification scheme is demonstrated in Table 3.10. Note also that the description of the selected modes as well as the target frequencies are listed in Table 3.10. From the table it can be seen that after ten iterations, the differences in the corresponding five frequencies of the identified baseline and the existing structures are 1.7%, 2.1%, 1.8%, 0.5%, and 1.6%. Please note that the baseline structure is assumed to be damage-free with

resonant frequencies near those of the existing structure.

Therefore, the model with frequencies of 3.046 Hz for the first bending mode in the Z-direction, 3.286 Hz for the first bending mode in the Y-direction, 4.506 Hz for the second bending mode in the Z-direction, 6.746 Hz for the first torsional mode, and 8.176 Hz for the second bending mode in the Y-direction is designated as the baseline structure. A dynamic finite element analysis was performed on the baseline structure to generate the corresponding mode shapes. The corresponding modal amplitudes for these modes at the simulated accelerometer locations are provided in Tables 3.11 to 3.15. The values of identified stiffness parameters for each group are provided in Table 3.16. Note that the stiffness values for Group 3 indicated in Table 3.16 refer to a single spring in Figure 3.9.

3.4 Location of Damage in the Existing Structure

Having identified modal parameters for the baseline structure, the problem of identifying the existing structure must now be solved. Recall that in order to identify the existing structure, any possible areas of damage are first located in the existing structure and then the severity of damage in those areas is estimated. Having accomplished the latter two tasks using the baseline structure as a reference, one would then have identified the existing structure. In this section, the problem of localizing the damage in the existing structure is addressed. Note that the logic behind this scheme is presented in Figure 3.1.

The damage detection model used in this study for the location of damage and the estimation of the severity of damage is shown in Figure 3.10. The damage detection model has 84 elements, i.e., Elements 1 to 72 for the deck, Elements 73 to 82 for the column, and Elements 83 and 84 for the Abutment #1 and Abutment #3, respectively. The sectional properties for each member are listed in Table 3.17. The polar moment of inertia J is calculated by sum of the second moment of area

about the Y-axis (I_{yy}) and the second moment of area about the Z-axis (I_{zz}). Note that Elements 36 and 37 represent the bentcap. For the two bending modes in the Z-direction and a torsional mode, the deck (i.e., Elements 1 to 72) and the column (i.e., Elements 73-82) are considered as Euler-Bernoulli beam elements and only springs in the Z-direction (i.e., k_z in Figure 3.10) are included in the damage detection model for Elements 83 and 84. For the two bending modes in the Y-direction, the deck (i.e., Elements 1 to 72) and the column (i.e., Elements 73-82) are also considered as Euler-Bernoulli beam elements and only springs in the Y-direction (i.e., k_y in Figure 3.10) are included in the damage detection model for Elements 83 and 84.

The location of potential damage in this structure is implemented using the following steps (See Appendix A for details):

1. Estimate a detailed modal amplitude representation for the deck by interpolating the thirteen sensor readings obtained in the field (i.e., W1-W13 and E1-E13) shown in Figure 3.2 using cubic-spline functions;
2. Estimate a detailed modal amplitude representation for the column by interpolating the four sensor readings obtained in the field (i.e., C1-C4) shown in Figure 3.2 using cubic-spline functions;
3. Generate the curvatures for the deck and the column using mode shapes from the baseline model and the field measurements;
4. Calculate the damage index DI_j for each element j;
5. Calculate the normalized damage indicator z_j; and
6. Determine if the structure is damaged or not damaged at Element j according to the pre-assigned decision rules with 84% of confidence level: (a) the element is damaged if $z_j \geq 1$; or (b) the element is not damaged if $z_j < 1$.

The results for the predicted damage locations are summarized in Figures 3.11 to 3.15 in which the individual mode is used to locate the possible damage area. Note that for the two bending modes in the Z-direction, the measurement

along the west girder (i.e, W1-W13) and the measurement along the east girder (i.e., E1-E13) are used separately.

3.5 Estimation of Damage Magnitude

The damage severity estimation is performed as follows. First, the baseline and post-damage sensitivities are obtained as described in the latter section. Second, the predicted damage locations are obtained from Figures 3.11 to 3.15. Finally, for each predicted damage location, the damage severity are estimated using the severity estimator (see Appendix A for detail). The estimated damage severities are listed in Table 3.18. Note that the magnitude of damage about the X-axis were estimated using the first torsional mode, the magnitude of damage about the Y-axis were estimated using the first two bending modes in the Z-direction, and the magnitude of damage about the Z-axis were estimated using the first two bending modes in the Y-direction. These magnitudes are fractional stiffness changes of those elements.

3.6 Estimation of Structural Properties of the Identified Existing Structure

Having determined the stiffness parameters for the baseline structure, the location of damage in the damage detection model, and the severity of damage in the damage detection model, the stiffness properties of the existing structure can now be estimated. In order to bridge the gap we make two assumptions: (1) the topology of FE model for the baseline structure and the existing structure are the same; and (2) the location and severity of damage in the existing structure relative to the baseline structure are given by the results predicted by the damage detection model. Thus the stiffness properties of the existing structure can be obtained from the equation:

$$k_j^{(\text{existing})} = k_j^{(\text{baseline})}[1 + \alpha_j] \tag{3.1}$$

where α_j is the damage severity of element j and k_j represents the bending stiffness

of element j. Note that if there is no damage at location j, the stiffness properties of the baseline and the existing structures are the same.

Using Equation (3.1) and the identified material properties of the baseline structure (see Table 3.16) and member properties (see Table 3.17), the estimated bending stiffness (EI) and torsional stiffness (GJ) for the deck and the column at Bent #2 of the existing structure are summarized in Table 3.19. The shear modulus, G, is estimated using the equation $G = E / 2(1+\nu)$.

Table 3.1 Measured Frequencies of the Bridge in December 1997

Mode	Frequency (Hz)
1 (First Bending in Z-dir.)	3.099
2 (First Bending in Y-dir.)	3.219
3 (Second Bending in Z-dir.)	4.426
4 (First Torsion)	6.781
5 (Second Bending in Y-dir.)	8.307

Table 3.2 Modal Coordinates of the First Bending Mode in the Z-direction at 3.099 Hz (Measured FIELD Data, December 1997)

Accelerometer Number	X-Modal Coordinate	Y-Modal Coordinate	Z-Modal Coordinate
W1	0.00000E+00	0.00000E+00	2.20158E-02
W2	0.00000E+00	0.00000E+00	4.53189E-01
W3	0.00000E+00	0.00000E+00	7.33487E-01
W4	0.00000E+00	0.00000E+00	8.29758E-01
W5	0.00000E+00	0.00000E+00	7.14347E-01
W6	0.00000E+00	0.00000E+00	3.98361E-01
W7	0.00000E+00	0.00000E+00	-3.02666E-02
W8	0.00000E+00	0.00000E+00	-4.72591E-01
W9	0.00000E+00	0.00000E+00	-8.51634E-01
W10	0.00000E+00	0.00000E+00	-1.00000E+00
W11	0.00000E+00	0.00000E+00	-8.57016E-01
W12	0.00000E+00	0.00000E+00	-4.83311E-01
W13	0.00000E+00	0.00000E+00	-2.49346E-02
E1	0.00000E+00	0.00000E+00	1.35526E-02
E2	0.00000E+00	0.00000E+00	4.86288E-01
E3	0.00000E+00	0.00000E+00	8.18737E-01
E4	0.00000E+00	0.00000E+00	8.65117E-01
E5	0.00000E+00	0.00000E+00	8.18605E-01
E6	0.00000E+00	0.00000E+00	5.07989E-01
E7	0.00000E+00	0.00000E+00	7.94779E-02
E8	0.00000E+00	0.00000E+00	-3.81846E-01
E9	0.00000E+00	0.00000E+00	-7.60657E-01
E10	0.00000E+00	0.00000E+00	-9.39525E-01
E11	0.00000E+00	0.00000E+00	-8.29605E-01
E12	0.00000E+00	0.00000E+00	-4.69797E-01
E13	0.00000E+00	0.00000E+00	-1.08152E-02
C1	-2.72633E-02	8.30641E-03	0.00000E+00
C2	-5.50934E-02	1.92359E-02	0.00000E+00
C3	-1.15509E-01	5.50934E-02	0.00000E+00
C4	-1.59216E-01	9.08009E-02	0.00000E+00

Table 3.3 Modal Coordinates of the First Bending Mode in the Y-direction at 3.219 Hz (Measured FIELD Data, December 1997)

Accelerometer Number	X-Modal Coordinate	Y-Modal Coordinate	Z-Modal Coordinate
W1	0.00000E+00	5.74840E-02	0.00000E+00
W2	0.00000E+00	2.57819E-01	0.00000E+00
W3	0.00000E+00	4.27746E-01	0.00000E+00
W4	0.00000E+00	6.55880E-01	0.00000E+00
W5	0.00000E+00	8.28601E-01	0.00000E+00
W6	0.00000E+00	9.13179E-01	0.00000E+00
W7	0.00000E+00	9.98793E-01	0.00000E+00
W8	0.00000E+00	9.98330E-01	0.00000E+00
W9	0.00000E+00	1.00000E+00	0.00000E+00
W10	0.00000E+00	8.13011E-01	0.00000E+00
W11	0.00000E+00	6.55458E-01	0.00000E+00
W12	0.00000E+00	3.28355E-01	0.00000E+00
W13	0.00000E+00	5.79314E-02	0.00000E+00
E1	0.00000E+00	5.74840E-02	0.00000E+00
E2	0.00000E+00	2.57819E-01	0.00000E+00
E3	0.00000E+00	4.27746E-01	0.00000E+00
E4	0.00000E+00	6.55880E-01	0.00000E+00
E5	0.00000E+00	8.28601E-01	0.00000E+00
E6	0.00000E+00	9.13179E-01	0.00000E+00
E7	0.00000E+00	9.98793E-01	0.00000E+00
E8	0.00000E+00	9.98330E-01	0.00000E+00
E9	0.00000E+00	1.00000E+00	0.00000E+00
E10	0.00000E+00	8.13011E-01	0.00000E+00
E11	0.00000E+00	6.55458E-01	0.00000E+00
E12	0.00000E+00	3.28355E-01	0.00000E+00
E13	0.00000E+00	5.79314E-02	0.00000E+00
C1	0.00000E+00	4.37078E-02	0.00000E+00
C2	0.00000E+00	1.14180E-01	0.00000E+00
C3	0.00000E+00	3.00463E-01	0.00000E+00
C4	0.00000E+00	4.85945E-01	0.00000E+00

Table 3.4 Modal Coordinates of the Second Bending Mode in the Z-direction at 4.426 Hz (Measured FIELD Data, December 1997)

Accelerometer Number	X-Modal Coordinate	Y-Modal Coordinate	Z-Modal Coordinate
W1	0.00000E+00	0.00000E+00	4.06736E-02
W2	0.00000E+00	0.00000E+00	5.63406E-01
W3	0.00000E+00	0.00000E+00	8.36842E-01
W4	0.00000E+00	0.00000E+00	8.19988E-01
W5	0.00000E+00	0.00000E+00	5.99607E-01
W6	0.00000E+00	0.00000E+00	3.14300E-01
W7	0.00000E+00	0.00000E+00	1.19924E-01
W8	0.00000E+00	0.00000E+00	3.07051E-01
W9	0.00000E+00	0.00000E+00	6.85741E-01
W10	0.00000E+00	0.00000E+00	1.00000E+00
W11	0.00000E+00	0.00000E+00	9.71314E-01
W12	0.00000E+00	0.00000E+00	5.84974E-01
W13	0.00000E+00	0.00000E+00	2.86070E-02
E1	0.00000E+00	0.00000E+00	3.85501E-02
E2	0.00000E+00	0.00000E+00	5.66013E-01
E3	0.00000E+00	0.00000E+00	8.46376E-01
E4	0.00000E+00	0.00000E+00	8.07954E-01
E5	0.00000E+00	0.00000E+00	6.21114E-01
E6	0.00000E+00	0.00000E+00	3.14200E-01
E7	0.00000E+00	0.00000E+00	1.07861E-01
E8	0.00000E+00	0.00000E+00	3.07070E-01
E9	0.00000E+00	0.00000E+00	6.90489E-01
E10	0.00000E+00	0.00000E+00	9.76001E-01
E11	0.00000E+00	0.00000E+00	9.13549E-01
E12	0.00000E+00	0.00000E+00	5.44273E-01
E13	0.00000E+00	0.00000E+00	2.40721E-02
C1	-4.97630E-03	-2.22547E-03	0.00000E+00
C2	-1.20512E-02	-2.41386E-03	0.00000E+00
C3	-2.86274E-02	-4.72093E-03	0.00000E+00
C4	-5.02072E-02	-7.03756E-03	0.00000E+00

Table 3.5 Modal Coordinates of the First Torsional Mode at 6.781 Hz (Measured FIELD Data, December 1997)

Accelerometer Number	X-Modal Coordinate	Y-Modal Coordinate	Z-Modal Coordinate
W1	0.00000E+00	0.00000E+00	-5.56943E-02
W2	0.00000E+00	0.00000E+00	-3.97133E-01
W3	0.00000E+00	0.00000E+00	-7.02481E-01
W4	0.00000E+00	0.00000E+00	-9.01755E-01
W5	0.00000E+00	0.00000E+00	-1.00000E+00
W6	0.00000E+00	0.00000E+00	-9.52193E-01
W7	0.00000E+00	0.00000E+00	-8.87267E-01
W8	0.00000E+00	0.00000E+00	-9.03091E-01
W9	0.00000E+00	0.00000E+00	-9.36355E-01
W10	0.00000E+00	0.00000E+00	-8.10162E-01
W11	0.00000E+00	0.00000E+00	-6.54837E-01
W12	0.00000E+00	0.00000E+00	-4.18341E-01
W13	0.00000E+00	0.00000E+00	-5.43730E-02
E1	0.00000E+00	0.00000E+00	6.23731E-02
E2	0.00000E+00	0.00000E+00	4.59434E-01
E3	0.00000E+00	0.00000E+00	6.33575E-01
E4	0.00000E+00	0.00000E+00	7.46388E-01
E5	0.00000E+00	0.00000E+00	9.50836E-01
E6	0.00000E+00	0.00000E+00	9.60312E-01
E7	0.00000E+00	0.00000E+00	8.56658E-01
E8	0.00000E+00	0.00000E+00	8.99060E-01
E9	0.00000E+00	0.00000E+00	8.88534E-01
E10	0.00000E+00	0.00000E+00	7.49130E-01
E11	0.00000E+00	0.00000E+00	5.97595E-01
E12	0.00000E+00	0.00000E+00	3.75937E-01
E13	0.00000E+00	0.00000E+00	4.77585E-02
C1	5.35159E-03	-9.43218E-02	0.00000E+00
C2	1.33434E-02	-1.83278E-01	0.00000E+00
C3	2.91820E-02	-4.06459E-01	0.00000E+00
C4	1.72785E-02	-5.63025E-01	0.00000E+00

Table 3.6 Modal Coordinates of the Second Bending Mode in the Y-direction at 8.307 Hz (Measured FIELD Data, December 1997)

Accelerometer Number	X-Modal Coordinate	Y-Modal Coordinate	Z-Modal Coordinate
W1	0.00000E+00	2.65044E-01	0.00000E+00
W2	0.00000E+00	5.73185E-01	0.00000E+00
W3	0.00000E+00	8.68381E-01	0.00000E+00
W4	0.00000E+00	9.84906E-01	0.00000E+00
W5	0.00000E+00	8.03697E-01	0.00000E+00
W6	0.00000E+00	4.39766E-01	0.00000E+00
W7	0.00000E+00	-2.80840E-02	0.00000E+00
W8	0.00000E+00	-4.89270E-01	0.00000E+00
W9	0.00000E+00	-8.57547E-01	0.00000E+00
W10	0.00000E+00	-1.00000E+00	0.00000E+00
W11	0.00000E+00	-8.92005E-01	0.00000E+00
W12	0.00000E+00	-5.99141E-01	0.00000E+00
W13	0.00000E+00	-2.26103E-01	0.00000E+00
E1	0.00000E+00	2.65044E-01	0.00000E+00
E2	0.00000E+00	5.73185E-01	0.00000E+00
E3	0.00000E+00	8.68381E-01	0.00000E+00
E4	0.00000E+00	9.84906E-01	0.00000E+00
E5	0.00000E+00	8.03697E-01	0.00000E+00
E6	0.00000E+00	4.39766E-01	0.00000E+00
E7	0.00000E+00	-2.80840E-02	0.00000E+00
E8	0.00000E+00	-4.89270E-01	0.00000E+00
E9	0.00000E+00	-8.57547E-01	0.00000E+00
E10	0.00000E+00	-1.00000E+00	0.00000E+00
E11	0.00000E+00	-8.92005E-01	0.00000E+00
E12	0.00000E+00	-5.99141E-01	0.00000E+00
E13	0.00000E+00	-2.26103E-01	0.00000E+00
C1	0.00000E+00	-8.51925E-03	0.00000E+00
C2	0.00000E+00	-1.52304E-02	0.00000E+00
C3	0.00000E+00	-3.24593E-02	0.00000E+00
C4	0.00000E+00	-4.30193E-02	0.00000E+00

Table 3.7 Initial Values of Material Properties of FE Model

	Group 1 (Deck)	Group 2 (Column and Footing)	Group 3 (Abutment-Soil System)
E (lb/ft^2)	576.00×10^6 (4000 ksi)	576.00×10^6 (4000 ksi)	-
k (lb/ft)	-	-	23.28×10^6
ρ ($lb \cdot s^2/ft^4$)	6.204	6.204	-

Table 3.8 Stiffness Sensitivity Matrix F for the System (December 1997)

Mode	Group Identification		
	Group 1 (Deck)	Group 2 (Column and Footing)	Group 3 (Abutment-Soil System)
1 (First Bending in Z-dir.)	0.8588	0.0814	0.0598
2 (First Bending in Y-dir.)	0.6323	0.0935	0.2741
3 (Second Bending in Z-dir.)	0.7928	0.0400	0.1672
4 (First Torsion)	0.4742	0.2379	0.2880
5 (Second Bending in Y-dir.)	0.6087	0.0022	0.3891

Table 3.9 Mass Sensitivity Matrix G for the System (December 1997)

Mode	Group 1 and Group 2
1 (First Bending in Z-dir.)	0.9093
2 (First Bending in Y-dir.)	0.9092
3 (Second Bending in Z-dir.)	0.9090
4 (First Torsion)	0.9090
5 (Second Bending in Y-dir.)	0.9093

Table 3.10 System Identification (December 1997)

Mode	Frequency of Initial FE model	Updated Frequencies (Hz)			Frequency of Target Structure	Error (%)	
		Iter. 2	Iter. 6	Iter. 10		Initial	Final
1	2.950	3.001	3.043	3.046	3.099	4.8	1.7
2	3.019	3.095	3.280	3.286	3.219	6.2	2.1
3	4.249	4.426	4.500	4.506	4.426	4.0	1.8
4	6.228	6.518	6.733	6.746	6.781	8.2	0.5
5	7.163	7.912	8.152	8.176	8.307	13.8	1.6

Table 3.11 Modal Coordinates of the First Bending Mode in the Z-direction at 3.046 Hz (Identified Baseline Data, December 1997)

Accelerometer Number	X-Modal Coordinate	Y-Modal Coordinate	Z-Modal Coordinate
W1	-1.8090E-01	2.6963E-04	2.1931E-02
W2	-1.7440E-01	-7.9432E-05	5.2500E-01
W3	-1.5160E-01	-2.1094E-04	8.5400E-01
W4	-1.1350E-01	-2.1254E-04	9.9430E-01
W5	-7.7455E-02	-2.4573E-04	8.4000E-01
W6	-5.4175E-02	-3.2235E-04	4.6150E-01
W7	-5.1339E-02	-6.9543E-04	7.3156E-03
W8	-5.8829E-02	1.5572E-04	-4.0270E-01
W9	-8.0150E-02	1.9606E-04	-7.1890E-01
W10	-1.1020E-01	1.7915E-04	-8.4020E-01
W11	-1.4120E-01	1.7540E-04	-7.1940E-01
W12	-1.5970E-01	5.7528E-05	-4.4460E-01
W13	-1.6580E-01	-2.9514E-04	-1.8542E-02
E1	-1.8090E-01	-2.6963E-04	2.1931E-02
E2	-1.7440E-01	7.9432E-05	5.2500E-01
E3	-1.5160E-01	2.1094E-04	8.5400E-01
E4	-1.1350E-01	2.1254E-04	9.9430E-01
E5	-7.7455E-02	2.4573E-04	8.4000E-01
E6	-5.4175E-02	3.2235E-04	4.6150E-01
E7	-5.1339E-02	6.9543E-04	7.3156E-03
E8	-5.8829E-02	-1.5572E-04	-4.0270E-01
E9	-8.0150E-02	-1.9606E-04	-7.1890E-01
E10	-1.1020E-01	-1.7915E-04	-8.4020E-01
E11	-1.4120E-01	-1.7540E-04	-7.1940E-01
E12	-1.5970E-01	-5.7528E-05	-4.4460E-01
E13	-1.6580E-01	2.9514E-04	-1.8542E-02
C1	-4.5312E-02	0.0000E+00	3.3750E-03
C2	-7.0763E-02	0.0000E+00	3.6187E-03
C3	-1.4370E-01	0.0000E+00	4.1398E-03
C4	-2.0410E-01	0.0000E+00	4.6775E-03

Table 3.12 Modal Coordinates of the First Bending Mode in the Y-direction at 3.286 Hz (Identified Baseline Data, December 1997)

Accelerometer Number	X-Modal Coordinate	Y-Modal Coordinate	Z-Modal Coordinate
W1	-1.2860E-01	1.1630E-01	-8.5269E-02
W2	-1.1820E-01	3.2880E-01	-1.0980E-01
W3	-1.1520E-01	5.2520E-01	-1.5660E-01
W4	-9.5342E-02	7.3280E-01	-2.0590E-01
W5	-6.3381E-02	8.8410E-01	-2.4890E-01
W6	-2.6493E-02	9.7280E-01	-2.8460E-01
W7	5.3144E-03	9.9470E-01	-3.0660E-01
W8	3.5286E-02	9.5740E-01	-2.8380E-01
W9	6.9172E-02	8.5980E-01	-2.4760E-01
W10	9.7881E-02	7.0760E-01	-2.0480E-01
W11	1.1510E-01	5.0590E-01	-1.5590E-01
W12	1.1700E-01	3.1820E-01	-1.0970E-01
W13	1.2750E-01	1.1640E-01	-8.5994E-02
E1	1.2860E-01	1.1630E-01	8.5269E-02
E2	1.1820E-01	3.2880E-01	1.0980E-01
E3	1.1520E-01	5.2520E-01	1.5660E-01
E4	9.5342E-02	7.3280E-01	2.0590E-01
E5	6.3381E-02	8.8410E-01	2.4890E-01
E6	2.6493E-02	9.7280E-01	2.8460E-01
E7	-5.3144E-03	9.9470E-01	3.0660E-01
E8	-3.5286E-02	9.5740E-01	2.8380E-01
E9	-6.9172E-02	8.5980E-01	2.4760E-01
E10	-9.7881E-02	7.0760E-01	2.0480E-01
E11	-1.1510E-01	5.0590E-01	1.5590E-01
E12	-1.1700E-01	3.1820E-01	1.0970E-01
E13	-1.2750E-01	1.1640E-01	8.5994E-02
C1	0.0000E+00	4.6505E-02	4.4746E-14
C2	0.0000E+00	7.1234E-02	4.4876E-14
C3	-2.4875E-14	2.2500E-01	4.4732E-14
C4	0.0000E+00	4.3850E-01	4.4062E-14

Table 3.13 Modal Coordinates of the Second Bending Mode in the Z-direction at 4.506 Hz(Identified Baseline Data, December 1997)

Accelerometer Number	X-Modal Coordinate	Y-Modal Coordinate	Z-Modal Coordinate
W1	-9.3250E-02	1.4644E-04	3.4750E-02
W2	-9.0101E-02	-1.9908E-04	4.3400E-01
W3	-6.0184E-02	-3.9965E-04	7.2370E-01
W4	-1.0337E-02	-3.8626E-04	8.1600E-01
W5	3.0324E-02	-5.2481E-04	6.2310E-01
W6	4.1965E-02	-1.4467E-03	3.0400E-01
W7	7.6028E-03	-1.1774E-02	1.4530E-01
W8	-2.4167E-02	-1.6563E-03	3.9670E-01
W9	-7.4843E-03	-6.3918E-04	7.7300E-01
W10	3.9276E-02	-4.6876E-04	9.8220E-01
W11	9.5114E-02	-4.7234E-04	8.6460E-01
W12	1.2870E-01	-2.1504E-04	5.2410E-01
W13	1.3340E-01	2.8398E-04	4.0964E-02
E1	-9.3250E-02	-1.4644E-04	3.4750E-02
E2	-9.0101E-02	1.9908E-04	4.3400E-01
E3	-6.0184E-02	3.9965E-04	7.2370E-01
E4	-1.0337E-02	3.8626E-04	8.1600E-01
E5	3.0324E-02	5.2481E-04	6.2310E-01
E6	4.1965E-02	1.4467E-03	3.0400E-01
E7	7.6028E-03	1.1774E-02	1.4530E-01
E8	-2.4167E-02	1.6563E-03	3.9670E-01
E9	-7.4843E-03	6.3918E-04	7.7300E-01
E10	3.9276E-02	4.6876E-04	9.8220E-01
E11	9.5114E-02	4.7234E-04	8.6460E-01
E12	1.2870E-01	2.1504E-04	5.2410E-01
E13	1.3340E-01	-2.8398E-04	4.0964E-02
C1	5.9713E-03	8.8048E-14	6.8590E-02
C2	9.2954E-03	1.9971E-12	7.3469E-02
C3	1.8678E-02	2.1408E-12	8.3894E-02
C4	2.6356E-02	-6.8725E-13	9.4640E-02

Table 3.14 Modal Coordinates of the First Torsional Mode at 6.746 Hz (Identified Baseline Data, December 1997)

Accelerometer Number	X-Modal Coordinate	Y-Modal Coordinate	Z-Modal Coordinate
W1	-6.3283E-02	-1.3560E-01	1.7210E-01
W2	-5.8349E-02	-9.4310E-02	3.7310E-01
W3	-5.0380E-02	-6.6859E-02	5.1970E-01
W4	-3.6482E-02	-3.9886E-02	6.5210E-01
W5	-1.9399E-02	-2.3675E-02	7.3300E-01
W6	-2.9251E-03	-1.8793E-02	7.5910E-01
W7	4.3116E-03	-2.5067E-02	7.3970E-01
W8	1.0548E-02	-2.8440E-02	7.4830E-01
W9	2.4296E-02	-4.0511E-02	7.1560E-01
W10	3.7958E-02	-5.9230E-02	6.3310E-01
W11	4.8738E-02	-8.3572E-02	5.0400E-01
W12	5.5043E-02	-1.0570E-01	3.6350E-01
W13	5.9025E-02	-1.3960E-01	1.7290E-01
E1	6.3283E-02	-1.3560E-01	-1.7210E-01
E2	5.8349E-02	-9.4310E-02	-3.7310E-01
E3	5.0380E-02	-6.6859E-02	-5.1970E-01
E4	3.6482E-02	-3.9886E-02	-6.5210E-01
E5	1.9399E-02	-2.3675E-02	-7.3300E-01
E6	2.9251E-03	-1.8793E-02	-7.5910E-01
E7	-4.3116E-03	-2.5067E-02	-7.3970E-01
E8	-1.0548E-02	-2.8440E-02	-7.4830E-01
E9	-2.4296E-02	-4.0511E-02	-7.1560E-01
E10	-3.7958E-02	-5.9230E-02	-6.3310E-01
E11	-4.8738E-02	-8.3572E-02	-5.0400E-01
E12	-5.5043E-02	-1.0570E-01	-3.6350E-01
E13	-5.9025E-02	-1.3960E-01	-1.7290E-01
C1	1.1281E-09	7.1544E-02	1.1704E-09
C2	-1.2180E-10	1.0380E-01	1.1823E-09
C3	-1.9236E-09	2.5470E-01	1.1982E-09
C4	-2.2498E-09	4.0300E-01	1.2055E-09

Table 3.15 Modal Coordinates of the Second Bending Mode in the Y-direction at 8.176 Hz (Identified Baseline Data, December 1997)

Accelerometer Number	X-Modal Coordinate	Y-Modal Coordinate	Z-Modal Coordinate
W1	-1.8640E-01	4.0960E-01	-2.2920E-01
W2	-1.4320E-01	7.3460E-01	-2.3600E-01
W3	-7.6667E-02	9.4210E-01	-2.4230E-01
W4	4.0532E-02	9.8760E-01	-2.1490E-01
W5	1.5530E-01	7.9370E-01	-1.5900E-01
W6	2.3130E-01	4.0940E-01	-8.1354E-02
W7	2.5320E-01	-5.4000E-02	-1.3852E-03
W8	2.1980E-01	-4.8740E-01	7.2185E-02
W9	1.3870E-01	-8.2710E-01	1.4250E-01
W10	2.6113E-02	-9.8290E-01	1.9400E-01
W11	-8.4399E-02	-9.1840E-01	2.2130E-01
W12	-1.4570E-01	-7.1280E-01	2.1890E-01
W13	-1.8700E-01	-4.0170E-01	2.2070E-01
E1	1.8640E-01	4.0960E-01	2.2920E-01
E2	1.4320E-01	7.3460E-01	2.3600E-01
E3	7.6667E-02	9.4210E-01	2.4230E-01
E4	-4.0532E-02	9.8760E-01	2.1490E-01
E5	-1.5530E-01	7.9370E-01	1.5900E-01
E6	-2.3130E-01	4.0940E-01	8.1354E-02
E7	-2.5320E-01	-5.4000E-02	1.3852E-03
E8	-2.1980E-01	-4.8740E-01	-7.2185E-02
E9	-1.3870E-01	-8.2710E-01	-1.4250E-01
E10	-2.6113E-02	-9.8290E-01	-1.9400E-01
E11	8.4399E-02	-9.1840E-01	-2.2130E-01
E12	1.4570E-01	-7.1280E-01	-2.1890E-01
E13	1.8700E-01	-4.0170E-01	-2.2070E-01
C1	9.7387E-09	-4.9498E-03	3.0351E-08
C2	-3.4499E-09	-7.3014E-03	3.0704E-08
C3	-2.1207E-08	-1.9713E-02	3.1220E-08
C4	-2.3938E-08	-3.4893E-02	3.1528E-08

Table 3.16 Identified Material Properties of the Baseline Structure (December 1997)

	Group 1 (Deck)	Group 2 (Column and Footing)	Group 3 (Abutment-Soil System)
E (lb/ft^2)	453.07×10^6 (3146 ksi)	364.02×10^6 (2528 ksi)	-
k (lb/ft)	-	-	36.98×10^6
ρ ($lb \cdot s^2/ft^4$)	4.6525	4.6525	-

Table 3.17 Member Properties

	Element No.	I_{yy} (ft^4)	I_{zz} (ft^4)	J (ft^4)
Concrete Box Girder	4-23, 50-69	347	2877	3224
	1-3, 24-26, 47-49, 70-72	354	3084	3438
	27-29, 44-46	362	3293	3655
	30-32, 41-43	370	3500	3870
	33-35, 38-40	374	3605	3979
	36, 37	750	10551	11301
Column	73-82	31	-	62

Table 3.18 Predicted Damage Magnitudes (December 1997)

Element No.	Damage Severity, α_j		
	about X-axis	about Y-axis	about Z-axis
1	-0.08	-	-
2	-0.08	-	-
3	-0.08	-	-
4	-0.08	-	-
5	-0.08	-	-
6	-0.08	-0.33	-
7	-	-0.33	-
8	-	-0.32	-
9	-	-0.31	-
10	-	-0.27	-
11	-	-0.29	-
12	-	-0.30	-
13	-	-0.33	-
18	-	-	-0.17
19	-	-	-0.16
24	-	-0.18	-
25	-	-0.22	-
26	-	-0.20	-
36	-	-	-0.20
37	-	-	-0.19
47	-	-	-0.35
48	-	-0.13	-0.42
49	-	-0.13	-0.43
50	-	-0.12	-0.35
51	-	-0.10	-
52	-	-0.09	-
53	-	-0.07	-
55	-	-0.07	-
56	-	-0.11	-
57	-	-0.12	-
58	-	-0.16	-
59	-	-0.21	-0.47
60	-	-0.27	-0.45
61	-	-0.28	-0.44
62	-	-0.24	-0.45
63	-	-0.21	-
68	-0.07	-	-
69	-0.07	-	-
70	-0.08	-	-
71	-0.08	-	-
72	-0.08	-	-

Table 3.19 Bending (EI) and Torsional (GJ) Stiffnesses of the Existing Structure (December 1997)

	Element No.	EI_{yy} (lb·ft²)	EI_{zz} (lb·ft²)	GJ (lb·ft²)
Concrete Box Girder	1	1.6039E+11	1.3973E+12	6.7724E+11
	2	1.6039E+11	1.3973E+12	6.7724E+11
	3	1.6039E+11	1.3973E+12	6.7724E+11
	4	1.5722E+11	1.3035E+12	6.3509E+11
	5	1.5722E+11	1.3035E+12	6.3509E+11
	6	1.0533E+11	1.3035E+12	6.1253E+11
	7	1.0533E+11	1.3035E+12	6.1253E+11
	8	1.0691E+11	1.3035E+12	6.1321E+11
	9	1.0848E+11	1.3035E+12	6.1390E+11
	10	1.1477E+11	1.3035E+12	6.1663E+11
	11	1.1162E+11	1.3035E+12	6.1526E+11
	12	1.1005E+11	1.3035E+12	6.1458E+11
	13	1.0533E+11	1.3035E+12	6.1253E+11
	14	1.5722E+11	1.3035E+12	6.3509E+11
	15	1.5722E+11	1.3035E+12	6.3509E+11
	16	1.5722E+11	1.3035E+12	6.3509E+11
	17	1.5722E+11	1.3035E+12	6.3509E+11
	18	1.5722E+11	1.0819E+12	5.3874E+11
	19	1.5722E+11	1.0949E+12	5.4441E+11
	20	1.5722E+11	1.3035E+12	6.3509E+11
	21	1.5722E+11	1.3035E+12	6.3509E+11
	22	1.5722E+11	1.3035E+12	6.3509E+11
	23	1.5722E+11	1.3035E+12	6.3509E+11
	24	1.3152E+11	1.3973E+12	6.6469E+11
	25	1.2510E+11	1.3973E+12	6.6190E+11
	26	1.2831E+11	1.3973E+12	6.6329E+11
	27	1.6401E+11	1.4920E+12	7.1999E+11
	28	1.6401E+11	1.4920E+12	7.1999E+11
	29	1.6401E+11	1.4920E+12	7.1999E+11
	30	1.6764E+11	1.5857E+12	7.6234E+11
	31	1.6764E+11	1.5857E+12	7.6234E+11
	32	1.6764E+11	1.5857E+12	7.6234E+11
	33	1.6945E+11	1.6333E+12	7.8381E+11
	34	1.6945E+11	1.6333E+12	7.8381E+11
	35	1.6945E+11	1.6333E+12	7.8381E+11
	36	3.3980E+11	3.8243E+12	1.8105E+12
	37	3.3980E+11	3.8721E+12	1.8313E+12
	38	1.6945E+11	1.6333E+12	7.8381E+11
	39	1.6945E+11	1.6333E+12	7.8381E+11
	40	1.6945E+11	1.6333E+12	7.8381E+11
	41	1.6764E+11	1.5857E+12	7.6234E+11

Table 3.19 Continued

	Element No.	EI_{yy} (lb·ft²)	EI_{zz} (lb·ft²)	GJ (lb·ft²)
	42	1.6764E+11	1.5857E+12	7.6234E+11
	43	1.6764E+11	1.5857E+12	7.6234E+11
	44	1.6401E+11	1.4920E+12	7.1999E+11
	45	1.6401E+11	1.4920E+12	7.1999E+11
	46	1.6401E+11	1.4920E+12	7.1999E+11
	47	1.6039E+11	9.0822E+11	4.6461E+11
	48	1.3954E+11	8.1042E+11	4.1302E+11
	49	1.3954E+11	7.9644E+11	4.0695E+11
	50	1.3835E+11	8.4726E+11	4.2853E+11
	51	1.4149E+11	1.3035E+12	6.2825E+11
	52	1.4307E+11	1.3035E+12	6.2893E+11
	53	1.4621E+11	1.3035E+12	6.3030E+11
	54	1.5722E+11	1.3035E+12	6.3509E+11
	55	1.4621E+11	1.3035E+12	6.3030E+11
	56	1.3992E+11	1.3035E+12	6.2757E+11
	57	1.3835E+11	1.3035E+12	6.2688E+11
	58	1.3206E+11	1.3035E+12	6.2415E+11
	59	1.2420E+11	6.9085E+11	3.5437E+11
	60	1.1477E+11	7.1692E+11	3.6160E+11
	61	1.1320E+11	7.2995E+11	3.6658E+11
	62	1.1948E+11	7.1692E+11	3.6365E+11
	63	1.2420E+11	1.3035E+12	6.2073E+11
	64	1.5722E+11	1.3035E+12	6.3509E+11
	65	1.5722E+11	1.3035E+12	6.3509E+11
	66	1.5722E+11	1.3035E+12	6.3509E+11
	67	1.5722E+11	1.3035E+12	6.3509E+11
	68	1.5722E+11	1.3035E+12	6.3509E+11
	69	1.5722E+11	1.3035E+12	6.3509E+11
	70	1.6039E+11	1.3973E+12	6.7724E+11
	71	1.6039E+11	1.3973E+12	6.7724E+11
	72	1.6039E+11	1.3973E+12	6.7724E+11
Column	73-82	1.1285E+10	-	9.8127E+09

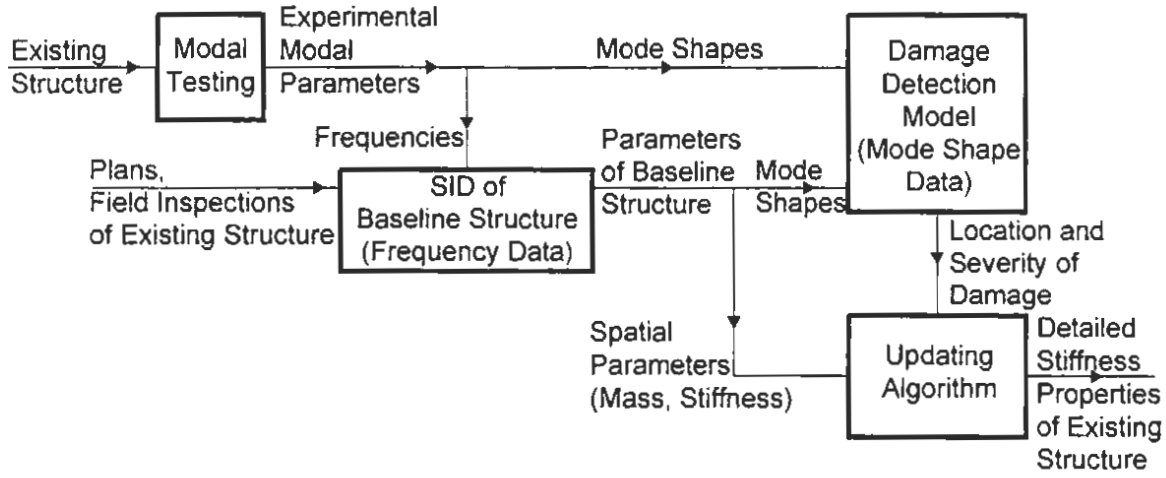

Figure 3.1 Schematic of Approach Used to Identify Stiffness Properties of Baseline and Existing Structures

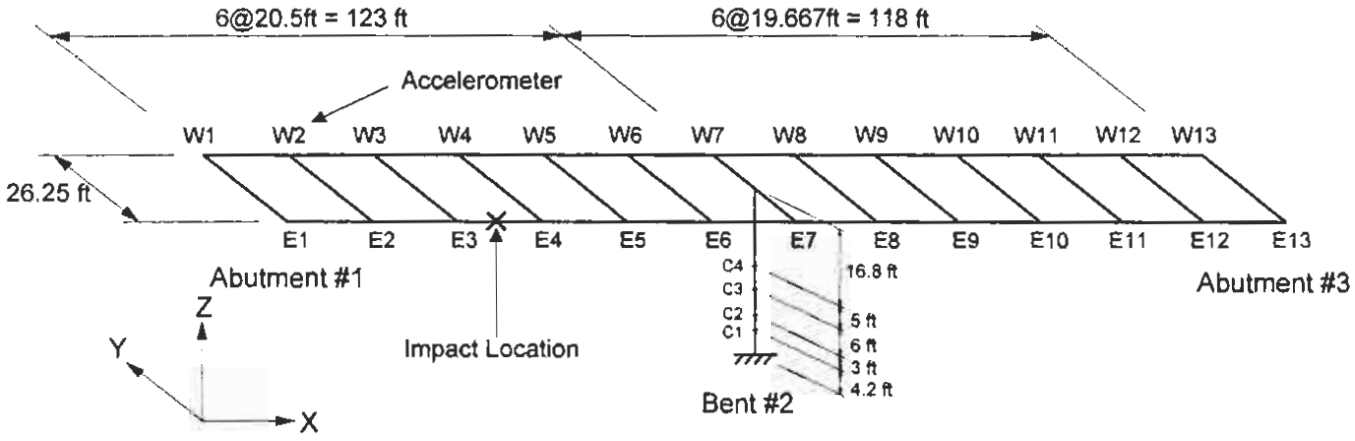

Figure 3.2 Locations of Accelerometers on the Bridge

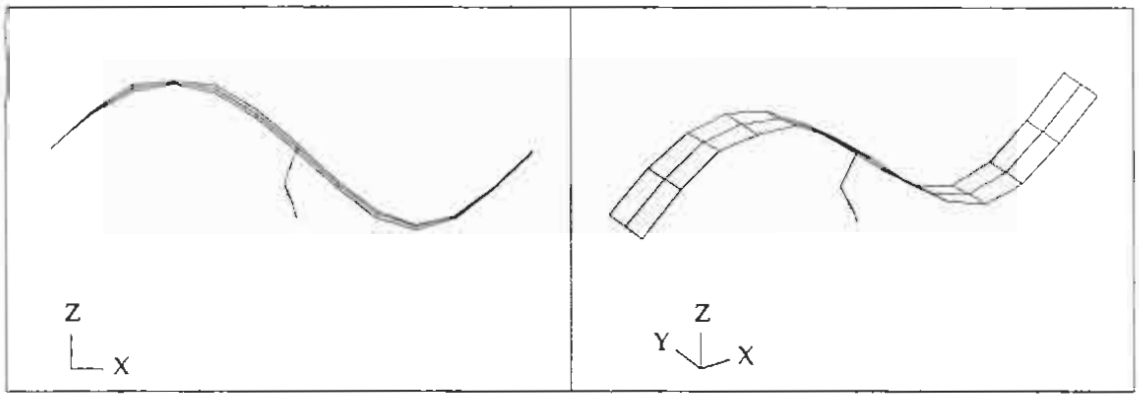

Figure 3.3 First Bending Mode Identified in the Z-direction at 3.099Hz (December 1997)

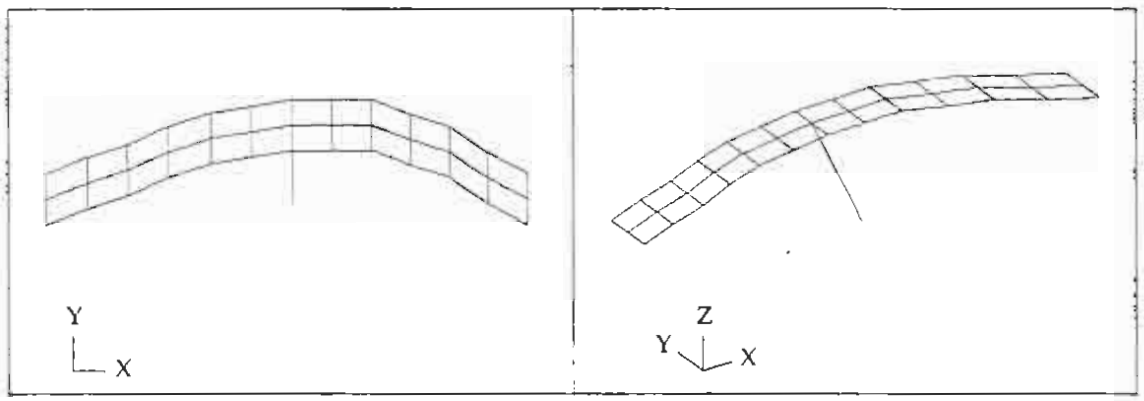

Figure 3.4 First Bending Mode Identified in the Y-direction at 3.219Hz (December 1997)

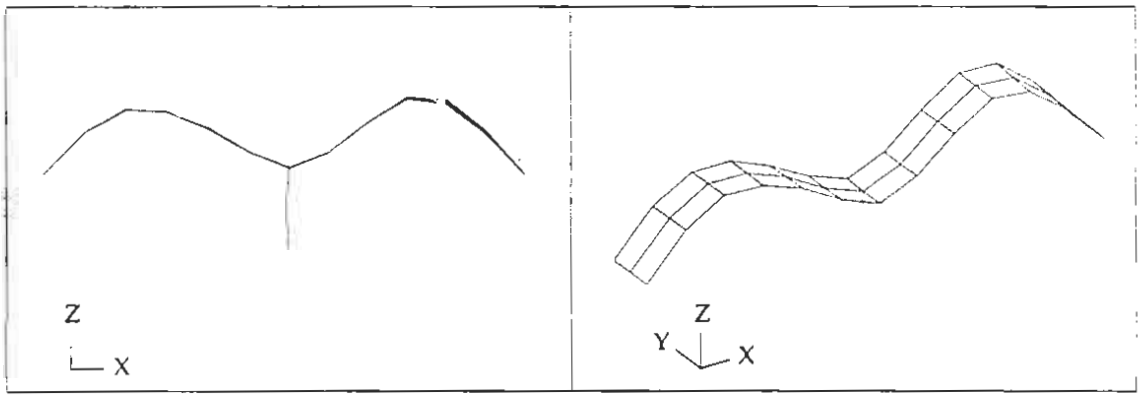

Figure 3.5 Second Bending Mode Identified in the Z-direction at 4.426Hz (December 1997)

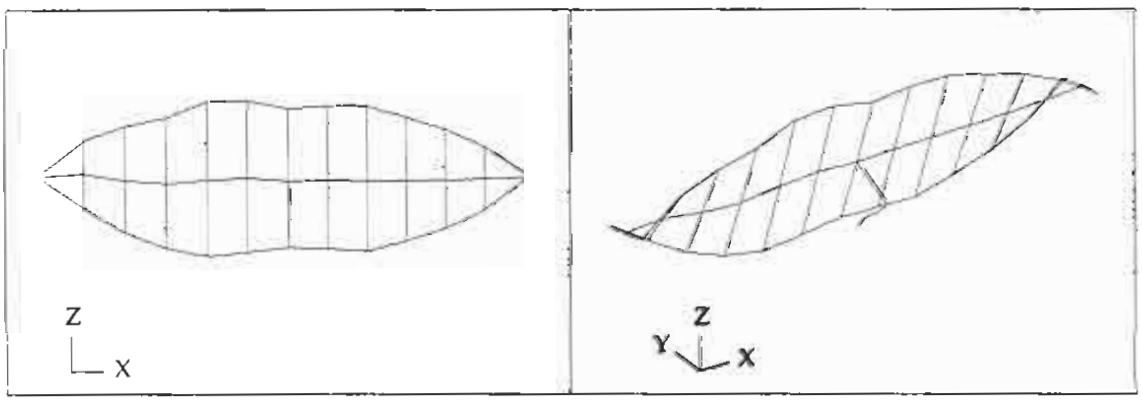

Figure 3.6 First Torsional Mode Identified at 6.781Hz (December 1997)

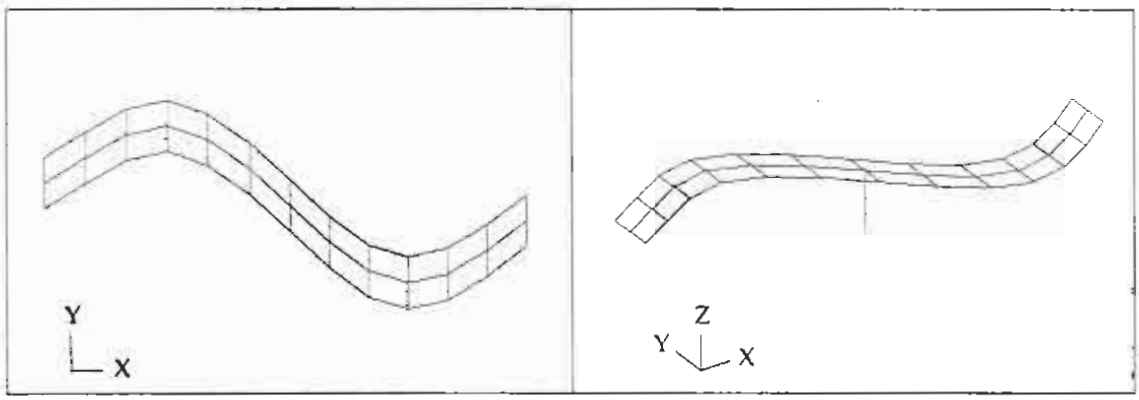

Figure 3.7 Second Bending Mode Identified in the Y-direction at 8.307Hz (December 1997)

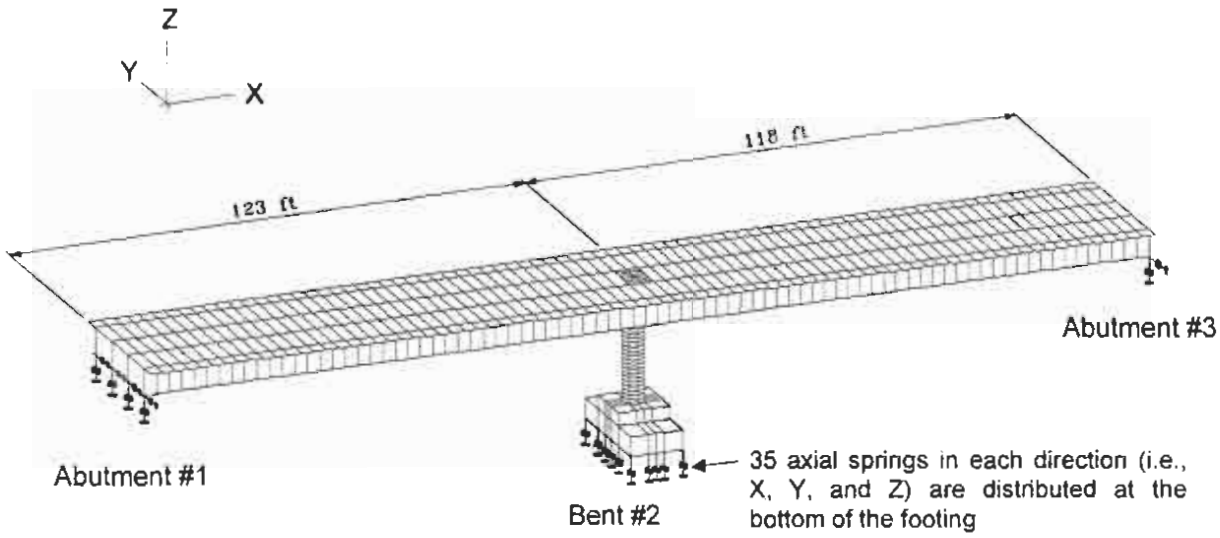

Figure 3.8 Schematic of Finite Element Model

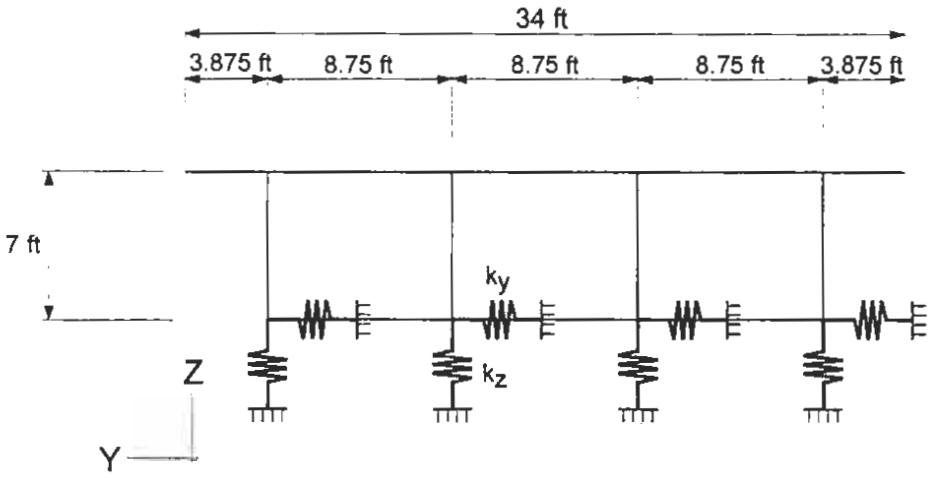

Figure 3.9 Locations of Springs at Abutments #1 and #3

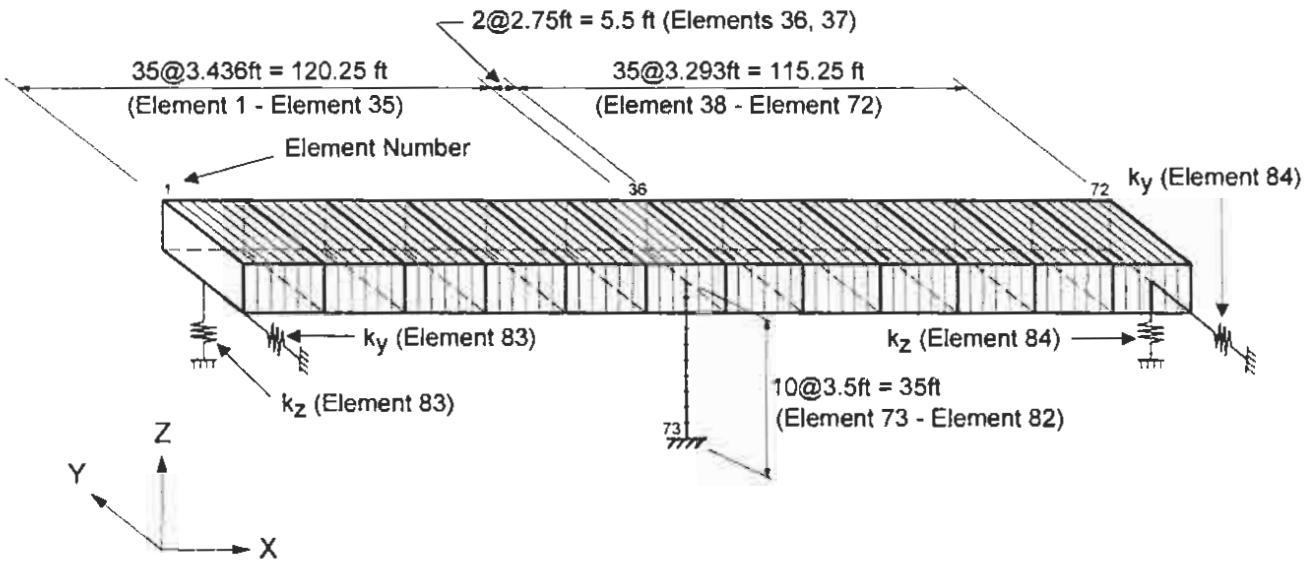

Figure 3.10 Damage Detection Model

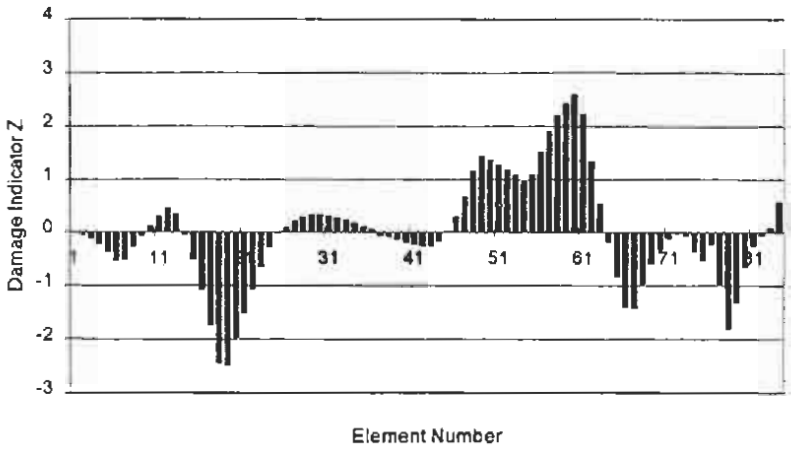

(a)

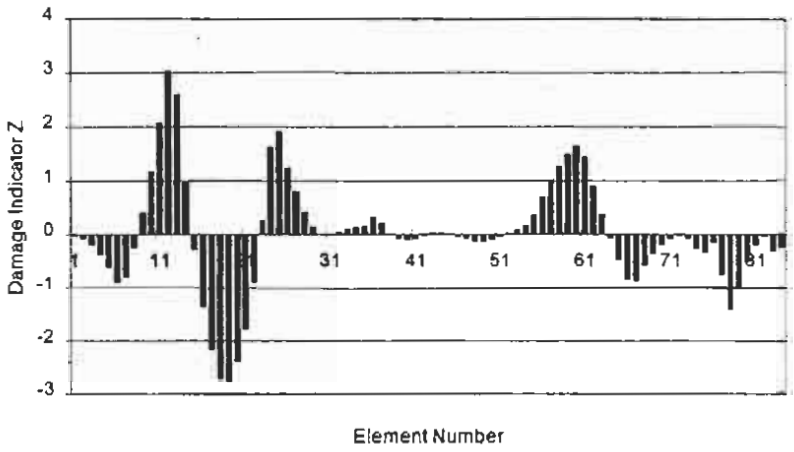

(b)

Figure 3.11 Damage Localization Results Using the First Bending Mode in the Z-dir. (December 1997): (a) Result using the measurements along the west girder (W1-W13);(b) Result using the measurements along the east girder (E1-E13).

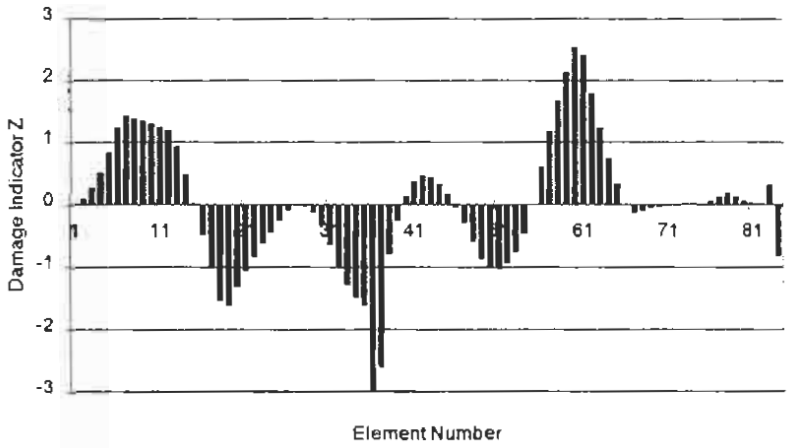

(a)

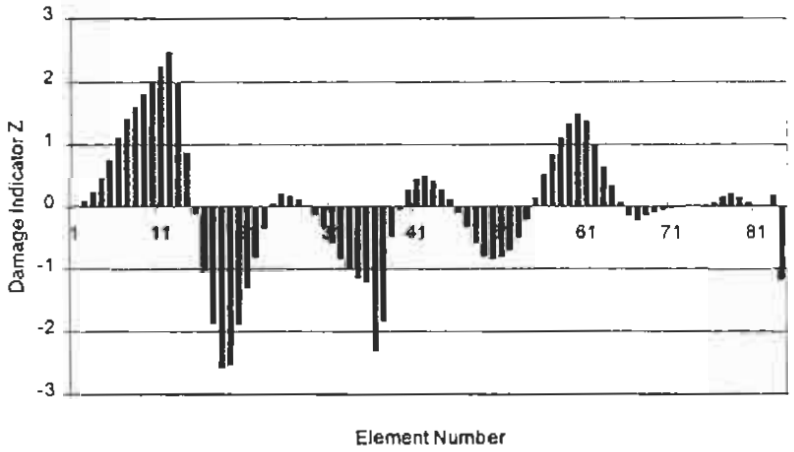

(b)

Figure 3.12 Damage Localization Results Using the Second Bending Mode in the Z-dir. (December 1997): (a) Result using the measurements along the west girder (W1-W13); (b) Result using the measurements along the east girder (E1-E13).

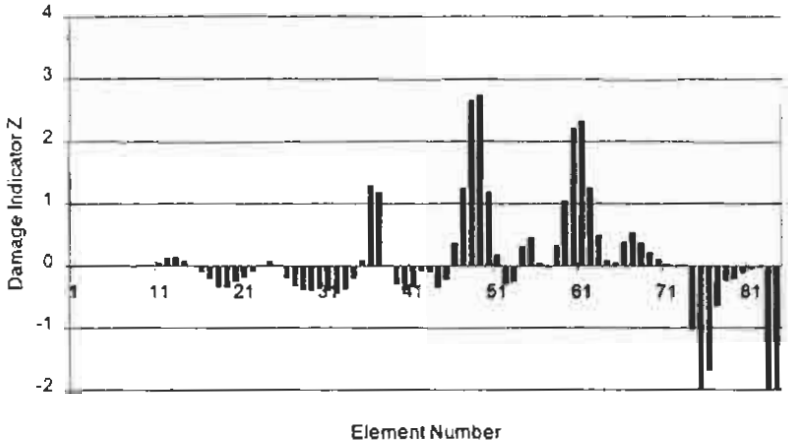

Figure 3.13 Damage Localization Results Using the First Bending Mode in the Y-dir. (December 1997)

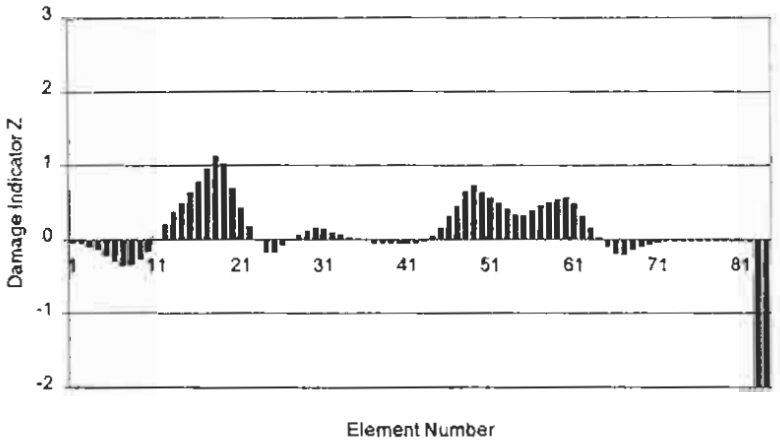

Figure 3.14 Damage Localization Results Using the Second Bending Mode in the Y-dir. (December 1997)

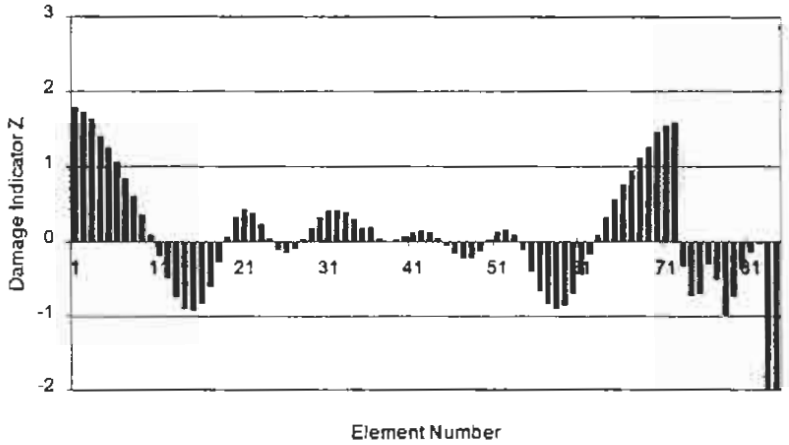

Figure 3.15 Damage Localization Results Using the First Torsional Mode (December 1997)

4. IDENTIFICATION OF THE EXISTING STRUCTURE AS OF SEPTEMBER 1998

4.1 Overview

The objective of this section is to generate an estimate of the appropriate stiffness properties of the Lavic Road Overcrossing using the field data measured in September 1998. The same schematic (Figure 3.1) in the previous section is utilized for systems identification, generation of possible locations and severity of damage in the existing structure, and estimation of the stiffness properties of the existing structure.

4.2 Summary of Modal Analysis

On September 26, 1998 a modal test was performed on the Lavic Road Overcrossing. Temperatures ranged from a low of 60 degrees Fahrenheit to a high of 70 degrees Fahrenheit and no significant wind was observed. The apparatus used in the modal test consisted of a 16-channel signal analyzer, five accelerometers, an impact hammer, and a commercial software package to perform the modal analysis. The same accelerometer layout shown in Figure 3.2 was used for the 1998 measurements. The responses of the structure were measured at 30 locations: 26 locations on the deck (E1-E13 and W1-W13) and 4 locations on the column (C1-C4). For all readings, the structure was impacted in the Z-direction by an instrumented hammer at the midpoint between accelerometers E3 and E4.

Acceleration responses in the X-, Y-, and Z-directions were recorded at all locations. Standard modal analyses were performed on collected data and resonant frequencies and mode shapes were extracted. A detailed description of the field testing and the modal analysis are provided in the Appendix B.

For the measurements in September 1998, the following four modes were

selected: (1) the first bending mode of the deck about the Y-axis; (2) the second bending mode of the deck about the Y-axis; (3) the first torsional mode of the deck about the X-axis; and (4) the second lateral bending mode of the deck about the Z-axis. The frequencies associated with these modes are listed in Table 4.1. Note that the first lateral bending mode of the deck about the Z-axis was not extracted in the modal analysis using the 1998 data.

The modal amplitudes of these modes at each accelerometer location are listed in Tables 4.2 to 4.5. Note that visualizations of the modes are provided in Figures 4.1 to 4.4.

4.3 Development of the Baseline Model

The same FE model of the box girder bridge shown in Figure 3.8 was used to develop a baseline model for the 1998 Lavic Road Overcrossing. With the same initial material properties provided in Section 3.3 and with the measured frequencies of the bridge obtained in September 1998 (See Table 4.1) as the target frequencies, the elements of the stiffness sensitivity matrix, F, listed in Table 4.6 and the elements of the mass sensitivity matrix, G, listed in Table 4.7 were generated and the system material properties were updated until the system converged. The results of this process are shown in Table 4.8. From the table it can be seen that after ten iterations, the differences in the corresponding four frequencies of the identified baseline and the existing structures are 0.7%, 1.0%, 0%, and 0.3%.

Therefore, the model with frequencies of 3.352 Hz for the first bending mode in the Z-direction, 4.885 Hz for the second bending mode in the Z-direction, 6.742 Hz for the first torsional mode, and 8.576 Hz for the second bending mode in the Y-direction is designated as the baseline structure. A dynamic finite element analysis was performed on the baseline structure to generate the corresponding mode shapes. The corresponding modal amplitudes for these modes at the

simulated accelerometer locations are provided in Tables 4.9 to 4.12. The values of identified stiffness parameters for each group are provided in Table 4.13.

4.4 Location of Damage in the Existing Structure

The damage detection model for the location of damage and the estimation of the severity of damage is shown in Figure 3.10 and the sectional properties for the members are listed in Table 3.17. For the two bending modes in the Z-direction and a torsional mode, the deck (i.e., Elements 1 to 72) and the column (i.e., Elements 73-82) are considered as Euler-Bernoulli beam elements and only springs in the Z-direction (i.e., k_z in Figure 3.10) are included in the damage detection model for Elements 83 and 84. For the bending mode in the Y-direction, the deck (i.e., Elements 1 to 72) and the column (i.e., Elements 73-82) are also considered as Euler-Bernoulli beam elements and only springs in the Y-direction (i.e., k_y in Figure 3.10) are included in the damage detection model for Elements 83 and 84.

The location of potential damage is implemented using the same steps provided in the Section 3.4. The results for the predicted damage locations are summarized in Figures 4.5 to 4.8. Note that for the bending modes, the measurements along the west girder (i.e., W1-W13) and the measurements along the east girder (i.e., E1-E13) are used separately.

4.5 Estimation of Damage Magnitude

The damage severity estimation is performed as follows. First, the baseline and post-damage sensitivities are obtained as described in the latter section. Second, the predicted damage locations are obtained from Figures 4.5 to 4.8. Finally, for each predicted damage location, the damage severity are estimated using the severity estimator. The estimated damage severities are listed in Table 4.14. Note that the magnitudes of damage about the X-axis were estimated using

the first torsional mode, the magnitudes of damage about the Y-axis were estimated using the first two bending modes in the Z-direction, and the magnitude of damage about the Z-axis were estimated using the bending mode in the Y-direction. These magnitudes are fractional stiffness changes of those elements.

4.6 Estimation of Structural Properties of the Identified Existing Structure

Using Equation (3.1) and the identified material properties of the baseline structure (see Table 4.13) and member properties (see Table 3.17), the estimated torsional and bending stiffnessess for the deck and the column at Bent #2 of the existing structure are summarized in Table 4.15.

Table 4.1 Measured Frequencies of the Bridge in September 1998

Mode	Frequency (Hz)
1 (First Bending in Z-dir.)	3.374
2 (Second Bending in Z-dir.)	4.839
3 (First Torsion)	6.740
4 (Second Bending in Y-dir.)	8.605

Table 4.2 Modal Coordinates of the First Bending Mode in the Z-direction at 3.374 Hz (Measured FIELD Data, September 1998)

Accelerometer Number	X-Modal Coordinate	Y-Modal Coordinate	Z-Modal Coordinate
W1	-1.13417E-01	-1.16751E-02	3.98363E-02
W2	-3.89946E-02	6.37377E-02	4.11335E-01
W3	-1.08788E-01	-6.83879E-03	7.97703E-01
W4	-1.04180E-02	9.07540E-02	1.00000E+00
W5	-1.30489E-02	3.57443E-02	8.61383E-01
W6	-3.04446E-02	1.01254E-01	5.67753E-01
W7	2.02746E-02	6.17519E-02	1.92683E-02
W8	-2.83539E-02	3.79342E-02	-5.09602E-01
W9	-6.53369E-02	7.77310E-03	-8.68746E-01
W10	-2.42656E-02	8.77974E-02	-8.75094E-01
W11	-5.50093E-02	4.91142E-02	-6.84604E-01
W12	-6.04188E-02	1.13795E-01	-3.60219E-01
W13	-5.01488E-02	4.67395E-02	-1.22052E-02
E1	-5.00912E-02	6.26416E-02	7.77447E-02
E2	-4.24061E-02	5.85007E-02	4.45482E-01
E3	-5.65252E-02	2.48166E-02	5.78758E-01
E4	-1.14204E-01	1.24370E-01	8.13778E-01
E5	-9.29769E-02	8.45869E-02	8.66648E-01
E6	-8.54662E-02	7.25188E-02	2.45679E-01
E7	3.39632E-03	4.36481E-02	-5.09675E-02
E8	-1.18295E-02	5.14805E-02	-4.53587E-01
E9	-3.56727E-02	6.20857E-02	-7.24982E-01
E10	-8.53313E-02	3.84423E-02	-8.24758E-01
E11	-3.10347E-02	5.08333E-02	-6.81746E-01
E12	-5.82786E-02	5.27136E-02	-3.39095E-01
E13	-1.15977E-01	1.58654E-02	-3.67242E-02
C1	1.93401E-02	8.23097E-03	-3.18476E-02
C2	-1.46323E-03	3.42740E-02	2.83989E-02
C3	-3.73318E-02	2.90967E-02	1.23842E-02
C4	-1.27546E-01	4.24876E-02	5.65381E-02

Table 4.3 Modal Coordinates of the Second Bending Mode in the Z-direction at 4.839 Hz (Measured FIELD Data, September 1998)

Accelerometer Number	X-Modal Coordinate	Y-Modal Coordinate	Z-Modal Coordinate
W1	-7.12049E-02	1.16860E-04	4.52587E-03
W2	-1.22090E-02	2.37954E-02	4.48939E-01
W3	-6.79563E-04	-1.91223E-02	7.27498E-01
W4	4.59862E-02	-9.56717E-03	8.14416E-01
W5	4.52596E-02	-2.15721E-02	6.09123E-01
W6	1.95506E-02	2.66358E-02	2.97466E-01
W7	-3.01886E-02	-1.48661E-02	1.21661E-01
W8	-4.61833E-02	-4.25448E-02	3.18781E-01
W9	-6.36082E-02	-4.20279E-02	6.96627E-01
W10	-1.42015E-02	1.39665E-02	1.00000E+00
W11	-4.84980E-03	5.96360E-03	9.02424E-01
W12	3.78115E-02	-4.08486E-02	5.22011E-01
W13	5.20732E-02	-1.30326E-02	1.56796E-02
E1	-6.74512E-02	1.25796E-02	7.27729E-02
E2	-4.87241E-02	-1.11057E-02	5.16378E-01
E3	-3.79859E-02	3.96936E-03	6.57426E-01
E4	-1.12138E-02	3.34755E-04	7.60278E-01
E5	1.45860E-02	-8.74700E-03	6.84957E-01
E6	5.19166E-02	5.83679E-03	1.87543E-01
E7	4.86930E-03	4.89958E-03	2.67600E-01
E8	-1.68797E-02	6.22944E-02	5.81462E-01
E9	-4.33540E-02	2.92717E-02	8.17159E-01
E10	-1.63560E-02	5.92209E-02	9.38264E-01
E11	-2.57602E-02	3.80005E-02	8.76905E-01
E12	6.86020E-02	-1.67698E-02	5.35392E-01
E13	4.08436E-02	-4.24725E-02	-1.03829E-02
C1	5.40346E-03	4.57667E-02	7.12598E-02
C2	-2.90081E-02	4.01153E-02	2.74022E-02
C3	7.88114E-03	-9.35563E-03	1.10986E-02
C4	1.16481E-02	-7.06157E-03	3.37979E-02

Table 4.4 Modal Coordinates of the First Torsional Mode at 6.740 Hz (Measured FIELD Data, September 1998)

Accelerometer Number	X-Modal Coordinate	Y-Modal Coordinate	Z-Modal Coordinate
W1	-7.09689E-02	-4.27519E-02	6.16230E-02
W2	-4.47134E-02	-6.22862E-02	4.74838E-01
W3	-3.53788E-02	-6.21865E-02	6.78980E-01
W4	-1.83792E-02	-3.64395E-03	7.89162E-01
W5	5.35953E-03	-4.96844E-02	9.03557E-01
W6	-2.05820E-03	-1.87081E-02	8.68837E-01
W7	-8.75851E-03	-4.63276E-03	8.11940E-01
W8	9.93393E-03	1.63385E-02	8.69013E-01
W9	3.81770E-02	8.74345E-03	8.83997E-01
W10	3.99808E-02	-1.89133E-02	7.53211E-01
W11	4.46202E-02	-2.28289E-02	6.00087E-01
W12	7.13296E-02	-3.65088E-02	3.73438E-01
W13	5.91874E-02	-2.85639E-02	1.04297E-02
E1	8.85697E-02	-6.08678E-02	-8.85479E-02
E2	5.60939E-02	-8.09855E-02	-4.62319E-01
E3	4.48144E-02	-5.07678E-02	-4.43196E-01
E4	5.92784E-02	-2.96906E-02	-6.32164E-01
E5	4.63609E-02	-4.70724E-02	-1.00000E+00
E6	-1.74707E-02	1.02751E-02	-5.43258E-01
E7	-2.29094E-02	-3.52750E-02	-6.25020E-01
E8	9.81428E-03	1.42088E-02	-7.75190E-01
E9	-4.17913E-02	-1.81705E-02	-7.86335E-01
E10	-4.62720E-02	-2.16613E-02	-6.88209E-01
E11	-3.08598E-02	-5.30026E-02	-6.00388E-01
E12	-5.48763E-02	-4.69103E-02	-4.14972E-01
E13	-5.11754E-02	-2.28950E-02	-4.58173E-02
C1	-2.26336E-02	7.96678E-02	4.53851E-02
C2	-1.56523E-02	1.68201E-01	9.09822E-02
C3	-7.66929E-04	3.60275E-01	8.23663E-02
C4	-3.44065E-02	4.69467E-01	2.86090E-02

Table 4.5 Modal Coordinates of the Second Bending Mode in the Y-direction at 8.605 Hz (Measured FIELD Data, September 1998)

Accelerometer Number	X-Modal Coordinate	Y-Modal Coordinate	Z-Modal Coordinate
W1	-1.36464E-01	3.05890E-01	-8.04834E-02
W2	-1.17777E-01	5.85781E-01	-5.61779E-01
W3	-1.30564E-01	8.43948E-01	-6.12710E-01
W4	-5.94930E-02	8.50140E-01	-4.73756E-01
W5	5.12588E-02	7.50048E-01	-3.55093E-01
W6	3.51241E-02	4.48500E-01	-1.10638E-01
W7	5.24912E-02	-1.48749E-01	1.71666E-01
W8	2.15761E-02	-6.22781E-01	3.89858E-01
W9	-1.78539E-02	-8.43648E-01	5.58949E-01
W10	-7.75355E-02	-9.51905E-01	5.43430E-01
W11	-1.21556E-01	-8.85111E-01	3.90832E-01
W12	-1.93640E-01	-6.28387E-01	9.82037E-02
W13	-2.07635E-01	-2.32579E-01	4.17206E-03
E1	-4.41766E-02	2.55420E-01	2.37242E-01
E2	1.27151E-01	5.99012E-01	5.49452E-01
E3	4.66556E-02	9.15568E-01	-3.08044E-01
E4	-1.84311E-01	9.83242E-01	-2.06703E-01
E5	-1.95075E-01	8.92040E-01	4.60702E-01
E6	-5.44604E-02	1.63167E-01	1.56218E-01
E7	-1.98332E-01	-2.79028E-01	-2.80407E-02
E8	-2.05336E-01	-6.54582E-01	-1.86748E-01
E9	-1.43213E-01	-8.96902E-01	-3.63476E-01
E10	-8.42546E-02	-1.00000E+00	-5.61389E-01
E11	-3.48005E-02	-8.57540E-01	-3.70043E-01
E12	4.40510E-02	-5.78589E-01	1.59320E-02
E13	7.31355E-02	-2.55341E-01	-4.89300E-02
C1	1.18818E-01	-6.27400E-03	2.22787E-03
C2	5.26548E-02	-1.97315E-04	-4.23762E-02
C3	-1.38479E-02	4.13317E-02	-3.31663E-02
C4	5.40527E-02	-6.28255E-02	-4.38183E-02

Table 4.6 Stiffness Sensitivity Matrix F for the System (September 1998)

Mode	Group Identification		
	Group 1 (Deck)	Group 2 (Column and Footing)	Group 3 (Abutment-Soil System)
1 (First Bending in Z-dir.)	0.8591	0.0813	0.0595
2 (Second Bending in Z-dir.)	0.7929	0.0399	0.1672
3 (First Torsion)	0.4742	0.2377	0.2880
4 (Second Bending in Y-dir.)	0.6090	0.0020	0.3891

Table 4.7 Mass Sensitivity Matrix G for the System (September 1998)

Mode	Group 1 and Group 2
1 (First Bending in Z-dir.)	0.9093
2 (Second Bending in Z-dir.)	0.9090
3 (First Torsion)	0.9090
4 (Second Bending in Y-dir.)	0.9093

Table 4.8 System Identification (September 1998)

Mode	Frequency of Initial FE model	Updated Frequencies (Hz)			Frequency of Target Structure	Error (%)	
		Iter. 2	Iter. 6	Iter. 10		Initial	Final
1	2.950	3.300	3.354	3.352	3.374	12.6	0.7
2	4.249	4.744	4.880	4.885	4.839	12.2	1.0
3	6.228	6.453	6.710	6.742	6.740	7.6	0.0
4	7.163	8.529	8.585	8.576	8.605	16.8	0.3

Table 4.9 Modal Coordinates of the First Bending Mode in the Z-direction at 3.352 Hz (Identified Baseline Data, September 1998)

Accelerometer Number	X-Modal Coordinate	Y-Modal Coordinate	Z-Modal Coordinate
W1	-1.7970E-01	3.0946E-04	3.5814E-02
W2	-1.7330E-01	-7.1200E-05	5.3120E-01
W3	-1.5130E-01	-1.9704E-04	8.5470E-01
W4	-1.1450E-01	-1.9854E-04	9.9460E-01
W5	-7.9287E-02	-2.2706E-04	8.4620E-01
W6	-5.5585E-02	-2.7622E-04	4.7270E-01
W7	-5.1104E-02	-6.6478E-04	1.1696E-02
W8	-5.9835E-02	1.1335E-04	-4.0670E-01
W9	-8.1560E-02	1.7819E-04	-7.2210E-01
W10	-1.1100E-01	1.6719E-04	-8.4120E-01
W11	-1.4110E-01	1.6411E-04	-7.2170E-01
W12	-1.5920E-01	5.1088E-05	-4.5110E-01
W13	-1.6530E-01	-3.3318E-04	-3.0358E-02
E1	-1.7970E-01	-3.0946E-04	3.5814E-02
E2	-1.7330E-01	7.1200E-05	5.3120E-01
E3	-1.5130E-01	1.9704E-04	8.5470E-01
E4	-1.1450E-01	1.9854E-04	9.9460E-01
E5	-7.9287E-02	2.2706E-04	8.4620E-01
E6	-5.5585E-02	2.7622E-04	4.7270E-01
E7	-5.1104E-02	6.6478E-04	1.1696E-02
E8	-5.9835E-02	-1.1335E-04	-4.0670E-01
E9	-8.1560E-02	-1.7819E-04	-7.2210E-01
E10	-1.1100E-01	-1.6719E-04	-8.4120E-01
E11	-1.4110E-01	-1.6411E-04	-7.2170E-01
E12	-1.5920E-01	-5.1088E-05	-4.5110E-01
E13	-1.6530E-01	3.3318E-04	-3.0358E-02
C1	-4.7675E-02	0.0000E+00	5.8072E-03
C2	-7.4485E-02	0.0000E+00	6.2540E-03
C3	-1.5250E-01	7.0105E-14	7.2086E-03
C4	-2.1690E-01	1.3855E-13	8.1930E-03

Table 4.10 Modal Coordinates of the Second Bending Mode in the Z-direction at 4.885 Hz(Identified Baseline Data, September 1998)

Accelerometer Number	X-Modal Coordinate	Y-Modal Coordinate	Z-Modal Coordinate
W1	-8.6987E-02	1.6113E-04	5.4831E-02
W2	-8.4596E-02	-1.7411E-04	4.3070E-01
W3	-5.7496E-02	-3.5690E-04	7.1000E-01
W4	-1.1740E-02	-3.5211E-04	8.1550E-01
W5	2.6431E-02	-5.0780E-04	6.5850E-01
W6	3.8560E-02	-1.4313E-03	3.7880E-01
W7	7.7957E-03	-1.1232E-02	2.3890E-01
W8	-2.0228E-02	-1.6226E-03	4.7310E-01
W9	-3.1002E-03	-6.1379E-04	8.1170E-01
W10	4.1096E-02	-4.2944E-04	9.8680E-01
W11	9.2840E-02	-4.2558E-04	8.5690E-01
W12	1.2360E-01	-1.8836E-04	5.2630E-01
W13	1.2770E-01	3.0952E-04	6.5102E-02
E1	-8.6987E-02	-1.6113E-04	5.4831E-02
E2	-8.4596E-02	1.7411E-04	4.3070E-01
E3	-5.7496E-02	3.5690E-04	7.1000E-01
E4	-1.1740E-02	3.5211E-04	8.1550E-01
E5	2.6431E-02	5.0780E-04	6.5850E-01
E6	3.8560E-02	1.4313E-03	3.7880E-01
E7	7.7957E-03	1.1232E-02	2.3890E-01
E8	-2.0228E-02	1.6226E-03	4.7310E-01
E9	-3.1002E-03	6.1379E-04	8.1170E-01
E10	4.1096E-02	4.2944E-04	9.8680E-01
E11	9.2840E-02	4.2558E-04	8.5690E-01
E12	1.2360E-01	1.8836E-04	5.2630E-01
E13	1.2770E-01	-3.0952E-04	6.5102E-02
C1	6.3667E-03	-3.9134E-13	1.2140E-01
C2	9.8951E-03	1.5599E-13	1.3050E-01
C3	1.9889E-02	5.8806E-13	1.4990E-01
C4	2.7971E-02	3.0503E-13	1.7000E-01

Table 4.11 Modal Coordinates of the First Torsional Mode at 6.742 Hz (Identified Baseline Data, September 1998)

Accelerometer Number	X-Modal Coordinate	Y-Modal Coordinate	Z-Modal Coordinate
W1	-6.0035E-02	-1.7890E-01	2.2730E-01
W2	-5.6005E-02	-1.3370E-01	4.0130E-01
W3	-5.0438E-02	-1.0080E-01	5.2670E-01
W4	-3.9720E-02	-6.4669E-02	6.4270E-01
W5	-2.4934E-02	-3.8303E-02	7.1890E-01
W6	-8.9159E-03	-2.4407E-02	7.5330E-01
W7	2.9894E-03	-2.4270E-02	7.4950E-01
W8	1.4089E-02	-3.0394E-02	7.4550E-01
W9	2.8343E-02	-4.8316E-02	7.0630E-01
W10	4.1116E-02	-7.5741E-02	6.2900E-01
W11	5.0123E-02	-1.1010E-01	5.1540E-01
W12	5.4828E-02	-1.4000E-01	3.9440E-01
W13	5.8455E-02	-1.8150E-01	2.2790E-01
E1	6.0035E-02	-1.7890E-01	-2.2730E-01
E2	5.6005E-02	-1.3370E-01	-4.0130E-01
E3	5.0438E-02	-1.0080E-01	-5.2670E-01
E4	3.9720E-02	-6.4669E-02	-6.4270E-01
E5	2.4934E-02	-3.8303E-02	-7.1890E-01
E6	8.9159E-03	-2.4407E-02	-7.5330E-01
E7	-2.9894E-03	-2.4270E-02	-7.4950E-01
E8	-1.4089E-02	-3.0394E-02	-7.4550E-01
E9	-2.8343E-02	-4.8316E-02	-7.0630E-01
E10	-4.1116E-02	-7.5741E-02	-6.2900E-01
E11	-5.0123E-02	-1.1010E-01	-5.1540E-01
E12	-5.4828E-02	-1.4000E-01	-3.9440E-01
E13	-5.8455E-02	-1.8150E-01	-2.2790E-01
C1	4.0851E-10	7.3939E-02	-3.7625E-11
C2	-5.7261E-11	1.0730E-01	-3.5659E-11
C3	-6.8399E-10	2.6550E-01	-3.0887E-11
C4	-6.9165E-10	4.1990E-01	-2.5532E-11

Table 4.12 Modal Coordinates of the Second Bending Mode in the Y-direction at 8.576 Hz (Identified Baseline Data, September 1998)

Accelerometer Number	X-Modal Coordinate	Y-Modal Coordinate	Z-Modal Coordinate
W1	-1.3950E-01	5.9300E-01	-3.2040E-01
W2	-1.0280E-01	8.3800E-01	-3.2210E-01
W3	-4.3528E-02	9.7830E-01	-3.1010E-01
W4	5.7175E-02	9.6860E-01	-2.6070E-01
W5	1.5390E-01	7.5670E-01	-1.8410E-01
W6	2.1720E-01	3.8540E-01	-8.8107E-02
W7	2.3580E-01	-5.0173E-02	7.8662E-03
W8	2.0760E-01	-4.5890E-01	9.8444E-02
W9	1.4020E-01	-7.9090E-01	1.8700E-01
W10	4.5536E-02	-9.6880E-01	2.5700E-01
W11	-4.9305E-02	-9.6040E-01	3.0240E-01
W12	-1.0380E-01	-8.2030E-01	3.1380E-01
W13	-1.3870E-01	-5.8660E-01	3.1470E-01
E1	1.3950E-01	5.9300E-01	3.2040E-01
E2	1.0280E-01	8.3800E-01	3.2210E-01
E3	4.3528E-02	9.7830E-01	3.1010E-01
E4	-5.7175E-02	9.6860E-01	2.6070E-01
E5	-1.5390E-01	7.5670E-01	1.8410E-01
E6	-2.1720E-01	3.8540E-01	8.8107E-02
E7	-2.3580E-01	-5.0173E-02	-7.8662E-03
E8	-2.0760E-01	-4.5890E-01	-9.8444E-02
E9	-1.4020E-01	-7.9090E-01	-1.8700E-01
E10	-4.5536E-02	-9.6880E-01	-2.5700E-01
E11	4.9305E-02	-9.6040E-01	-3.0240E-01
E12	1.0380E-01	-8.2030E-01	-3.1380E-01
E13	1.3870E-01	-5.8660E-01	-3.1470E-01
C1	2.0690E-08	-3.9252E-03	1.3948E-09
C2	-2.7631E-09	-5.7749E-03	1.2950E-09
C3	-3.4524E-08	-1.5648E-02	1.0592E-09
C4	-3.5247E-08	-2.7938E-02	8.0144E-10

Table 4.13 Identified Material Properties of the Baseline Structure (September 1998)

	Group 1 (Deck)	Group 2 (Column and Footing)	Group 3 (Abutment-Soil System)
E (lb/ft^2)	488.41×10^6 (3392 ksi)	208.56×10^6 (1448 ksi)	
k (lb/ft)	-	-	22.90×10^6
ρ ($lb \cdot s^2/ft^4$)	3.871	3.871	

Table 4.14 Predicted Damage Magnitudes (September 1998)

Element No.	Damage Severity, α_i		
	about X-axis	about Y-axis	about Z-axis
1	-0.11	-	-
2	-0.11	-	-
3	-0.09	-	-
19	-0.23	-	-
20	-0.28	-	-
21	-0.29	-	-
23	-	-0.32	-0.40
24	-	-0.39	-0.44
25	-	-0.40	-0.44
26	-	-0.24	-0.40
27	-0.44	-	-
28	-0.46	-	-
29	-0.48	-0.40	-0.45
30	-0.48	-0.44	-0.47
31	-	-0.45	-0.48
32	-	-0.42	-
36	-	-0.48	-
37	-	-0.47	-
46	-	-0.22	-
47	-	-0.24	-
48	-	-0.26	-
49	-	-0.24	-
50	-	-0.16	-
54	-	-0.08	-
55	-	-0.11	-
56	-	-0.11	-
57	-	-0.11	-
73	-	-0.46	-
74	-	-0.45	-
75	-	-0.44	-
76	-	-0.47	-
77	-	-0.47	-
78	-	-0.48	-
79	-	-0.48	-

Table 4.15 Bending (EI) and Torsional (GJ) Stiffnesses of the Existing Structure (September 1998)

	Element No.	EI_{yy} (lb·ft²)	EI_{zz} (lb·ft²)	GJ (lb·ft²)
	1	1.7290E+11	1.5063E+12	7.3007E+11
	2	1.7290E+11	1.5063E+12	7.3007E+11
	3	1.7290E+11	1.5063E+12	7.3007E+11
	4	1.6948E+11	1.4052E+12	6.8462E+11
	5	1.6948E+11	1.4052E+12	6.8462E+11
	6	1.6948E+11	1.4052E+12	6.8462E+11
	7	1.6948E+11	1.4052E+12	6.8462E+11
	8	1.6948E+11	1.4052E+12	6.8462E+11
	9	1.6948E+11	1.4052E+12	6.8462E+11
	10	1.6948E+11	1.4052E+12	6.8462E+11
	11	1.6948E+11	1.4052E+12	6.8462E+11
	12	1.6948E+11	1.4052E+12	6.8462E+11
	13	1.6948E+11	1.4052E+12	6.8462E+11
	14	1.6948E+11	1.4052E+12	6.8462E+11
	15	1.6948E+11	1.4052E+12	6.8462E+11
	16	1.6948E+11	1.4052E+12	6.8462E+11
	17	1.6948E+11	1.4052E+12	6.8462E+11
	18	1.6948E+11	1.4052E+12	6.8462E+11
	19	1.6948E+11	1.4052E+12	6.8462E+11
	20	1.6948E+11	1.4052E+12	6.8462E+11
	21	1.6948E+11	1.4052E+12	6.8462E+11
	22	1.6948E+11	1.4052E+12	6.8462E+11
Concrete	23	1.1525E+11	8.4309E+11	4.1667E+11
Box Girder	24	1.0547E+11	8.4350E+11	4.1260E+11
	25	1.0374E+11	8.4350E+11	4.1184E+11
	26	1.3140E+11	9.0375E+11	4.5007E+11
	27	1.7680E+11	1.6083E+12	7.7615E+11
	28	1.7680E+11	1.6083E+12	7.7615E+11
	29	1.0608E+11	8.8458E+11	4.3072E+11
	30	1.0120E+11	9.0600E+11	4.3791E+11
	31	9.9391E+10	8.8891E+11	4.2969E+11
	32	1.0481E+11	1.7094E+12	7.8880E+11
	33	1.8267E+11	1.7607E+12	8.4495E+11
	34	1.8267E+11	1.7607E+12	8.4495E+11
	35	1.8267E+11	1.7607E+12	8.4495E+11
	36	1.9048E+11	5.1532E+12	2.3233E+12
	37	1.9414E+11	5.1532E+12	2.3249E+12
	38	1.8267E+11	1.7607E+12	8.4495E+11
	39	1.8267E+11	1.7607E+12	8.4495E+11
	40	1.8267E+11	1.7607E+12	8.4495E+11
	41	1.8071E+11	1.7094E+12	8.2180E+11

Table 4.15 Continued

	Element No.	EI_{yy} (lb·ft²)	EI_{zz} (lb·ft²)	GJ (lb·ft²)
Concrete Box Girder	42	1.8071E+11	1.7094E+12	8.2180E+11
	43	1.8071E+11	1.7094E+12	8.2180E+11
	44	1.7680E+11	1.6083E+12	7.7615E+11
	45	1.7680E+11	1.6083E+12	7.7615E+11
	46	1.3791E+11	1.6083E+12	7.5924E+11
	47	1.3140E+11	1.5063E+12	7.1203E+11
	48	1.2794E+11	1.5063E+12	7.1052E+11
	49	1.3140E+11	1.5063E+12	7.1203E+11
	50	1.4236E+11	1.4052E+12	6.7283E+11
	51	1.6948E+11	1.4052E+12	6.8462E+11
	52	1.6948E+11	1.4052E+12	6.8462E+11
	53	1.6948E+11	1.4052E+12	6.8462E+11
	54	1.5592E+11	1.4052E+12	6.7873E+11
	55	1.5084E+11	1.4052E+12	6.7652E+11
	56	1.5084E+11	1.4052E+12	6.7652E+11
	57	1.5084E+11	1.4052E+12	6.7652E+11
	58	1.6948E+11	1.4052E+12	6.8462E+11
	59	1.6948E+11	1.4052E+12	6.8462E+11
	60	1.6948E+11	1.4052E+12	6.8462E+11
	61	1.6948E+11	1.4052E+12	6.8462E+11
	62	1.6948E+11	1.4052E+12	6.8462E+11
	63	1.6948E+11	1.4052E+12	6.8462E+11
	64	1.6948E+11	1.4052E+12	6.8462E+11
	65	1.6948E+11	1.4052E+12	6.8462E+11
	66	1.6948E+11	1.4052E+12	6.8462E+11
	67	1.6948E+11	1.4052E+12	6.8462E+11
	68	1.6948E+11	1.4052E+12	6.8462E+11
	69	1.6948E+11	1.4052E+12	6.8462E+11
	70	1.7290E+11	1.5063E+12	7.3007E+11
	71	1.7290E+11	1.5063E+12	7.3007E+11
	72	1.7290E+11	1.5063E+12	7.3007E+11
Column	73	3.4913E+09	-	4.3290E+09
	74	3.5559E+09	-	4.3571E+09
	75	3.6206E+09	-	4.3852E+09
	76	3.4266E+09	-	4.3009E+09
	77	3.4266E+09	-	4.3009E+09
	78	3.3620E+09	-	4.2728E+09
	79	3.3620E+09	-	4.2728E+09
	80	6.4654E+09	-	5.6221E+09
	81	6.4654E+09	-	5.6221E+09
	82	6.4654E+09	-	5.6221E+09

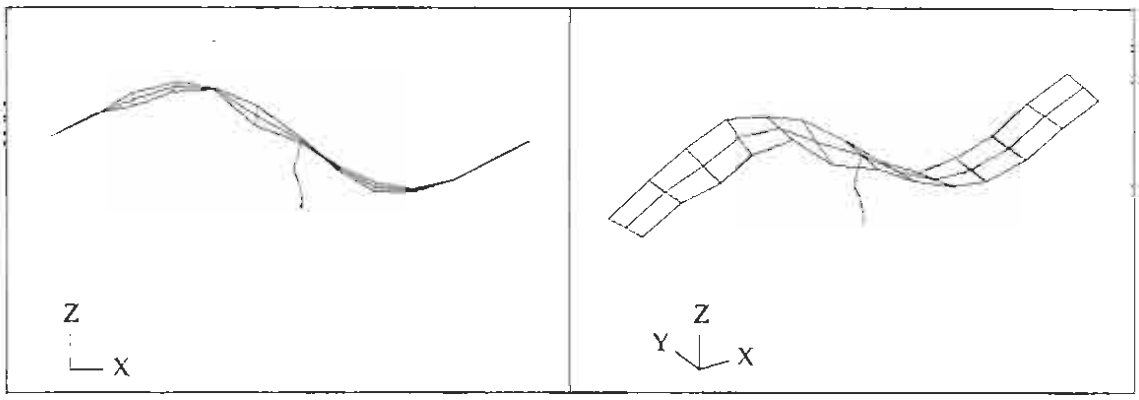

Figure 4.1 First Bending Mode Identified in the Z-direction at 3.374Hz (September 1998)

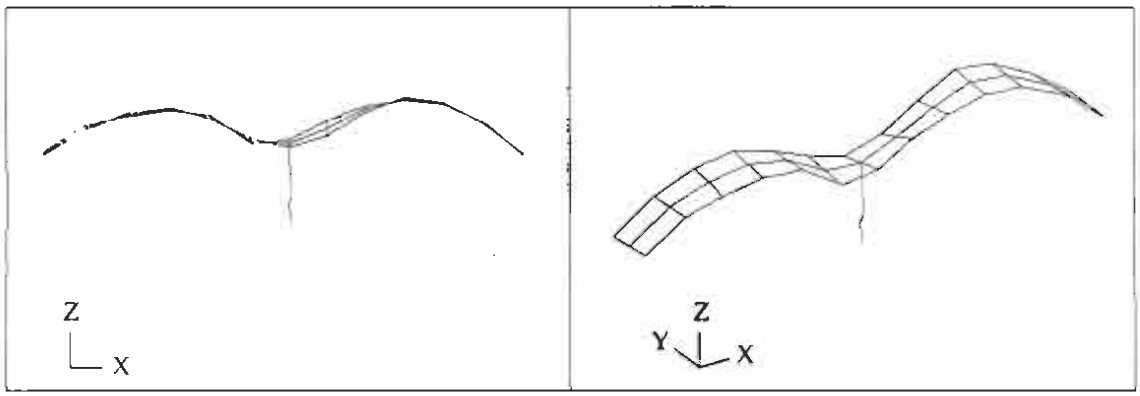

Figure 4.2 Second Bending Mode Identified in the Z-direction at 4.839Hz (September 1998)

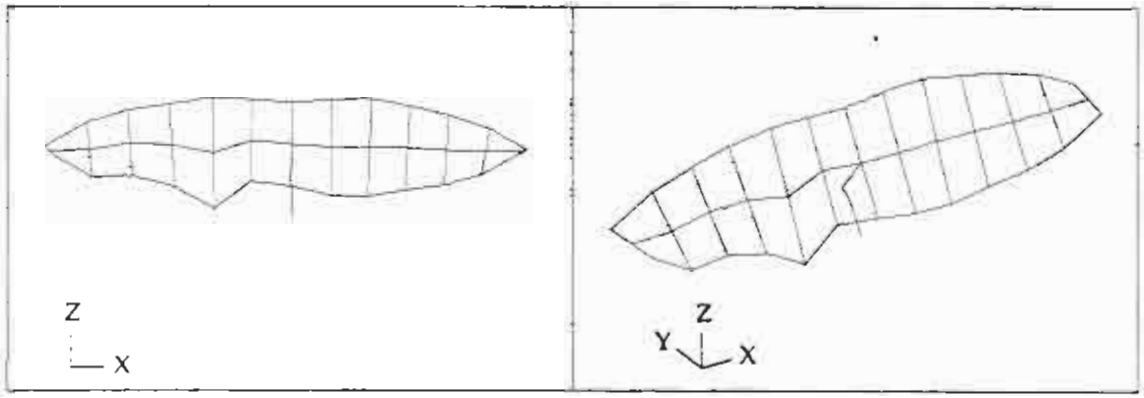

Figure 4.3 First Torsional Mode Identified at 6.740Hz (September 1998)

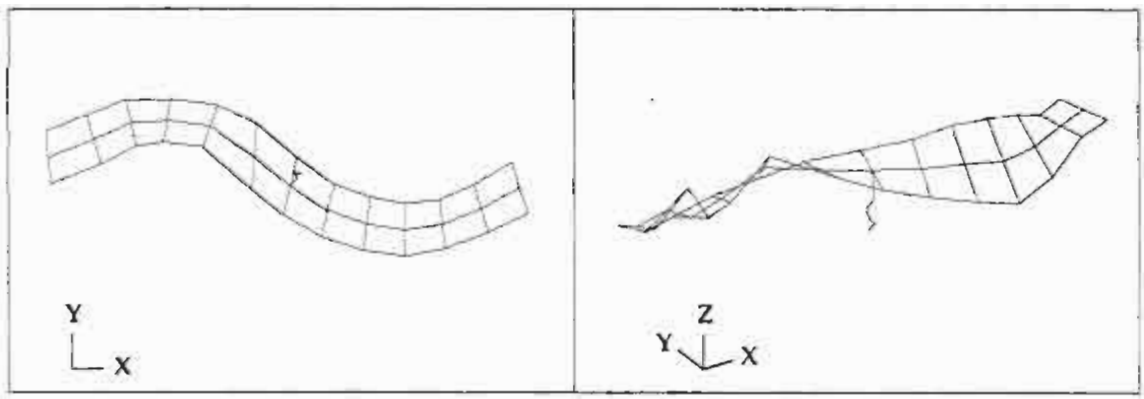

Figure 4.4 Second Bending Mode Identified in the Y-direction at 8.605Hz (September 1998)

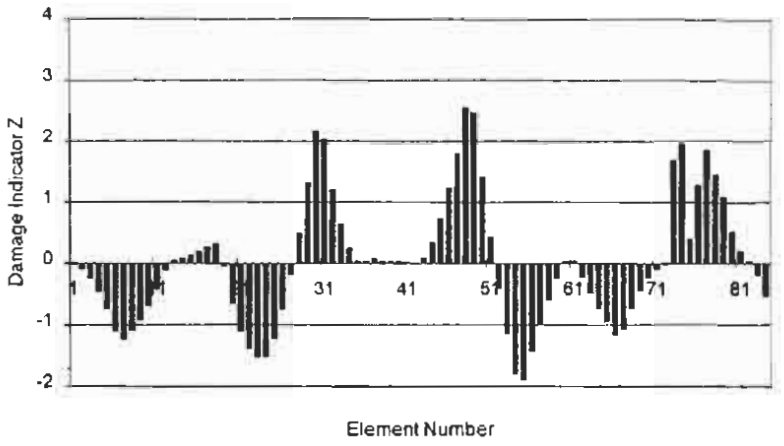

(a)

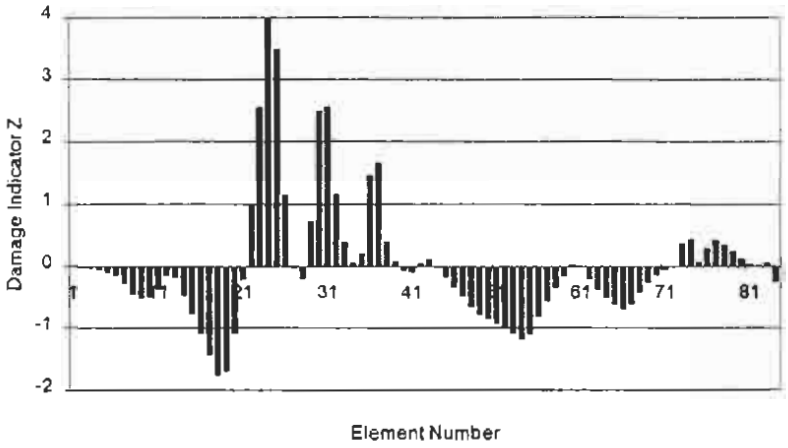

(b)

Figure 4.5 Damage Localization Results Using the First Bending Mode in the Z-dir. (September 1998): (a) Result using the measurements along the west girder (W1-W13);(b) Result using the measurements along the east girder (E1-E13).

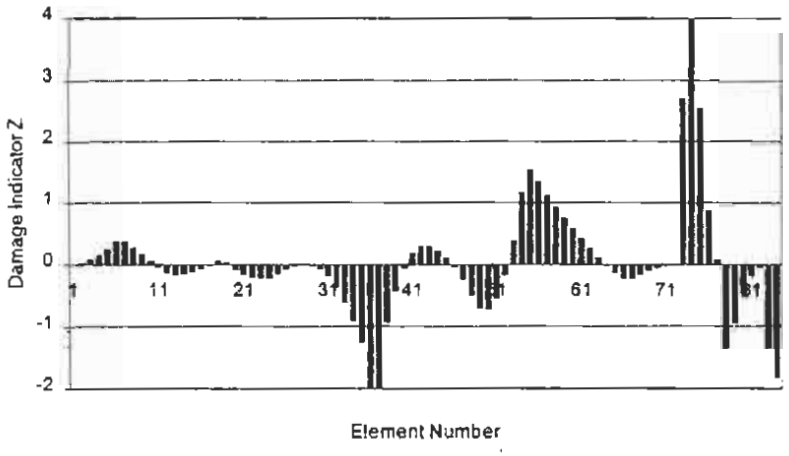

(a)

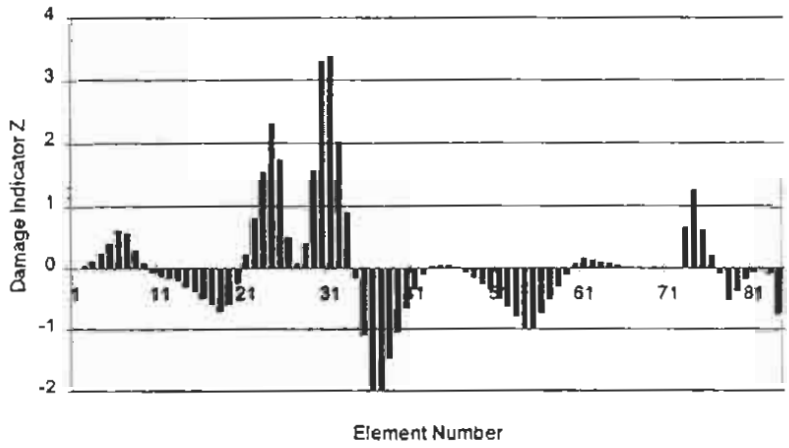

(b)

Figure 4.6 Damage Localization Results Using the Second Bending Mode in the Z-dir. (September 1998): (a) Result using the measurements along the west girder (W1-W13); (b) Result using the measurements along the east girder (E1-E13).

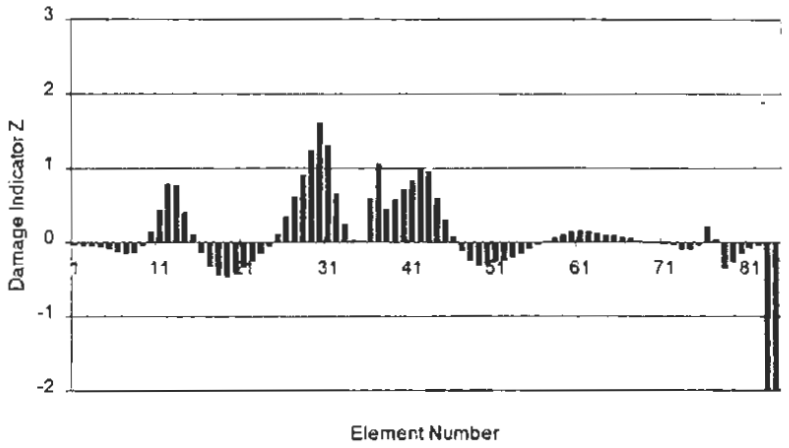

(a)

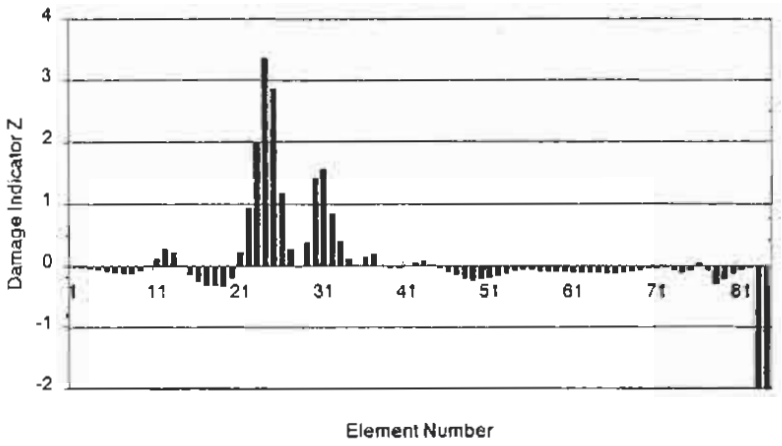

(b)

Figure 4.7 Damage Localization Results Using the Second Bending Mode in the Y-dir. (September 1998): (a) Result using the measurements along the west girder (W1-W13); (b) Result using the measurements along the east girder (E1-E13).

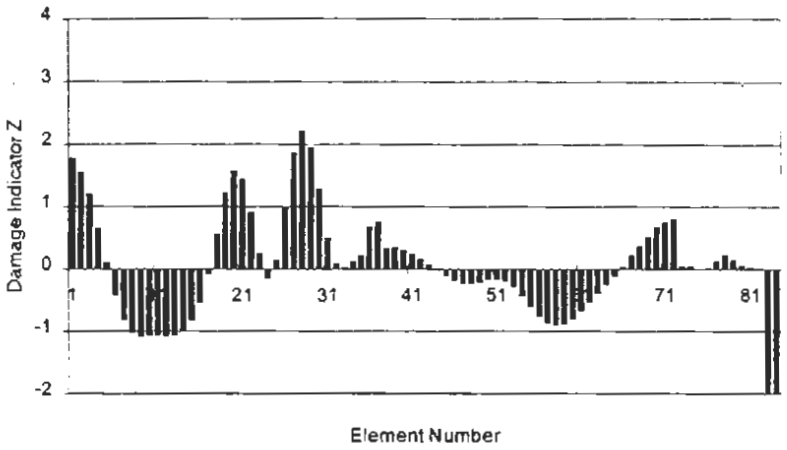

Figure 4.8 Damage Localization Results Using the First Torsional Mode (September 1998)

5. ESTIMATION OF THE DETERIORATION RATES OF THE STRUCTURAL COMPONENTS

5.1 Overview

The objective of this section is to investigate the existence of possible degradation of the integrity of the structure for the time period between the tests. Here, a decrease in a stiffness parameter is considered to be an indicator of degradation. Three approaches were used to estimate any potential degradation in the structural stiffness of the bridge. In the first approach, the gross stiffness properties obtained in 1997 and 1998 for the major superstructure and substructure elements were compared. In the second approach, the stiffness properties of the structure based on the damage detection model shown in Figure 3.10 were compared. In the third approach, the measured modal data obtained in 1997 and 1998 were used with the damage detection model, shown in Figure 3.10, to evaluate any change in structural stiffness during that period of time.

5.2 Comparison of the 1997 and 1998 Properties via Identified Baseline Structures

The properties of interest in this comparison include the average stiffness and density of the deck, the average stiffness and density of the column, and the stiffness of the abutment-soil system. The stiffness properties for the 1997 and 1998 baseline structures are listed, respectively, in Tables 3.16 and 4.13. From the tables, the following observations regarding the average stiffness properties can be made:

1. The elastic modulus (E) of the deck (Group 1) apparently increased 8% from 3146 ksi (December 1997) to 3392 ksi (September 1998);
2. The elastic modulus (E) of the column at Bent #2 (Group 2) decreased 43% from 2528 ksi (December 1997) to 1448 ksi (September 1998); and

3. The effective spring constant, $k_{Abut+Soil}$, for abutments-soil system decreased 38% from 36.98×10^6 lb/ft (December 1997) to 22.90×10^6 lb/ft (September 1998).

These results are shown graphically in Figure 5.1.

With regards to the average mass properties of the structure during the referenced period, the following observation can be made:

1. The mass density of the bridge in December 1997 decreased 17% from 4.65 $lb \cdot s^2/ft^4$ to 3.87 $lb \cdot s^2/ft^4$ in September 1998.

In summary, we interpret the potential changes in stiffness and mass properties as follows:

1. During the period of interest there was no significant change in the average stiffness of the deck;
2. The degradation in the stiffnesses of the column and abutments was significant; and
3. The density of the superstructure appears to change significantly during the wet months and dry months.

5.3 Comparison of the Stiffness Properties via Damage Detection

In this comparison, the properties of interest are referenced to the damage detection model shown in Figure 3.10. Recall that in the damage detection model Elements 1-72 represent approximately 3.4 ft. linear sections of the deck, Elements 73-82 represent 3.5 ft. linear sections of the column, and Elements 83 and 84, respectively, represent the south and north abutment systems. The bending, torsional, or axial stiffnesses associated with each element are summarized in Table 3.19 and Table 4.15 for the 1997 and 1998 structures, respectively.

Comparisons of the stiffness properties for 1997 and 1998 are shown in Figures 5.2 to 5.4. In Figure 5.2 relative stiffnesses changes (bending stiffness about the Y-axis, bending stiffness about the Z-axis, and torsional stiffness) for the

deck elements are presented. A depression in the stiffness ratio, e.g., as indicated in Figure 5.2(a) in the region of Elements 6-13 is generally interpreted as a loss in stiffness. Note, however, the same depression could have been caused by an increase in mass in that region. It is seen that except for a few localized regions, the stiffness of the deck elements is essentially the same for the period under study.

In Figure 5.3, the relative stiffness changes for the bending stiffness about the Y-axis and the torsional stiffness of the column are presented. In both Figure 5.3(a) and Figure 5.3(b), during the period of interest a significant drop (i.e., approximately 46% from the baseline value (Elements 80-82) in bending and 23% in torsion) in the stiffness of the column is indicated. This stiffness drop cannot be explained by any variation in mass of the column.

The relative stiffness changes for the abutments are presented in Figure 5.4. Note that between 1997 and 1998 a decrease of approximately 38% in the effective axial stiffness of the abutments has occurred.

In summary, the change in the stiffness properties for the structure in the 1997-1998 period, using the combination of damage detection and systems identification as a basis, are as follows:

1. Except for possible local regions of damage on the deck, there has been no deterioration of the deck; and
2. A decrease in the bending and torsional stiffnesses has occurred in Elements 73 to 79 of the column.

5.4 Comparison of the 1997 and 1998 Structures by Direct Utilization of 1997 and 1998 Data

From the field data phases, modal information was collected on the frequency as well as the mode shapes of the structure. The reader may also note that two distinct approaches are used here to probe the properties of the structure; namely, the frequency-based approach which relies on the sensitivity equations,

and the mode shape-based approach which relies on the damage index and pattern recognition. Here the actual frequency and mode shape data gathered in 1997 and 1998 were used to examine the possible degradation of the structure in the period of interest.

5.4.1 Determination of Changes in the Average Properties of the Structure via Sensitivity Equations and Frequencies

In this comparison, the selected structural elements are the deck, the column, and the abutment-soil system. Changes in the mass and stiffness of the structure were determined as explained below. The fundamental equation used to estimate the changes is the same sensitivity equation described in Appendix A:

$$Z = F\alpha - G\beta \tag{5.1}$$

in which:

Z = a k x 1 matrix containing the fractional changes of the k measured frequencies;

α = a b x 1 matrix containing the fractional changes in stiffness of the selected structural elements;

F = a k x b matrix defining the sensitivity between Z and α;

β = a v x 1 matrix countering the fractional change in mass of the selected mass elements; and

G = a k x v matrix defining the sensitivity between G and β.

The elements of the matrix Z are obtained using the measured frequencies in 1997 and 1998 that are listed in Table 3.1 and Table 4.1, respectively. The stiffness-frequency sensitivity matrix, F, of interest here is given in Table 4.6. Similarly, the mass-frequency sensitivity matrix, G, is given in Table 4.7.

With Z, F, and G defined, the above equation is solved, using a combination of iterative and generalized inverse techniques, to yield the average changes in stiffness of the elements and the change in density of the deck and column combined. Using the above procedure, the following results were obtained for the period from December 1997 to September 1998:

1. The average density of the deck and column decreased by 21%;
2. The stiffness of the deck apparently increased by 9%;
3. The stiffness of the column decreased by 53%; and
4. The stiffness of the abutment-soil system decreased by 42%.

5.4.2 Determination of Changes via Damage Detection using Mode Shapes

In this comparison, the properties of interest are referenced to the damage detection model shown in Figure 3.10. The measured modal amplitudes for December 1997 are listed in Tables 3.2 to 3.6. Similarly, the measured modal amplitudes for September 1998 are listed in Tables 4.2 to 4.5. Using the 1997 mode shapes as a reference, damage localization and severity estimation calculation were performed as described in Appendix A.

Comparison of the stiffness properties for 1997 and 1998 are shown in Figures 5.5 to 5.7. In Figure 5.5, the estimated stiffness degradation for bending about the Y-axis and the Z-axis, as well as twisting about the X-axis are presented. From the figure, it can be concluded that significant local changes in stiffness of the deck, particularly in the central region between Elements 21 and 44 may have occurred. In Figure 5.6, results indicate that approximately a 40% reduction in the bending stiffness and a 20% reduction in the torsional stiffness have occurred in Elements 73 to 77 of the column. Finally, the mode shape data do not predict any changes in the stiffness of the abutments for the period of interest.

5.5 Summary of Major Findings

Findings based on individual systems identification of the 1997 and 1998 structures, damage detection and systems identification, and the direct comparison of the 1997 and 1998 modal data are summarized in Table 5.1. Note that the results based on frequency analysis (i.e., columns 2 and 4 of Table 5.1) and the results based on the mode shape analysis (i.e., columns 3 and 5) are in excellent

agreement.

Table 5.1 Summary of Stiffness Changes for 1997-1998

Component	Method			
	SID of Baseline Structure	SID & NDD	1997/1998 Frequencies	1997/1998 Mode Shapes
Deck Stiffness	8% increase	localized damage	9% increase	localized damage
Deck Mass	17% decrease	N/A	21% decrease	N/A
Column Stiffness	43% decrease	localized damage	53% decrease	localized damage
Abutments	38% decrease	N/A	42% decrease	N/A

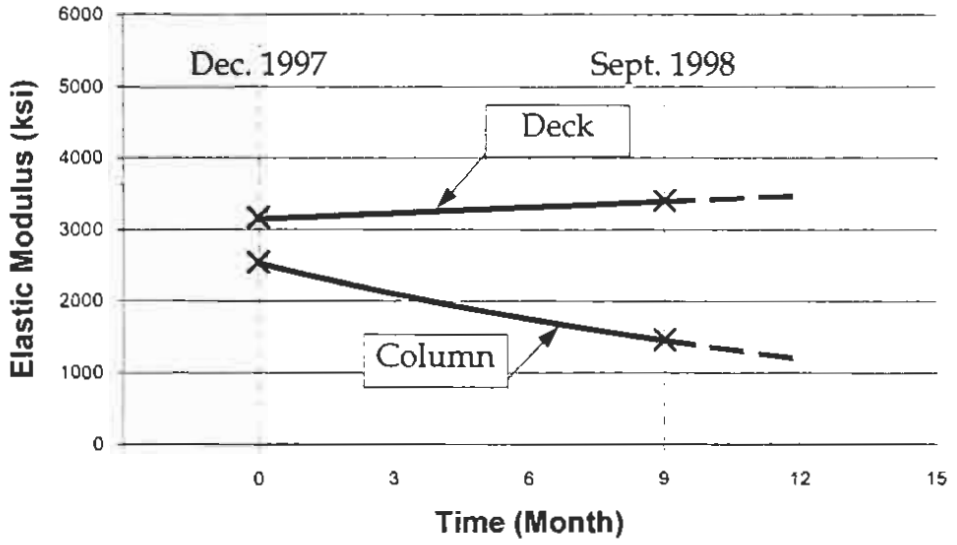

(a)

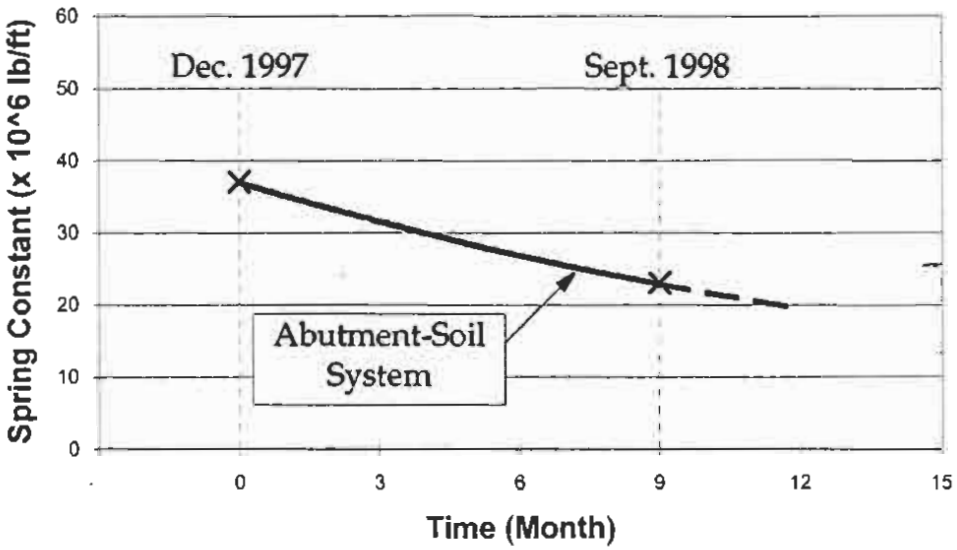

(b)

Figure 5.1 Changes in Average Stiffness Properties: (a) Elastic Modulus of the Deck and Column; (b) Spring Constant of Abutment-Soil System

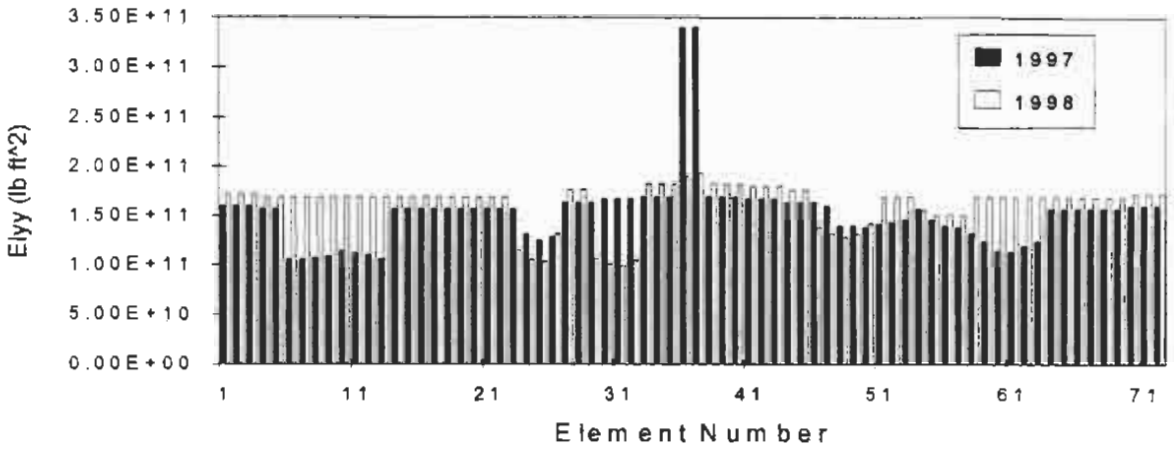

(a)

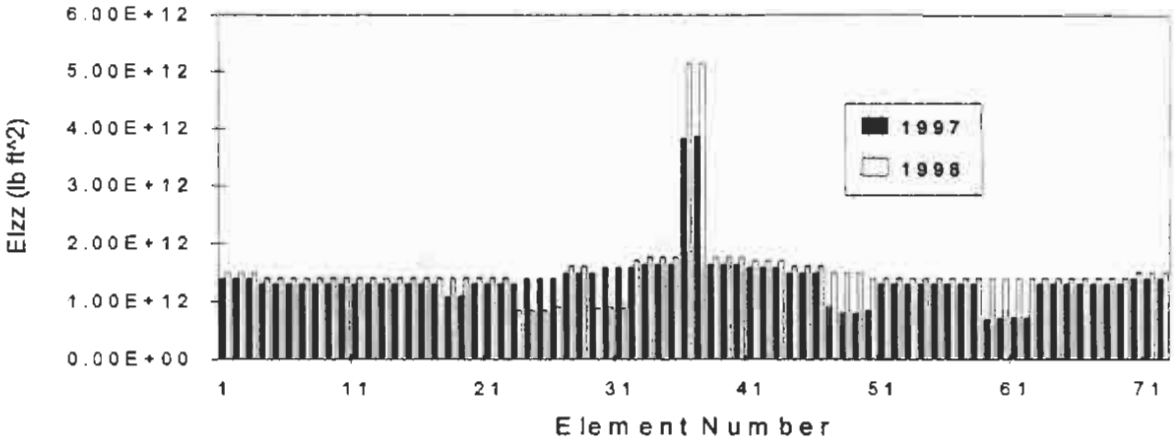

(b)

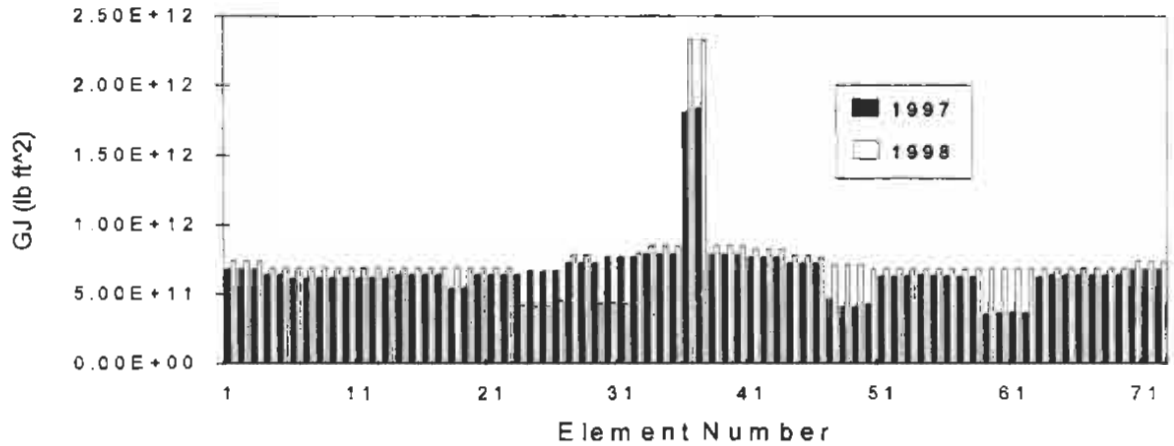

(c)

Figure 5.2 Stiffness Changes of the Deck: (a) EI_{yy}; (b) EI_{zz}; (c) GJ

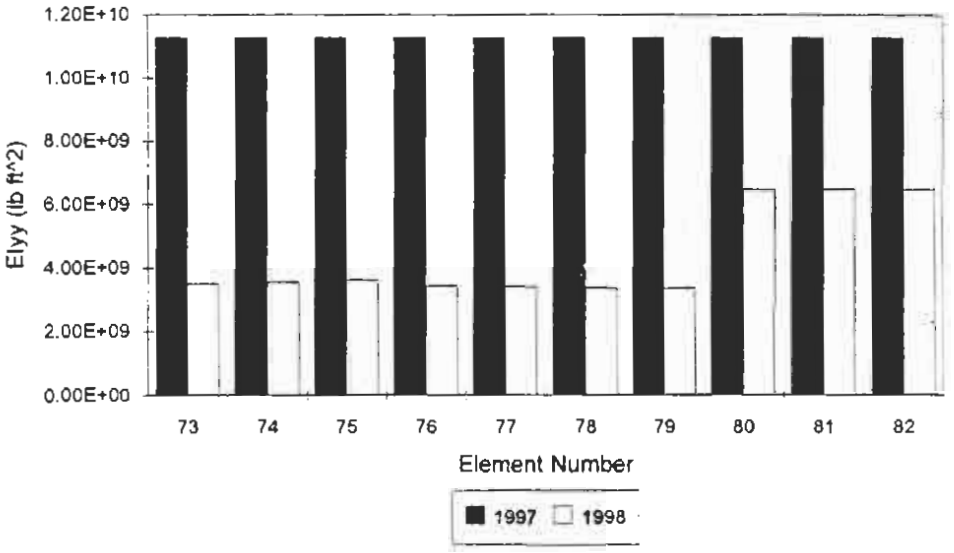

(a)

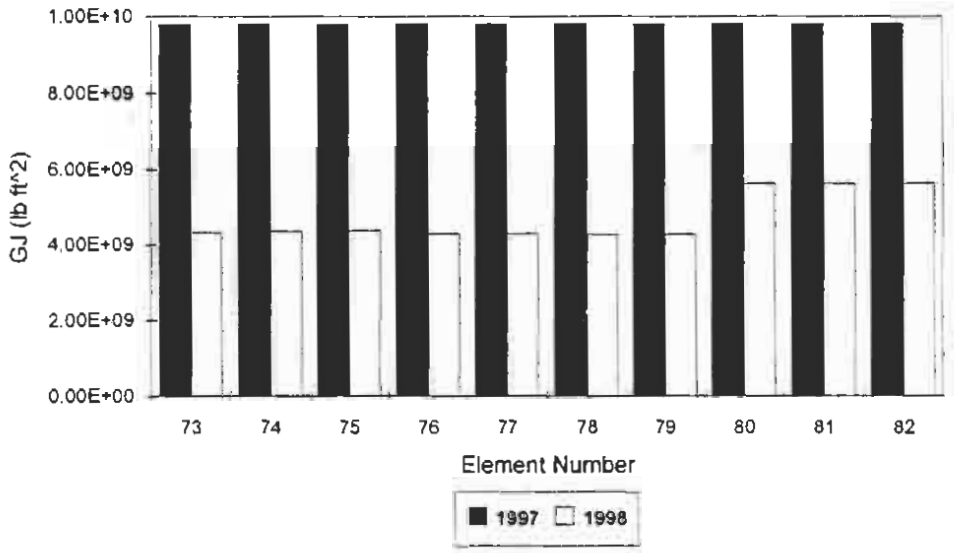

(b)

Figure 5.3 Stiffness Changes of the Column: (a) EI_{yy}; (b) GJ

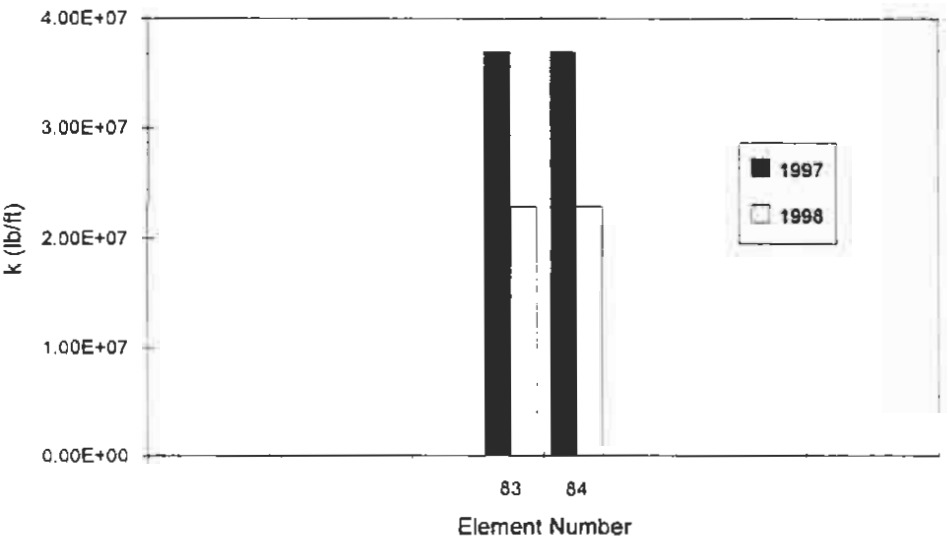

Figure 5.4 Stiffness Changes of the Abutments

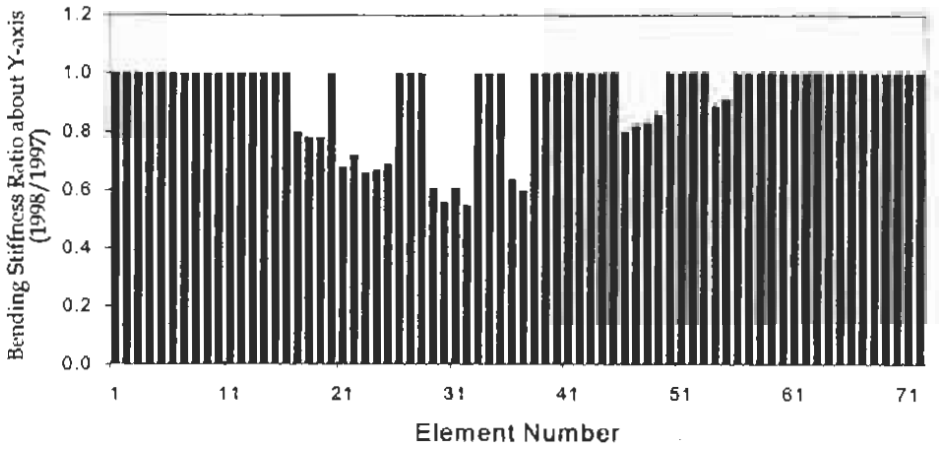

(a)

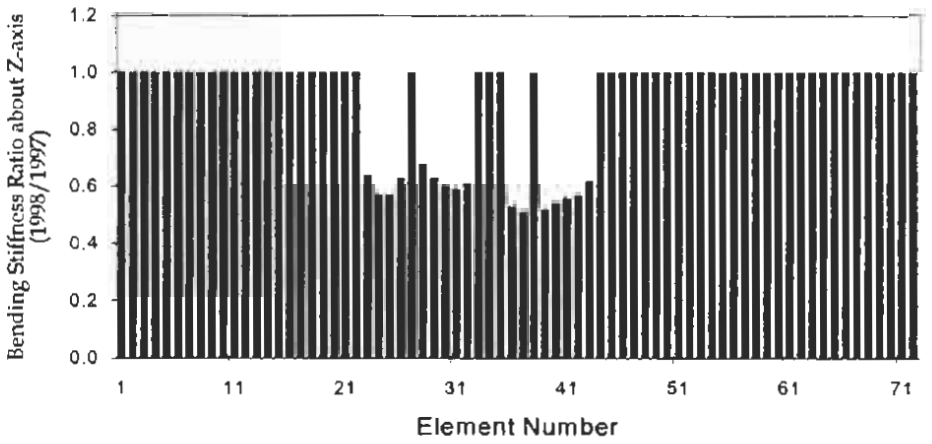

(b)

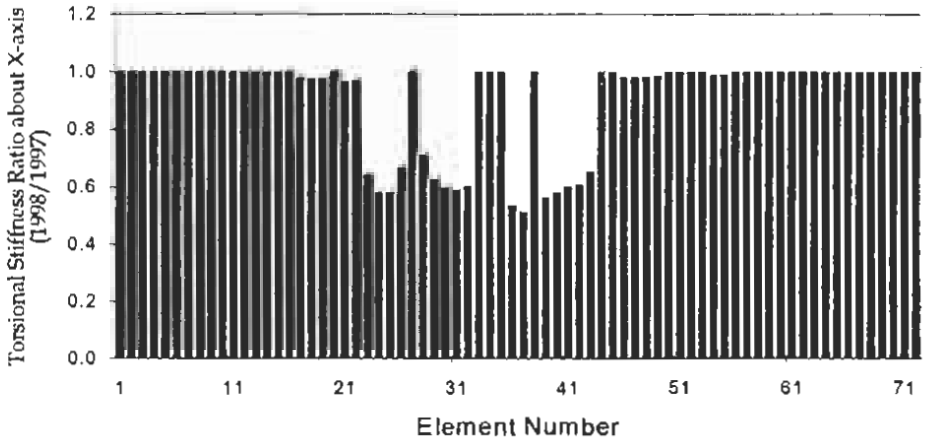

(c)

Figure 5.5 Estimated Stiffness Ratio of the Deck from the 1997 and 1998 Field-Measured Data: (a) $EI_{yy,\,1998}/EI_{yy,\,1997}$; (b) $EI_{zz,\,1998}/EI_{zz,\,1997}$; (c) GJ_{1998}/GJ_{1997}

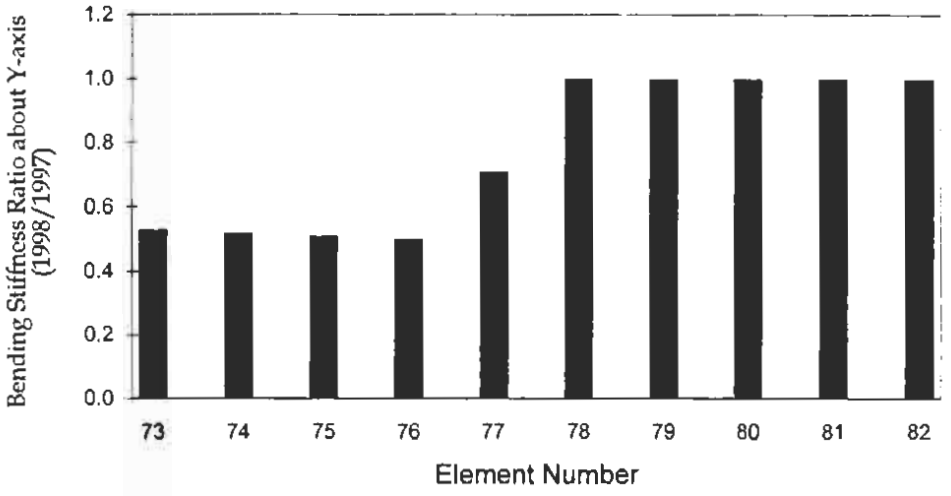

(a)

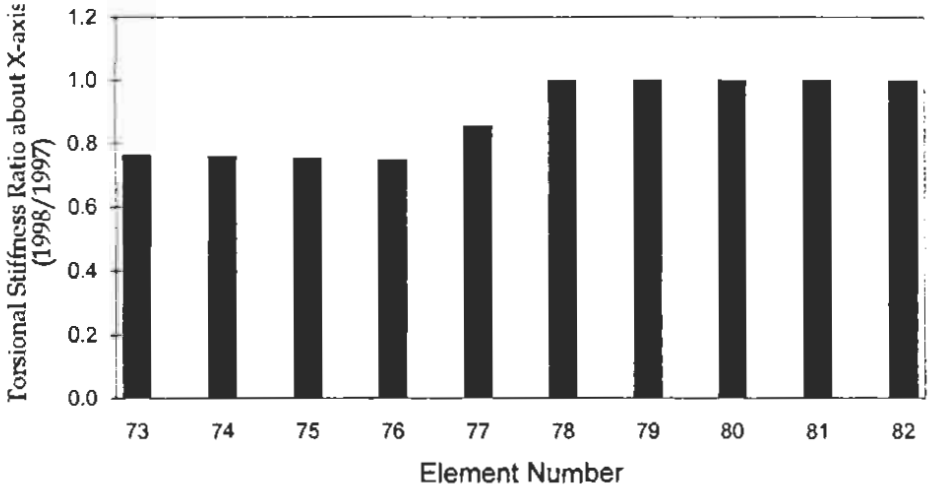

(b)

Figure 5.6 Estimated Stiffness Ratio of the Column from the 1997 and 1998 Field-Measured Data: (a) $EI_{yy,\,1998}/EI_{yy,\,1997}$; (b) GJ_{1998}/GJ_{1997}

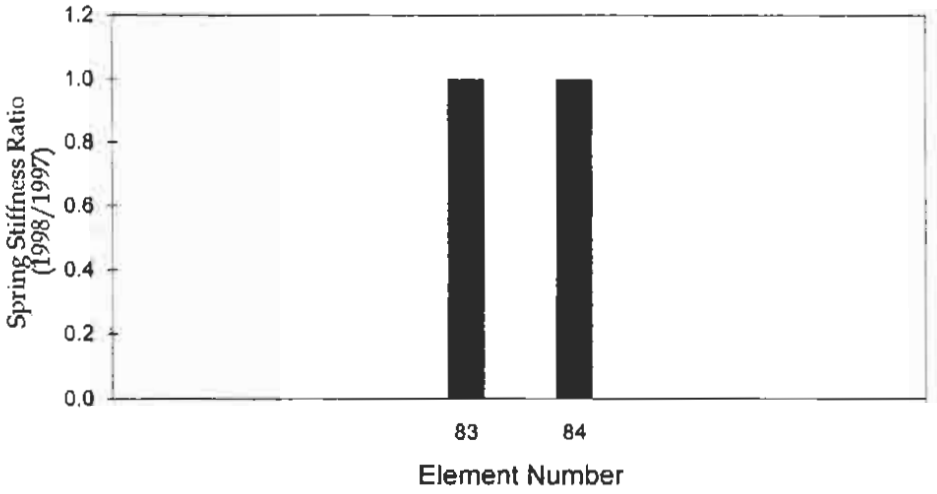

Figure 5.7 Estimated Stiffness Ratio (k_{1998}/k_{1997}) of the Abutments from the 1997 and 1998 Field-Measured Data

6. DISCUSSION OF RESULTS

6.1 Overview

The results in the last section may be summarized as follows:

1. Systems identification using frequency data indicates that from 1997 to 1998 the mass of the deck decreased;
2. Systems identification using frequency data also indicates that between 1997 and 1998 there was a significant reduction in the stiffness of the column and the abutments;
3. Systems identification using frequency data also shows that there was an apparent increase in the stiffness of the deck; and
4. Nondestructive damage detection using mode shape data indicates that localized damage exists in the deck and the column.

Below we will address some of the less obvious aspects of the above issues.

6.2 Apparent Decrease in Deck Mass

Weather conditions during the 1997 test in December were rainy and cold. Weather conditions during the 1998 test in September were dry and hot. During the wet season the mass of the deck can increase via at least two mechanisms: (1) moisture absorption by the concrete and (2) direct retention of water in the cavity of the box girder. With regards to the first mechanism, CALTRANS sources indicate that for 145 pounds per cubic foot concrete, it is estimated that the moisture content for bridges along the I-40 corridor is 1-2% during the dry months and can increase to 4-6% during the wet months. It has also been stated that some bridges in the Needles area, approximately 65 miles east along I-40, have been found to have absorption rates as high as 10%.

With regards to the second mechanism, we have no quantitative data. However, visual inspection of the deck has revealed a number of cracks on the

deck. It is quite possible that water may penetrate these cracks and lodge in the voids in the box girder.

6.3 Apparent Increase in Deck Modulus

While variations in mass are easy to imagine, possible explanations for the increase in modulus of the deck are not so obvious. However, before we continue with the discussion, it should be pointed out that the apparent increase in the modulus of the deck is much smaller than the changes calculated for the abutments and the column. There are at least two possible sources for this anomalous results: (1) limitations of the dynamic model of the structure, and (2) errors in the frequency data. With regards to the first limitation, the dynamic model used in this analysis was an undamped multi-degree-of-freedom system. Such factors as damping, thermal effects, and possible changes in boundary conditions were not considered. How these factors may alter the predictions is a subject of state-of-the-art research. Note that from an analysis of Tables B.10 and B.12 in Appendix B, there was no significant change in the modal damping ratio. Therefore, we can rule out the effect of damping. With regards to the second limitation, the instrumentation used to perform the modal analysis in 1997 differed from the instrumentation used in 1998. It is possible that slight differences in the calibration of the two systems may explain some of the increase in the stiffness. Differences in the resolution between the two data sets may also contribute to the difference of the moduli.

6.4 Local Damage in the Deck

Local damage in the structure is depicted in Figures 5.2 to 5.7. To provide some evidence of the veracity of the predictions a visual inspection was performed on the bridge on 22 May 1999. The objective was to determine if there might be a correlation between observed distress and predicted damage. During the visual

inspection, size and location of deck cracks were recorded.

The documented surface crack pattern is depicted in Figure 6.1. The pattern of surface cracks are mainly in the transverse direction, except for a group of cracks near the column-deck interface of Bent #2. The surface cracks consist of: (a) a single crack near Abutment #1; (b) two groups of cracks between Abutment #1 and Bent #2; (c) a group of cracks in the middle of the structure; (d) a group of cracks between Bent #2 and Abutment #3; and (e) a single crack near Abutment #3.

Figure 6.2 shows a combination of the documented crack locations and the potential damage locations identified using the 1997 field measurements. Note that the hatched areas in Figure 6.2 are superposed by damage locations identified using individual mode shapes. It is shown that a group of surface cracks between Bent #2 and Abutment #3, the cracks in the middle of the structure, and the individual cracks near Abutment #1 and Abutment #3 are identified by damage locations from the 1997 measurements. With regards to the two groups of surface cracks between Abutment #1 and Bent #2, only the south portion of cracks are detected.

Figure 6.3 compares the crack locations with the possible damage locations identified using the 1998 field measurements. These observations indicate that the damage locations appear to correlate with the observed cracks (except the single crack near Abutment #3). It is also observed that the north portion of two groups of cracks between Abutment #1 and Bent #2 is consistently detected in each mode. From this observation and on studying Figure 6.2 and Figure 6.3, one can deduce that the north portion of two groups of cracks between Abutment #1 and Bent #2 developed after the field measurement in December 1997 and before the field measurement in September 1998.

6.5 General Comments

In closing we make two observations that may put these results into perspective. First, from a statistical viewpoint, two data points are insufficient to draw a scientific conclusion. Future tests, similar to the ones described here, should be performed. It should also be pointed out that at present the testing and analysis for the Lavic Road Overcrossing is a routine activity. In fact, a modal test of the Lavic Road Overcrossing can now be accomplished in two to three hours.

The second observation is that a variation of 8% in the modulus of concrete still corresponds to what may be classified as good concrete. Table 6.1, adopted from ACI, classifies the quality of concrete in terms of the coefficient of variation of the compressive strength (ACI 214-65, 1968). Note that "good" concrete is characterized by a coefficient of variation between 10% and 15%. To translate this number into an equivalent coefficient of variation for the elastic modulus, we first begin with the well known empirical relationship between the modulus and the compressive strength:

$$E = a\sqrt{f_c} \tag{6.1}$$

The variance of E and f_c are related by

$$\text{Var } E = \left(\frac{\partial E}{\partial f_c}\right)^2 \text{Var } f_c \tag{6.2}$$

From the definition of coefficient of variation (COV), the two equations may be combined to give the relationship

$$COV_E = \frac{COV_{f_c}}{2} \tag{6.3}$$

Thus for good concrete, the coefficient of variation of the modulus is expected to range between 5% and 8%.

Table 6.1 Coefficients of Variation for Different Control Standards

Class of operation	Standards of concrete control			
	Excellent	Good	Fair	Poor
General construction, over-all variations	< 10%	10% - 15%	15% - 20%	> 20%

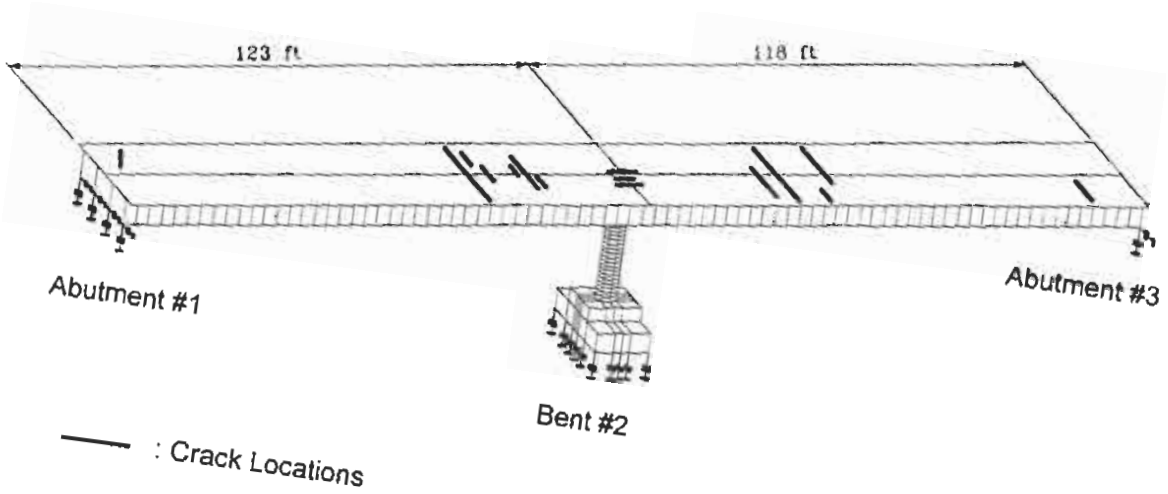

Figure 6.1 Surface Crack Pattern on the Deck

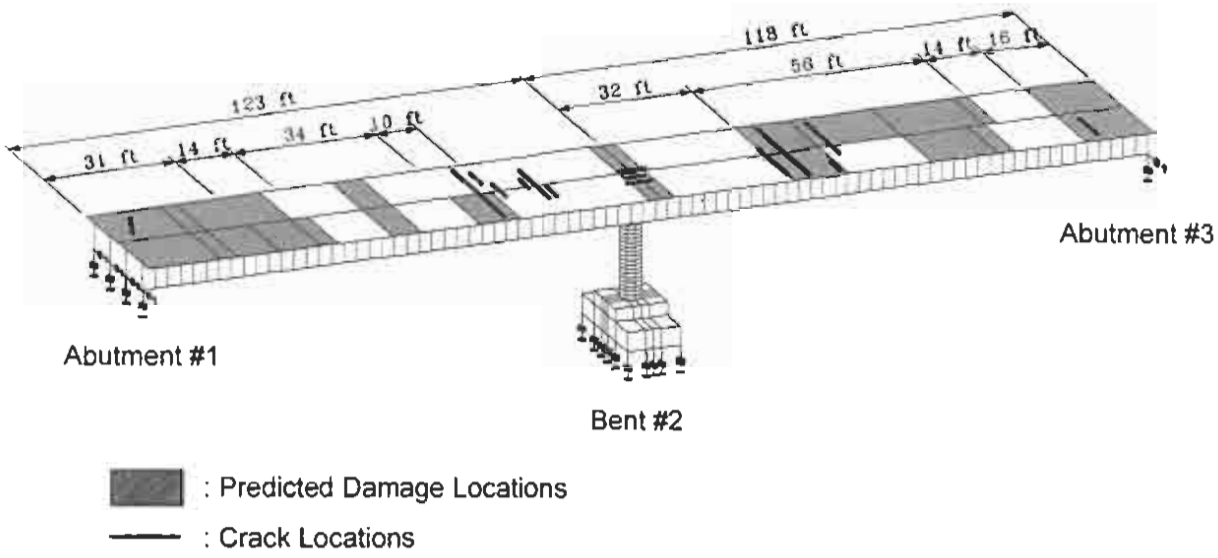

Figure 6.2 Comparison of Surface Cracks with Damage Localization Results using Superposition of All Modes from the 1997 Measurements

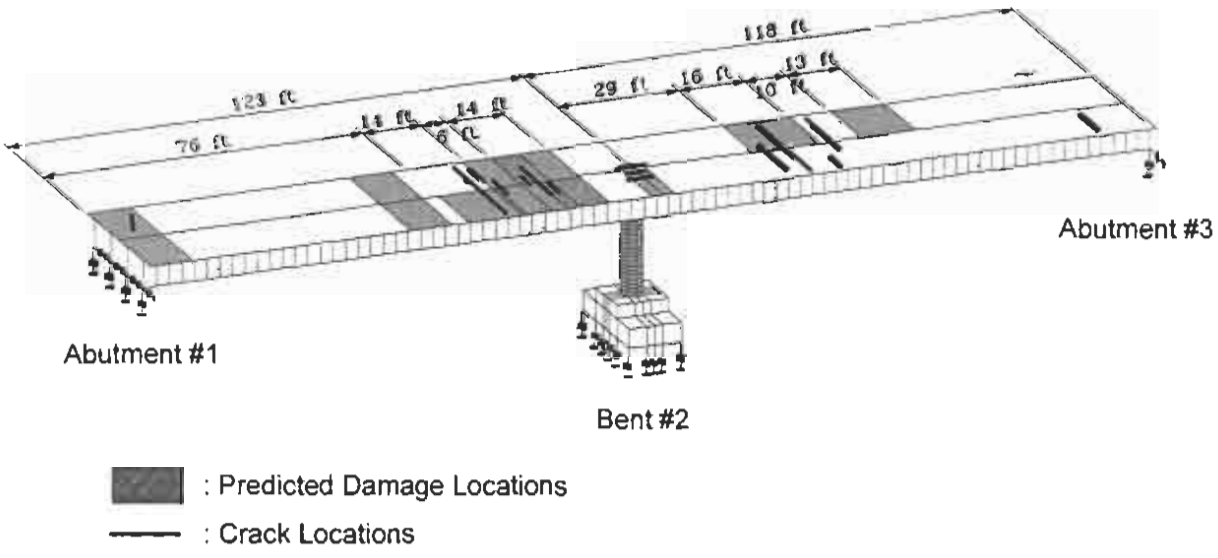

Figure 6.3 Comparison of Surface Cracks with Damage Localization Results using Superposition of All Modes from the 1998 Measurements

7. SUMMARY AND CONCLUSIONS

7.1 Summary

The objective of this study was to quantitatively evaluate, using recent work in nondestructive damage evaluation (NDE) and systems identification at Caltrans, the rate of possible structural stiffness deterioration of the Lavic Road Overcrossing (Bridge #54-734). The structure is suspected of having been constructed with reactive aggregates. To meet this objective, the following eight tasks were performed. First, a modal test was performed on the bridge in December 1997. Second, a modal analysis was performed on the test data and selected modal parameters of the bridge were extracted. Third, a 3-dimensional finite element model of the superstructure and substructure of the bridge was developed. Fourth, using the finite element model and the frequency modal parameters extracted from the field data, baseline modal parameters for the bridge and mass and elastic parameters of the deck, column, and abutments were generated. Fifth, using the field modal parameters and the baseline modal parameters, potential damage in the structure at the member level was localized. Sixth, using the field modal parameters and a knowledge of the location of damage, a damage severity was assigned to each of the identified members. Seventh, using the location and severity of the damage along with the baseline model, the detailed structural properties of the existing bridge were estimated. Finally, each of the previous seven tasks were repeated nine months later (September 1998) and the magnitude of deterioration during that period of time for the structural members was quantified.

7.2 Conclusions

The quantification of the change in material properties during the stated period have led to the following conclusions:

1. Systems identification using frequency data indicates that from 1997 to 1998 the mass of the deck decreased 17% - 21%. This decrease was explained by the fact that during the December, 1997 test, weather conditions were wet and cold while during the September, 1998 test, the conditions were hot and dry. Some of the difference in mass may also be explained by the direct retention of leaking water in the hollow chambers of the box girder deck during the wet months;
2. Systems identification using frequency data indicates that between 1997 and 1998 there was a significant reduction in the stiffness of the column (43% - 53%) and the abutments (38% - 42%);
3. Systems identification using frequency data also shows that there was an apparent increase (8% - 9%) in the stiffness of the deck. While this apparent increase of the modulus of the deck may be due in part to such causes as the limitations of the dynamic model of the structure or errors in the data, variations of these magnitudes in the coefficient of variation of the elastic modulus of concrete are consistent with good quality concrete; and
4. Nondestructive damage detection using mode shape data indicates that localized damage exists in the deck and the column. A correlation exists between the visually observed cracking pattern on the deck and the predicted locations of damage.

REFERENCES

ABAQUS (1994). *Version 5.4 User Manual.* Hibbitt, Karlsson & Sorensen, Inc., Providence, Rhode Island.

ACI 214-65, *Recommended Practice for Evaluation of Concrete Test Results of Field Concrete.* In ACI Manual of Concrete Practice, Vol. 1, American Concrete Institute, Detroit, Michigan, 1968.

Craig, R.R. (1981). *Structural Dynamics - An Introduction to Computer Methods.* John Wiley & Sons, New York, New York.

Garcia, G.V. (1996). "Evaluation of Relative Performance of Classification Algorithms for Nondestructive Damage Detection." *Ph.D. Dissertation,* Texas A&M University, College Station, Texas.

Gibson, J.D., and Melsa, J.L. (1975). *Introduction to Nonparametric Detection with Applications.* Academic Press, New York, New York.

Kolsky, H. (1963). *Stress Waves in Solids.* Dover Publications, New York, New York.

Lin, J., and Sansalone, M. (1997). "A Procedure for Determining P-Wave Speed in Concrete for Use in Impact-Echo Testing Using a Rayleigh Wave Speed Measurement Technique." *SP-168, Innovations in Non-Destructive Testing of Concrete, American Concrete Institute,* Farmington Hills, MI.

Nadler, M., and Smith, E.P. (1993). *Pattern Recognition Engineering.* John Wiley, New York, New York.

Sansalone, M., and Carino, N. (1986). "Impact-Echo: A Method for Flaw Detection in Concrete Using Transient Stress Waves." *NBSIR 86-3452, National Bureau of Standards,* Gaithersburg, MD, Sept.

Stubss, N., and Osegueda, R. (1990). "Global Non-Destructive Damage Evaluation in Solids." *Int. J. Analytical and Experimental Modal Analysis,* 5(2), 67-79.

Stubbs, N., Kim, J.T., and Topole, K. (1992). "An Efficient and Robust Algorithm for Damage Localization in Offshore Platforms." *ASCE 10th Structures Congress '92,* San Antonio, Texas, 543-546.

Stubbs, N., and Kim, J.T. (1996). "Damage Localization in Structures without Baseline Modal Parameters.", *AIAA J.,* 34(8), 1644-1649.

APPENDIX A

A METHODOLOGY TO IDENTIFY STRUCTURAL PROPERTIES OF THE BASELINE AND THE EXISTING STRUCTURES

A.1 System Identification Scheme for the Baseline Structure

The rationale behind the development of the baseline model can be explained with the aid of Figure A.1. Suppose a flawed (i.e., damaged) structure [Figure A.1(a)] is given with field-measured mode shapes Φ_i^* and eigenfrequencies ω_i^*. Assume that the magnitude of the flaw is small in comparison to a flawless (i.e., baseline) structure. Suppose that an estimate of the flawless structure can be identified, shown in Figure A.1(b), using only the frequency information from the flawed structure. Then the identified baseline model [Figure A.1(b)] will have the same eigenfrequencies ω_i^* (in the least square sense) of the flawed model [Figure A.1(a)] but the mode shapes of the two structures will be different in the neighborhood of the flaw. This difference in the mode shapes of the identified baseline structure and the measured mode shapes of the existing structure may then be exploited to localize the flaw.

Here, a system identification methodology to identify baseline modal responses of a structure is outlined (Stubbs and Kim 1996). Consider a linear skeletal structure with *NE* members and *N* nodes. Suppose $\mathbf{k}_j^*$ is the unknown stiffness of the j^{th} member of the structure for which *M* eigenvalues are known. Also, suppose $\mathbf{k}_j$ is a known stiffness of the j^{th} member of a finite element (FE) model for which the corresponding set of *M* eigenvalues are known. Then, relative to the FE model, the fractional stiffness change of the j^{th} member of the structure, α_j, and the stiffnesses are related according to the following equation:

$$\mathbf{k}_j^* = \mathbf{k}_j (1 + \alpha_j) \tag{A.1}$$

Similarly the fractional mass change of the j^{th} member of the structure, β_j, and the masses are related according to the following equation:

$$\mathbf{m}_j^* = \mathbf{m}_j (1 + \beta_j) \tag{A.2}$$

The fractional stiffness change and the fractional mass change of *NE* members may be

obtained using the following equation (Stubbs and Osegueda 1990):

$$\mathbf{Z} = \mathbf{F}\alpha - \mathbf{G}\beta \tag{A.3}$$

where α is a NE x 1 matrix containing the fractional changes in stiffness between the FE model and the structure, β is a NE x 1 matrix containing the fractional changes in mass between the FE model and the structure, $\mathbf{Z}$ is a M x 1 matrix containing the fractional changes in eigenvalues between the two systems, $\mathbf{F}$ is a M x NE stiffness sensitivity matrix relating the fractional changes in stiffnesses to the fractional changes in eigenvalues, and $\mathbf{G}$ is a M x NE mass sensitivity matrix relating the fractional changes in masses to the fractional changes in eigenvalues.

The M x NE, $\mathbf{F}$ matrix can be determined as follows: first, M eigenvalues are numerically generated from the initial FE model; second, the stiffness of the first member of the FE model is modified by a known amount; third, the corresponding set of M eigenvalues are numerically generated for the modified FE model; fourth, the fractional changes between the M initial eigenvalues and M eigenvalues of the modified structure are computed; fifth, each component of the first column of the $\mathbf{F}$ matrix (i.e., the M x 1, $\mathbf{F}$ matrix) is computed by dividing the fractional changes in each eigenvalue by the magnitude of the modification at member one; and finally, the M x NE, $\mathbf{F}$ matrix is generated by repeating the entire procedures for all NE members. The M x NE, $\mathbf{G}$ matrix can be determined in similar manner.

Using the above rationale as a basis, the following 7-step algorithm is proposed to identify a given structure:

1. Select a target structure (e.g., a post-damage state of the structure) for which sufficient eigenfrequencies that can be used to identify the baseline structure are available. (Note that the mode shapes of the damaged structure in defining the target structure are ignored.)
2. Select an initial FE model of the structure, utilizing all possible knowledge about the design and construction of the structure.
3. As outlined above, compute the sensitivity matrices of the FE model.
4. As outlined above, compute the fractional changes in eigenvalues between the FE

model and the target structure.

5. Assume $\alpha = 0$ and fine-tune the FE model by first solving Equation (A.3) to estimate mass changes (i.e., to compute the *NE* x 1, β matrix) and next solving Equation (A.2) to update the mass parameters of the FE model.
6. Assume $\beta = 0$ and fine-tune the FE model by first solving Equation (A.3) to estimate stiffness changes (i.e., to compute the *NE* x 1, α matrix) and next solving Equation (A.1) to update the stiffness parameters of the FE model.
7. Repeat steps 4~6 until $\mathbf{Z} \cong 0$ or $\alpha \cong 0$ and $\beta \cong 0$ (i.e., as they approach zero) when the parameters of the FE model are identified.

The converged FE model is the baseline model. It has the frequencies of the damaged (i.e., target) structure but none of its members are damaged. Furthermore, the mode shapes of the baseline model differ from those of the damaged structure. Once the baseline model is identified, its modal parameters can be numerically generated [e.g., using commercial software ABAQUS (1994)].

A.2 Damage Localization Theory (Damage Index Method)

In the field of Nondestructive Damage Detection (NDD) using modal parameters, one of the more difficult problems is that of making a statement regarding the integrity of a relatively small portion of a structure when very few modal parameters are available. In such cases, inverse methods using systems of equations usually result in unsolvable systems with few equations but many unknowns. The discipline of pattern recognition provides a way to deal with such heavily underdetermined systems (Nadler and Smith 1993).

In pattern recognition, physical world data are transduced into the so-called pattern space. Using techniques of dimensionality reduction, the pattern space is reduced to a smaller dimension known as the feature space. Data in the feature space are introduced to a decision algorithm and the elements of the feature space are classified into a finite number of clusters. In the problem at hand, the dynamic response of the structure in the time domain represents the physical world data and the modal parameters represent the pattern

space. The feature space is represented by indicators that are a function of measurable pre-damage and post-damage modal parameters. These indicators can be selected in such a manner that they reflect internal structure in the data. The decision algorithm is a means by which the data space is partitioned into D_n clusters (decision spaces). In this study, n = 2 and the decision spaces correspond to the cases: (a) a structure is not damaged at a given location, and (b) a structure is damaged at a given location. For each instance the indicator of damage will fall into one of the two categories.

The damage index method utilizes the change in mode shapes of the pre-damage and post-damage structure to detect and locate damage in a structure (Stubbs et al. 1992). Consider a linear, undamaged, skeletal structure with NE elements and N nodes. After writing the equations of motion for the structure and solving the eigenvalue problem, the i^{th} modal stiffness, K_i, of the arbitrary structure is given by (Craig 1981)

$$K_i = \Phi_i^T C \Phi_i \tag{A.4}$$

where Φ_i is the i^{th} modal vector and C is the system stiffness matrix. From matrix structural analysis, the contribution of the j^{th} member to the i^{th} modal stiffness, K_{ij}, is given by

$$K_{ij} = \Phi_i^T C_j \Phi_i \tag{A.5}$$

where C_j is the contribution of the j^{th} member to the system stiffness matrix. The fraction of modal energy for the i^{th} mode that is concentrated in the j^{th} member (i.e., the element sensitivity of the j^{th} member to the i^{th} mode) is given by

$$F_{ij} = K_{ij}/K_i \tag{A.6}$$

Let the corresponding modal parameters in Equations (A.4) to (A.6) associated with a subsequently damaged structure be characterized by asterisks. Then for the damaged structure,

$$F_{ij}^* = K_{ij}^* / K_i^* \tag{A.7}$$

where K_{ij}^* and K_i^* are given by, respectively

$$K_{ij}^* = \Phi_i^{*T} C_j^* \Phi_i^* \tag{A.8}$$

and

$$K_i^* = \Phi_i^{*T} C^* \Phi_i^* \tag{A.9}$$

Again, from matrix structural analysis, the stiffness matrices C_j and C_j^* in Equations (A.5) and (A.8) may be written as follows:

$$C_j = k_j C_{jo} \tag{A.10}$$

and

$$C_j^* = k_j^* C_{jo} \tag{A.11}$$

where the scalars k_j and k_j^*, respectively, are parameters representing the material stiffness properties of the undamaged and damaged j^{th} member of the structure, and the matrix C_{jo} involves only geometric quantities (and possibly terms containing Poisson's ratio). The quantities F_{ij} and F_{ij}^* are related by the equation:

$$F_{ij}^* = F_{ij} + dF_{ij} \tag{A.12}$$

where dF_{ij} is related to the change in the fraction of modal energy of the j^{th} member in the i^{th} mode. The quantity dF_{ij} can be obtained from the expression:

$$dF_{ij} = \frac{K_{ij}}{K_i}\left[\frac{dK_{ij}}{K_{ij}} - \frac{dK_i}{K_i}\right] \tag{A.13}$$

Assuming that the structure is damaged at a single location j and the resulting change in F_{ij} is only a function of k_j, a first order approximation of dK_{ij} can be obtained from the expression:

$$dK_{ij} \cong \frac{\partial K_{ij}}{\partial k_j} dk_j + \frac{\partial K_{ij}}{\partial u_{ij}} \frac{\partial u_{ij}}{\partial k_j} dk_j \tag{A.14}$$

where

$$u_{ij} = \Phi_i^T C_{jo} \Phi_i \tag{A.15}$$

Using Equations (A.5) and (A.10), it can be shown that

$$\frac{\partial K_{ij}}{\partial k_j} = u_{ij} \tag{A.16}$$

and

$$\frac{\partial K_{ij}}{\partial u_{ij}} = k_j \tag{A.17}$$

Next, introducing the modal force vector associated with the j^{th} member and the i^{th} mode, A_{ij}, given by

$$A_{ij} = C_j \Phi_i \tag{A.18}$$

it can be shown that by using Equations (A.10), (A.15), and (A.18),

$$u_{ij} = \frac{1}{k_j^2} A_{ij}^T C_{jo}^{-1} A_{ij} \tag{A.19}$$

Therefore, if it is assumed that the modal force A_{ij} remains constant while k_j changes (note that the assumption is true in the case of a statically determinant system), then

$$\frac{\partial u_{ij}}{\partial k_j} = -\frac{2u_{ij}}{k_j} \tag{A.20}$$

Since it has been assumed that the structure is damaged in only one location, it follows readily that $dK_{ij} = dK_i$. Also, since $K_i >> K_{ij}$, from Equation (A.13)

$$dF_{ij} \cong \frac{dK_{ij}}{K_i} = -\frac{u_{ij}}{K_i} dk_j = -F_{ij}\alpha_j \tag{A.21}$$

where $a_j = dk_j/k_j$, the fractional change in the stiffness of Element j. Substituting the result of Equation (A.21) into Equation (A.12), and substituting for F_{ij}^* using Equations (A.7) to (A.12), it can be shown that

$$\frac{k_j^*}{K_i^*} = k_j \frac{u_{ij}}{K_i}(1 - \alpha_j) \tag{A.22}$$

Substituting for $a_j = (k_j^* - k_j)/k_j$ in Equation (A.22), and rearranging, one obtains:

$$\frac{k_j}{k_j^*} = \left(\frac{u_{ij}^*}{K_i^*} + \frac{u_{ij}}{K_i}\right) / 2\frac{u_{ij}}{K_i} \tag{A.23}$$

Setting $f_{ij}^* = u_{ij}^*/K_i^*$ and $f_{ij} = u_{ij}/K_i$, Equation (A.23) reduces to

$$DI_{ij} = \frac{k_j}{k_j^*} = \frac{f_{ij}^*/f_{ij} + 1}{2} \tag{A.24}$$

where DI_{ij} is the indicator of damage in the j^{th} member using the i^{th} mode. If $DI_{ij} > 1$, damage may exist. From Equation (A.24), the fundamental indicator of damage is the quotient f_{ij}^*/f_{ij}. Note that the one in the numerator is, essentially, a shifting factor while the two in the denominator is a scaling factor. Equation (A.24) becomes singular when $f_{ij} \rightarrow 0$: a condition which will occur when, simultaneously, the element size approaches zero and the element is located at a node of a mode. Here the division-by-zero difficulty can be overcome by simply

shifting the axis of reference for the sensitivities. For example, if the origin is shifted from $f_{ij} = 0$ to $f_{ij} = -1$, then

$$f_{ij}' \rightarrow 1 + f_{ij} \tag{A.25}$$

and

$$f_{ij}^{*\prime} \rightarrow 1 + f_{ij}^{*} \tag{A.26}$$

So the new indicator function, DI_{ij}, which will also form the basis of feature space (in the pattern recognition sense), becomes

$$DI_{ij} = \frac{f_{ij}^{*} + 1}{f_{ij} + 1} \approx \left[\frac{\Phi_i^{*T} C_{jo} \Phi_i^{*} + \Phi_i^{*T} C \Phi_i^{*}}{\Phi_i^{T} C_{jo} \Phi_i + \Phi_i^{T} C \Phi_i} \right] \frac{\Phi_i^{T} C \Phi_i}{\Phi_i^{*T} C \Phi_i^{*}} \tag{A.27}$$

There are two important characteristics of the indicator DI_{ij} given by Equation (A.27): first, the expression attempts to express the changes in stiffness at a specific location in terms of measurable pre-damage and post-damage mode shapes (Φ_i and Φ_i^{*}); and second, the term C_{jo} on the right hand side of Equation (A.27) can be determined from a knowledge of the geometry of the structure. Thus for each damage location j, there are as many DI_{ij}'s available as there are mode shapes. As noted above, in the context of pattern recognition, the latter values of DI_{ij} define the feature space. The following expression will be the convenient form of damage index DI_j for a single location if several modes (NM) are used

$$DI_j = \frac{\sum_{i=1}^{NM} \left(\Phi_i^{*T} C_{jo} \Phi_i^{*} + \Phi_i^{*T} C \Phi_i^{*} \right) \Phi_i^{T} C \Phi_i}{\sum_{i=1}^{NM} \left(\Phi_i^{T} C_{jo} \Phi_i + \Phi_i^{T} C \Phi_i \right) \Phi_i^{*T} C \Phi_i^{*}} \tag{A.28}$$

The final step in damage localization is classification. Classification analysis addresses itself to the problem of assigning an object to one of a number of possible groups on the basis of observations made on the objects. In this study, the objects are the members of the structure. There are two groups: undamaged elements and damaged elements. Finally, the observations made on the objects are the DI_j's. Many techniques are available to accomplish the end. Examples of these methods include classification on the basis of: (1) Bayes' rule (from which the well known Linear Discriminant Analysis and Quadratic Discriminant Analysis are derived), (2) nearest distance, and (3) hypothesis testing (Gibson

and Melsa 1975). While other approaches are available (Garcia 1996), the authors currently have utilized primarily techniques from hypothesis testing. The criteria for damage localization is established based on statistical reasoning. The values, DI_1, DI_2, DI_3, ... , DI_{NE} for each element, are considered as realization of a random variable. The normalized damage indicator is given by

$$z_j = \frac{DI_j - \mu_{DI}}{\sigma_{DI}} \tag{A.29}$$

where μ_{DI} and σ_{DI} represent mean and standard deviation of the damage index, DI_j, respectively. Let H_o be the hypothesis that the structure is not damaged at member j, and let H_1 be the hypothesis that the structure is damaged at member j. The following decision rules may be used to assign damage to member j: (1) choose H_1 if $z_j \geq \lambda$ and (2) choose H_o if $z_j < \lambda$ where λ is a threshold which assigns a level of significance.

A.3 Damage Severity Estimation

Note that in Equation (A.24) the indicator of damage is the ratio of the undamaged stiffness to the damaged stiffness. Such a number exists for each potentially damaged member. For example, in the case of a truss there is a DI_j associated with every member j. Here the damage is expressed as the fractional change in stiffness of an element:

$$\alpha_j = \frac{k_j^* - k_j}{k_j} = \frac{1}{DI_j} - 1 \tag{A.30}$$

Thus if there is no damage, $\alpha_j = 0$; if there is damage, $\alpha_j < 0$. Note that if $\alpha_j = -1$, all stiffness capacity is completely lost.

A.4 Identification of Stiffness of Existing Structure

Having stiffness parameters for the baseline structure, location of damage, and the severity of damage, the stiffness properties of the existing structure can be obtained from the equation:

$$k_j^{(existing)} = k_j^{(baseline)}\left[1 + \alpha_j\right] \tag{A.31}$$

Note that if there is no damage at location j, the stiffness properties of the baseline and the existing structures are the same.

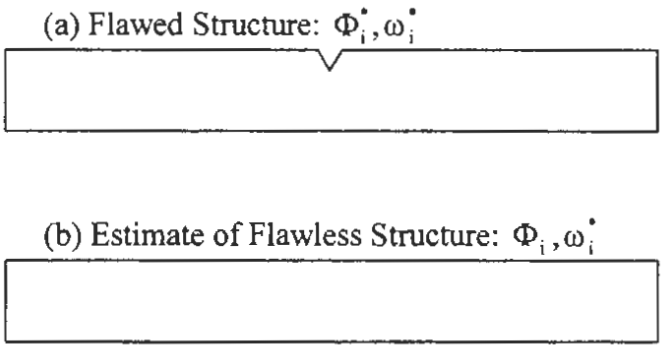

Figure A.1 Flawed Structure and Estimate of Flawless Structure

APPENDIX B

FIELD DATA MEASUREMENT AND ANALYSIS

B.1 Introduction

This appendix documents the field investigation of the Lavic Road Overcrossing completed for the California Department of Transportation (Caltrans) under Contract 59A0022 by the Texas Engineering Experiment Station. The goal of this contract is to develop formal techniques to predict the structural integrity and the remaining service life of existing concrete structures weakened by reactive aggregate used during construction of the bridge.

Experimental field data were collected from the Lavic Road Overcrossing located on Interstate 40, 7.4 miles west of Ludlow, San Bernardino County, California during the period of December 20, 1997 to December 22, 1997 and nine months later during the period of September 27, 1998 to September 29, 1998. The field data collected during these periods included photographic records documenting the overcrossing site, experimental setups, visible abutment/superstructure damage, modal data derived from the excitation of the structure, and wave propagation data at selected points on the superstructure and abutments. The intent of this appendix is to document the field data collection methodology and to present analytical results from the processed data. Frequency and mode shapes for the lower structural modes where extracted from the data collected on site. Selected modal data were used in subsequent systems identification and damage detection analyses.

Field data collection and measurement techniques used in these field tests were designed to provided high resolution spatial modal data while minimizing the impact of the measurement process on usability of the structures. The investigated structure was an in-service bridge which remained open to traffic during tests. Obstruction of traffic was limited to shoulder closures. The global damage detection algorithm applied to these structures required that three to five low-frequency global modes be measured with sufficient resolution to accurately extract irregularities in mode shape curvatures.

A typical data set consisted of thirty or more structural responses at selected node points throughout the structure. Data were collected with several instrumentation setups utilizing five

to seven accelerometers per setup. A common impact point was used to excite the structure for all setups. Several overlaps of common response points were included in the setups to provide linkages between individual setups. Variations in response of these common points have not been noted in collected response data. A large aggregate data set derived from the individual instrument setups was used to perform a structural modal analysis. Individual mode shapes and the corresponding frequency parameters were extracted.

B.2 Site Description

The Lavic Road Overcrossing is a standard Caltrans-designed reinforced concrete box-girder, constructed in 1968 over Interstate 40. The overcrossing has a south span of 123 ft. and north span of 118 ft. The spans rigidly connect to a single pedestal 60-inch diameter column located in the freeway median. The box-girder is approximately 26 ft. wide and 7 ft. deep and has two symmetrical interior longitudinal ribs. Wall and deck thickness is approximately 6 inches. The structure is oriented nearly North-South. Figures B.1 through B.4 show views of the structure from several vantage points on the surrounding terrain. Figure B.5 is a photograph of the one of the expansion joints at the superstructure-abutment interface showing evidence of recent grouting operations. Figures B.6 and B.7 are photographs of the abutment-wingwall details below the superstructure which exhibit significant visible deterioration.

B.3 Field Instrumentation

The lightweight mobile field equipment allowed quick movement through sequential instrument setups. The goal during field tests was to acquire all modal response data in a two day period. It typically took fifteen minutes to move accelerometers and reset instrumentation for each setup and ten minutes to acquire data. Several instrument configurations were utilized. In the initial test baseline field measurements were acquired with an 8-channel instrument setup consisting of seven single-axis accelerometers and an impact hammer. The second field test utilized the same impact hammer and five triaxial accelerometers. Time data acquired in these tests were processed on a 16-channel digital signal analyzer.

B.3.1 Field Instrument Setup for December 1997 Test Period

Modal data were collected using an eight-channel instrumentation setup consisting of seven accelerometers and one load cell from a drop weight impact hammer. Data from thirty superstructure response points were collected in seven separate setups using a common hammer impact point on the east side of the superstructure between accelerometer locations 23 and 24 (see Figure B.20). Several overlaps of common response points were included in the setups to provide linkages between data sets. Variations in structural response between setups were not noted in the response data. Figure B.8 shows a schematic of the basic instrumentation setup used in this field investigation.

PCB 393A03 ICP accelerometers were used for all acceleration measurements. Figure B.9 and Figure B.10 show typical accelerometer installations on the superstructure deck and center column. Aluminum angle brackets were used to attach accelerometers in horizontal orientations for transverse measurements. Specifications for this accelerometer are summarized in Table B.1. The drop weight impact hammer specifically constructed for this field investigation is shown in Figure B.11. The hammer tip was instrumented with a 20,000 lb PCB 200C20 piezoelectric load cell. Lead ballast was used to increase impact head weight to 120 lb Table B.2 summarizes the specifications of this instrument.

Data from the accelerometers and impact hammer were acquired and processed on an eight-channel Zonic Model 2300 signal analyzer. Selected time data and frequency measurements were transferred to a laptop computer for further analysis. The computer also controlled the data acquisition and setup of the Zonic analyzer. A typical field modal setup is shown in Figure B.12. Table B.3 lists selected specification data for the Zonic 2300. Batteries provided DC power to the instrumentation system during testing.

B.3.2 Field Instrument Setup for September 1998 Test Period

The December 1997 modal test was replicated using a sixteen-channel instrumentation setup consisting of five triaxial accelerometers and the same drop weight impact hammer used in earlier testing. Data were collected from the same thirty superstructure response points using the hammer impact location defined in December 1997. Data were collected in eight separate setups. Several overlaps of common response points were included in the setups to provide

linkages between setups. The major difference between the two test periods was use of triaxial accelerometers and a different signal analyzer.

Kistler 8390A2 triaxial accelerometers were used for all acceleration measurements. These sensors were attached directly to response points in orientations matching global Cartesian response directions. Specifications for the accelerometer are summarized in Table B.4. Data from the accelerometers and impact hammer were acquired and processed on with a 16-channel SigLab 20-42 DSP analyzer manufactured by DSP Technologies. Time data were transferred to a laptop computer for further analysis. Table B.5 presents selected specification data for the SigLab 20-42. Figure B.13 and B.14 depict typical instrument setups for this testing.

B.4 Discussion of Instrument Response Characteristics

Typical vertical accelerometer time responses from the bridge deck are shown in Figures B.15 and B.16. These traces represent extremes in the acceleration range of +/- 0.003 g to +/- 0.025 g, noted during field tests. Instrument sensitivities were adequate to record these low g (acceleration) levels. The response point of Figure B.15 is located on the south abutment and the response of Figure B.16 is near the middle of the south span on the west edge of the box-girder.

Figure B.17 is a time trace of a typical hammer impact. The magnitude of the frequency spectrum for the hammer is shown in Figure B.18. The hammer was designed to provide sufficient energy content in the DC to 100 Hz frequency range to increase the response above background noise levels. A slight ripple in the frequency response depicted in Figure B.18 may be a result of the secondary peak present in the time trace.

B.5 Modal Test Instrumentation Layout

Frequency response functions (FRFs), auto-spectrums, cross-spectrums, coherence functions, and time data were collected using acquisition/analysis software provided with each analyzer. Figure B.19 is a typical FRF for a vertical response of the deck. The corresponding coherence function is shown directly below the FRF. Coherence is very high for all modes extracted from the FRF data. FRFs were transferred to MEScope Version 2.0 and natural frequencies, modal damping, and mode shapes were extracted. Figure B.20 shows a plan and profile views denoting the location of modal test response points.

B.5.1 Modal Measurements for December 1997 Test Period

Seven response points were monitored in each instrument setup. Five impacts were recorded in each setup and an average FRF computed for each response point. Time data were stored for the last measurement in each setup. A common instrument setup was used for all seven modal setups. Each Zonic analyzer instrument channel was attached to an individual accelerometer during the first setup, and the system was calibrated using a linear calibration factor for each accelerometer. These channel-accelerometer relations were then maintained throughout the remaining test setups. Common modal test instrument settings are summarized in Table B.6. Spectral resolution of the resulting FRFs was 0.125 Hz. Accelerometer and load cell calibration factors used to generate modal response data are listed in Table B.7. Table B.8 identifies actual global degrees of freedom measured at each response location.

B.5.2 Modal Measurements for September 1998 Test Period

Fifteen analyzer instrument channels were assigned to five triaxial accelerometers. Their corresponding directional inputs and the relationships were maintained during all modal testing. The system was calibrated using a linear calibration factor for each accelerometer axis. Common modal test instrument settings are summarized in Table B.9. Spectral resolution of the resulting FRFs was 0.0625 Hz. All response data were saved as time traces and FRFs extracted off-line. Three global Cartesian accelerations were recorded at all response points.

B.5.3 Discussion of Modal Testing Process

Instrumentation and cabling were confined to the overcrossing shoulder beyond the outside pavement stripe during testing. Traffic was not stopped and overcrossing flow impeded only to the extent needed to protect the instrumentation placed on shoulder stripping with traffic cones. Measurements on the center bend were accomplished from above by dropping cabling over the side into guardrail protected median area.

B.6 Modal Analysis of Field Measurements

ME'scope Version 2.0 was used to analyze frequency response functions (FRFs) derived from time data collected during the two test periods. FRFs for each response point were

transferred to ME'scope via the Universal File Format (UFF). The structure was modeled in ME'scope as a wireframe and FRFs associated with the appropriate degree of freedom (DOF) at each response location. The remaining unmeasured DOFs in the structure were either slaved to weight averages of known DOFs or fixed. Using a cumulative FRF summing algorithm, a composite FRF for the whole structure was generated to highlight all possible modal frequencies. The analysis frequency range was limited to DC-30 Hz because of the dropout in hammer energy above this point and because this range covered about ten to twelve major lower modes of the structure. The wireframe model of the structure and the FRF response points are shown in Figure B.21. Note that response of the column, points 27 through 30, were not measured along the columns central axis but on the surface of the column in the transverse and longitudinal directions.

B.6.1 Modal Analysis Results for December 1997 Test Period

FRFs from this baseline test were grouped in two analysis subsets. The first analysis subset focused on vertical bending and torsion modes while the second was used to determine transverse bending modes. Most of the modal energy in the system responses was concentrated in the vertical bending and torsion modes. ME'scope Version 2.0 was used to analyze both data sets. The frequency range of analysis was limited to DC-30 Hz which spanned the first ten to twelve structural modes. The ten unique modes extracted from the baseline data are summarized in Table B.10. The Modal Assurance Criteria (MAC) for the modes in this analysis indicated several coupled or complex modes.

Vertical and Torisonal Mode Analysis

Several independent and coupled bending and torsion modes were found for the superstructure. The frequencies and damping of these modes are summarized in Table B.10. Corresponding mode shapes are shown in Figures B.22 through B.31. The modal assurance criteria (MAC) for the modes in this analysis set indicate several coupled or complex modes and are indicated in Table B.10.

Transverse Mode Analysis

Fewer modes were identified in the transverse direction. Many of the modes identified had identical frequencies to certain modes found in vertical and torsion analysis data set. The modes are assumed to result from crosstalk with these other modes and are not discussed here. Four modes in this second set do have unique characteristics and are reported here. The frequencies and damping of these modes are summarized in Table B.11. Corresponding mode shapes are shown in Figures B.32 through B.35. Two modes appear to be independent transverse modes; the others are complex.

B.6.2 Modal Analysis Results for September 1998 Test Period

This replication of the first field test provided the second point of a trend line defining the capacity and serviceability of the structure. A unified data set containing multi-DOF nodal accelerations was analyzed and modal parameters extracted. The frequency range of analysis was again limited to DC-30 Hz. Table B.12 lists structural parameters for this test period. Figure B.36 depicts a composite plot of vertical motion FRFs for the structure. Note that several of the fitted parameter frequencies in Table B.12 are evident in the figure. Figures B.37 through B.40 depict the first four structural mode shapes. A review of the frequencies for the two field tests indicates that slight shifts in the modal characteristics, generally frequency, have occurred in the structure. In particular, the frequency of Mode 1 increased from 3.10 Hz to 3.30 Hz. In the second data set the transverse mode was not separable due to overlaps with other modes. These variations are attributed to environmental changes such as temperature, humidity, abutment support characteristics, and possible instrumentation differences. In general, material degradation should decrease modal frequencies since it reduces the elastic modulus of the concrete.

B.7 Summary and Conclusions

Review of testing reported here indicates sequential collection of modal data using portable instrumentation and a small impact hammer works well in providing the lower-mode modal data for NDE of medium length (100 – 200 ft.) span bridge structures or even larger

structures consisting of combinations of medium length spans. In addition, on the basis of the results generated during the testing, the following conclusions are proposed:

- The results of the modal analysis were very good.
- Some complex modes were found but most fundamental mode shapes and frequencies were in good agreement with analytical results.
- Recorded data had a good signal to noise ratio.
- Responses of the sensors were well above ambient noise levels created by nearby traffic.
- The impact load provided by the mobile drop hammer along with sufficiently responsive accelerometers were capable of determining modal parameters of the box-girder structure.
- An impact of approximately 3000 lb peak over 50 ms was sufficient to excite structural modes needed for damage detection.
- The response accelerations were in the +/- 15 mg range.
- The results from this testing indicate it is possible to acquire modal data on structures of relatively large size without impeding the usability of the structure during testing.
- The total field test time for mobilization, travel, set up, and data collection on a structure tested here is one to two days.

Table B.1 PCB 393A03 accelerometer specifications

Sensitivity	1000	mV/g
Frequency range (+/- 5%)	0.5 - 2000	Hz
Amplitude range	+/-5	g peak
Resolution	0.000005	g
Linearity	+/-1	%
Transverse sensitivity	<5	%
Weight	210(7.4)	gram(oz)

Table B.2 PCB 200C20 piezoelectric load cell specifications

Sensitivity	.256	mV/lbf
Rise time	< 15	micro-seconds
Amplitude range	0 - 20000	lbf
Discharge time constant	>2000	Sec
Linearity	<1	%full-scale

Table B.3 Zonic 2300 analyzer specifications

Channels	8	
Frequency range	20	kHz/channel
Channel match: Amplitude Phase	 +/- 1 +/- 1	 dB degree
Dynamic range	> 80	dB
Crosstalk	< 75	dB
A/D resolution	16	bit sigma delta
Anti-alias filters	80	dB rejection)

Table B.4 Kistler 8390A2 accelerometer specifications

Sensitivity	500	mV/g
Frequency range (+/- 5%)	DC – 150	Hz
Amplitude range	+/-2	g peak
Resolution (broadband)	1.5	mg
Linearity	+/-1	%FS
Transverse sensitivity	< 5	%
Weight	210(7.4)	gram(oz)

Table B.5 SigLab 20-42 analyzer specifications

Channels	16	
Frequency range	20	kHz/channel
Channel match: Amplitude Phase	 +/- 1 +/- 1	 dB Degree
Dynamic range	> 84	dB
A/D resolution	20	bit sigma delta
Anti-alias filters	>90	dB rejection

Table B.6 Modal test instrument settings (1997)

Test Parameter	Value	Notes/Units
Accelerometer channels	2, 3, 4, 5, 6, 7, 8	Zonic instrument channel
Load cell channel	1	Zonic instrument channel
Sample frequency	512	Hz
Sample length	4096	Samples per channel
Spectral Resolution	0.125	Hz
Number of repetitions	5	Linear average
Channel gain	Varied	Adjusted for overloading
Trigger method	+ 5% Load cell fullscale	Pretrigger save all channels
Accelerometer window	Exponential	99% down at end
Load cell window	Rectangular	10% Window width

Table B.7 Sensor calibration factors for modal tests (1997)

Sensor	Zonic Channel	Calibration Factor	
PCB 200C20 SN3325	1	0.256	mV/lb
PCB 393A03 SN5394	2	960	mV/g
PCB 393A03 SN5395	3	986	mV/g
PCB 393A03 SN5396	4	971	mV/g
PCB 393A03 SN5397	5	965	mV/g
PCB 393A03 SN5398	6	996	mV/g
PCB 393A03 SN5399	7	969	mV/g
PCB 393A03 SN5400	8	994	mV/g

Table B.8 Measured global degrees of freedom at response points (1997)

DOF	x-dir	y-dir	z-dir
1		X	X
2		X	X
3		X	X
4		X	X
5		X	X
6		X	X
7		X	X
8		X	X
9		X	X
10		X	X
11		X	X
12		X	X
13		X	X
14			X
15			X
16			X
17			X
18			X
19			X
20			X
21			X
22			X
23			X
24			X
25			X
26			X
27	X	X	
28	X	X	
29	X	X	
30	X	X	

Table B.9 Modal test instrument settings (1998)

Test Parameter	Value	Notes/Units
Accelerometer channels	2-16 each accelerometer connected in sequence	Siglab channels
Load cell channel	1	Siglab channel
Sample frequency	512	Hz
Sample length	8192	Samples per channel
Spectral Resolution	0.0625	Hz
Number of repetitions	5	Linear average
Channel gain	Varied	Adjusted for overloading
Trigger method	+ 25% Load cell fullscale	Pretrigger save all channels
Accelerometer window	Boxcar	
Load cell window	Boxcar	

Table B.10 Frequency and damping of modes for vertical and torsional modes (1997)

Mode	Frequency Hz	Damping %	Mode Type
1	3.10	3.5	1st Longitudinal bending mode
2	4.43	3.3	2nd Longitudinal bending mode
3	6.78	2.0	1st Torsion mode
4	8.32	2.7	Complex 2nd Torsion mode with some bending in south span
5	10.58	1.9	Complex -- 2nd torsion mode with bending component
6	11.64	4.0	3rd Bending mode
7	14.46	1.7	3rd Torsion mode
8	20.72	1.3	4th Torsion mode
9	23.35	1.1	Bending mode, possible harmonic of 3rd
10	24.42	1.8	5th Torsion mode

Table B.11 Frequency and damping of modes in transverse analysis (1997)

Mode	Frequency Hz	Damping %	Mode Type
1	3.22	3.1	1st Transverse bending mode
2	8.31	3.9	Complex 2nd mode
3	10.59	1.9	Complex 2nd mode
4	20.68	1.29	Possible transverse bending mode

Table B.12 Frequency and damping from 1998 modal analysis

Mode	Frequency Hz	Damping %
1	3.35	3.51
2	4.82	3.30
3	6.73	2.34
4	8.75	2.57
5	10.63	2.10
6	12.93	3.65
7	14.62	2.33
8	20.55	1.69
9	20.93	1.30
10	21.71	1.58
11	24.42	1.87
12	27.04	1.95
13	29.01	1.01

Figure B.1 View of east face of superstructure from freeway

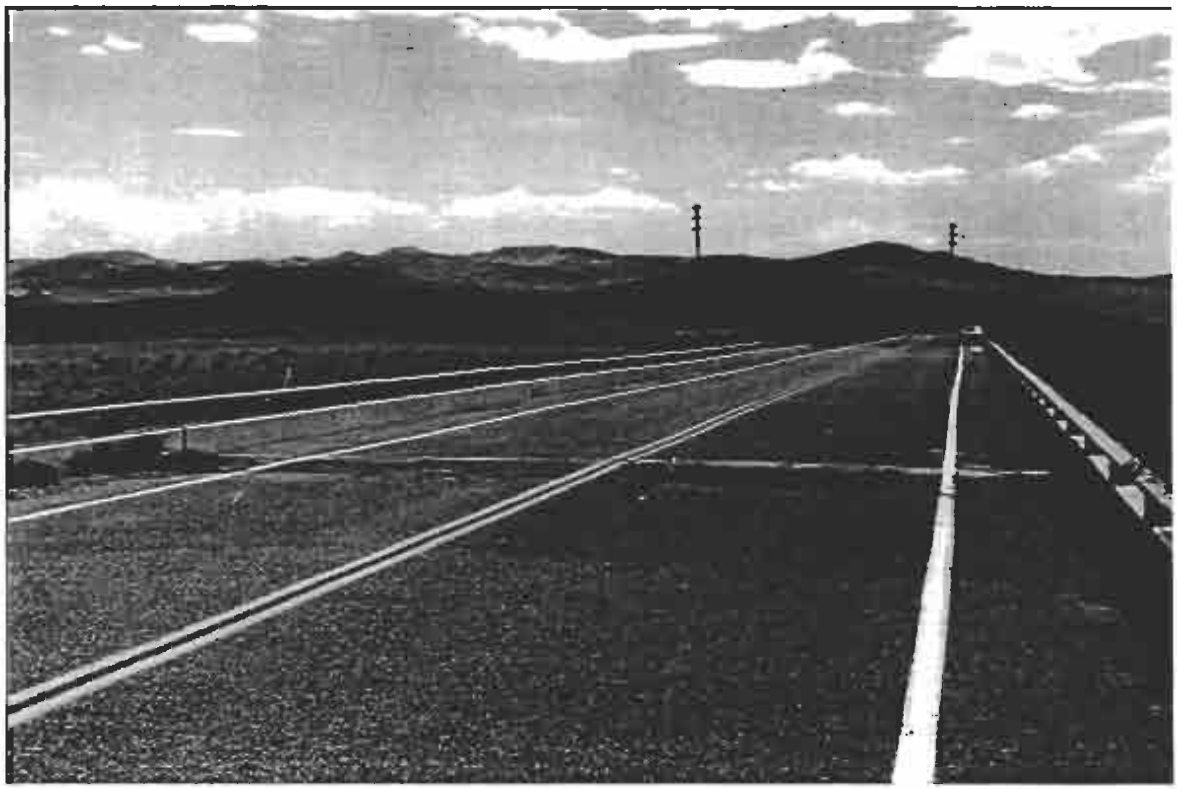

Figure B.2 View of bridge deck from north approach

Figure B.3 South abutment and east face superstructure from freeway

Figure B.4 Profile view of superstructure at abutment connection

Figure B.5 Grouted expansion joint

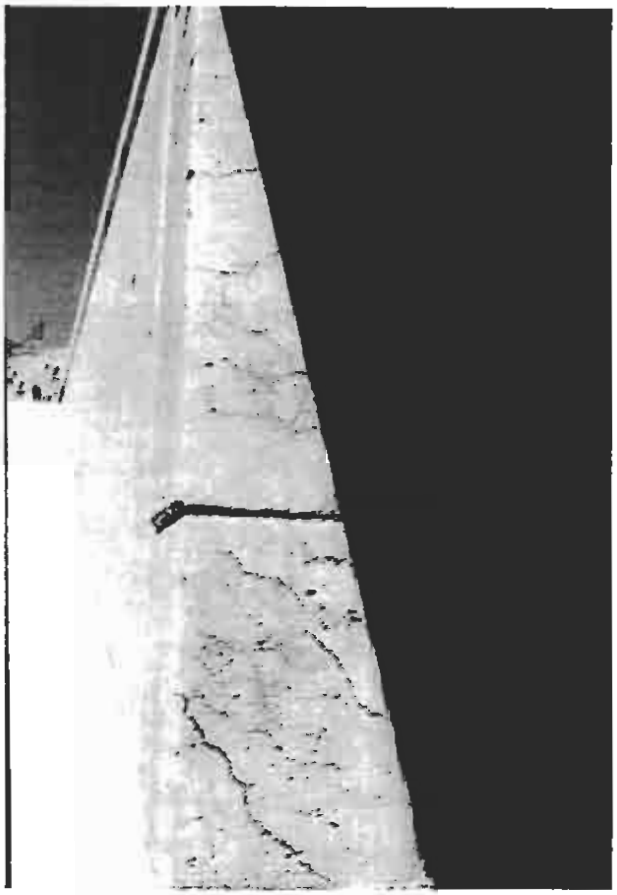

Figure B.6 Wingwall Deterioration

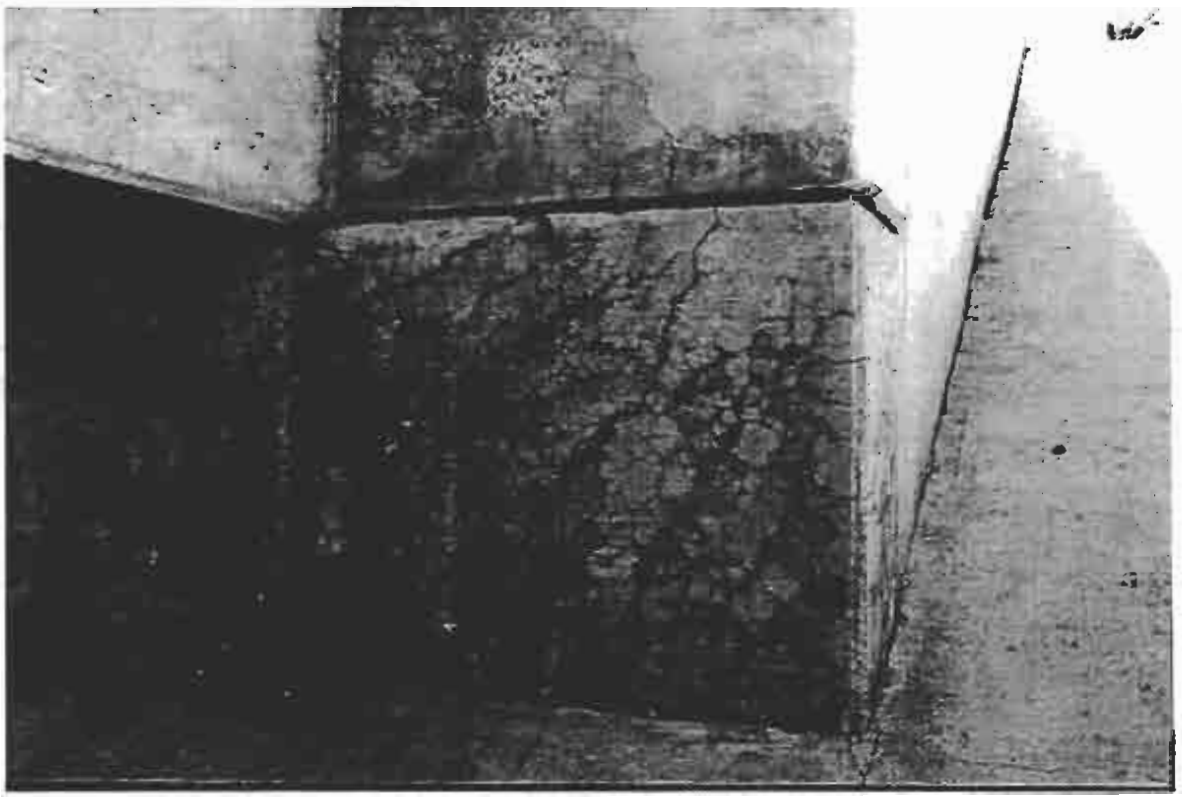

Figure B.7 Visible deterioration of abutment

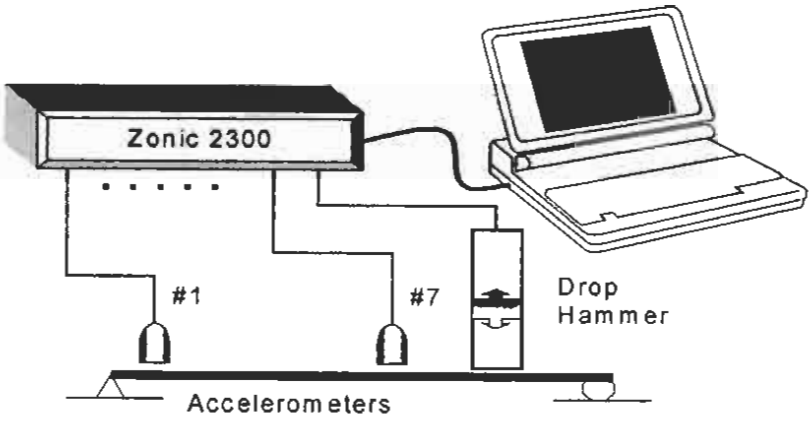

Figure B.8 Schematic of basic instrumentation setup

Figure B.9 Accelerometer installation on deck

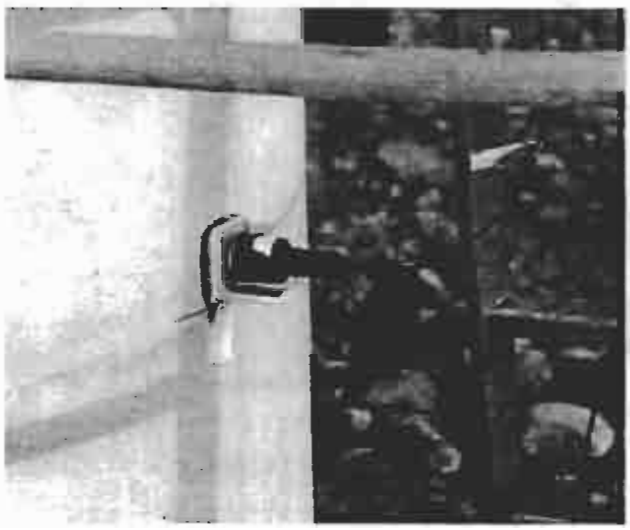

Figure B.10 Accelerometer column installation

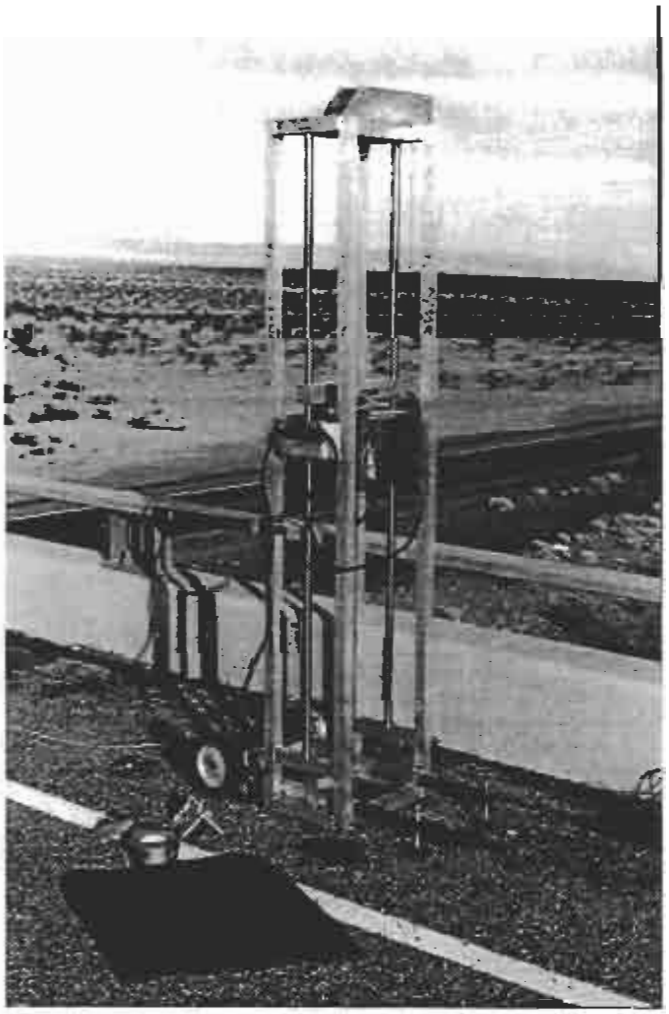

Figure B.11 Impact hammer

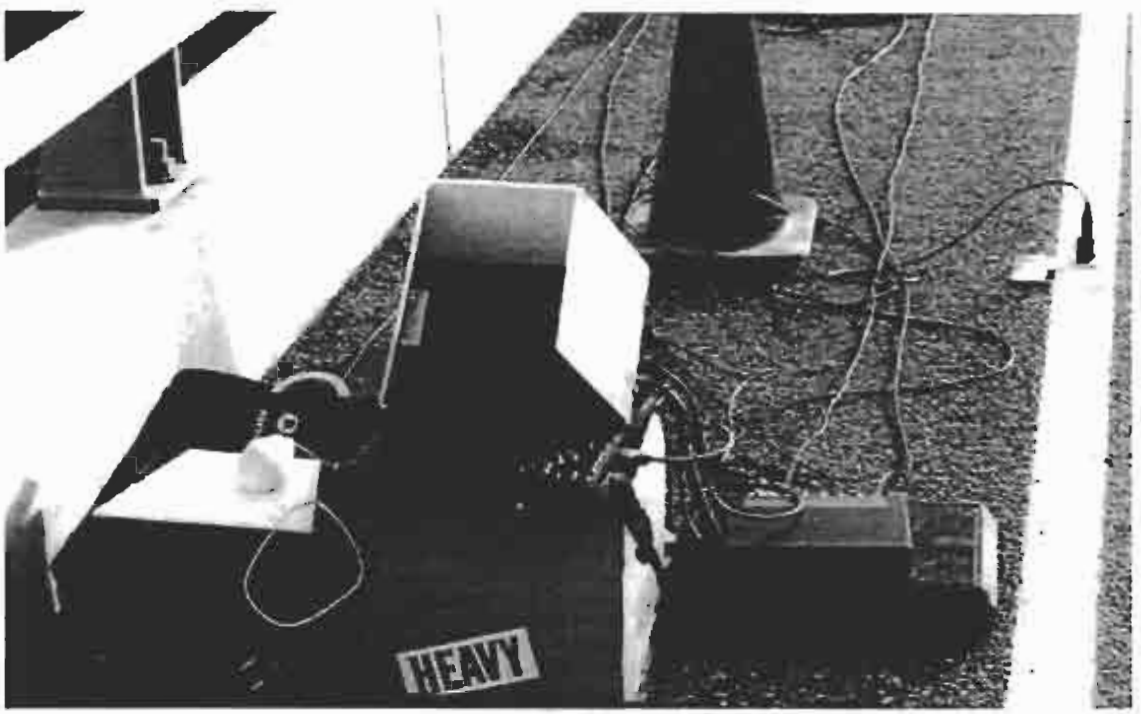

Figure B.12 Acquisition instrumentation for first field test

Figure B.13 16-Channel instrument setup for second field test

Figure B.14 Typical triaxial accelerometer mounting

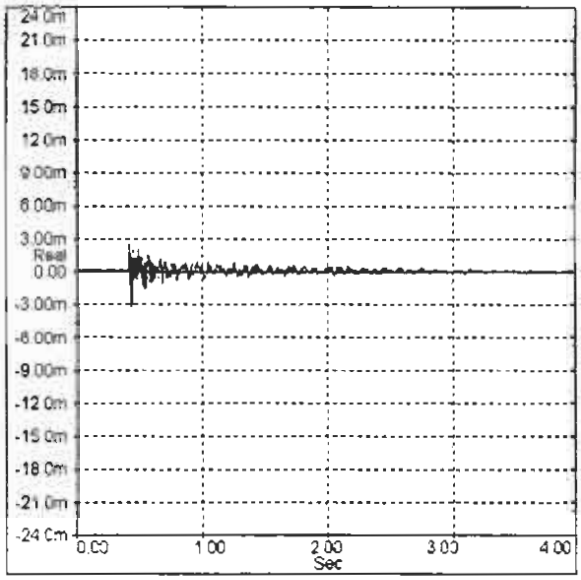

Figure B.15 Vertical response at south abutment (g)

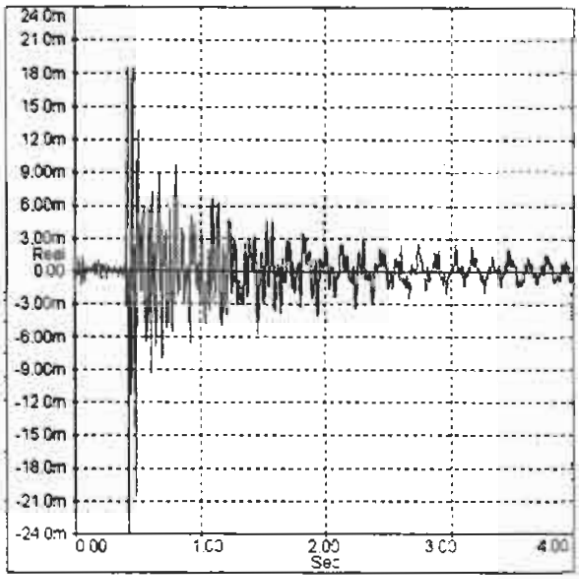

Figure B.16 Mid-span vertical response (g)

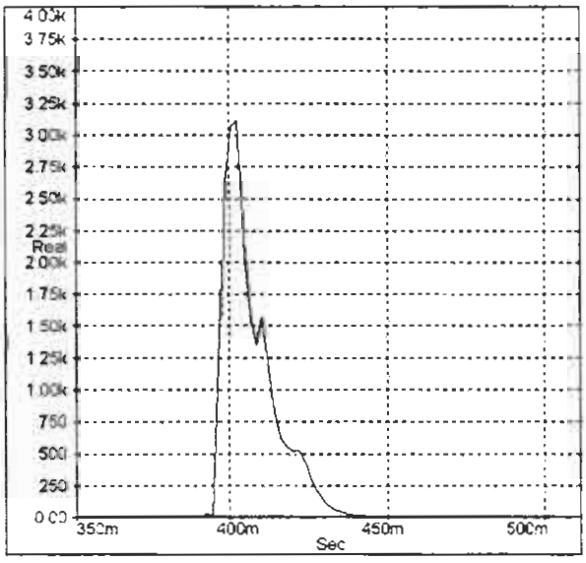

Figure B.17 Typical time response of impact hammer

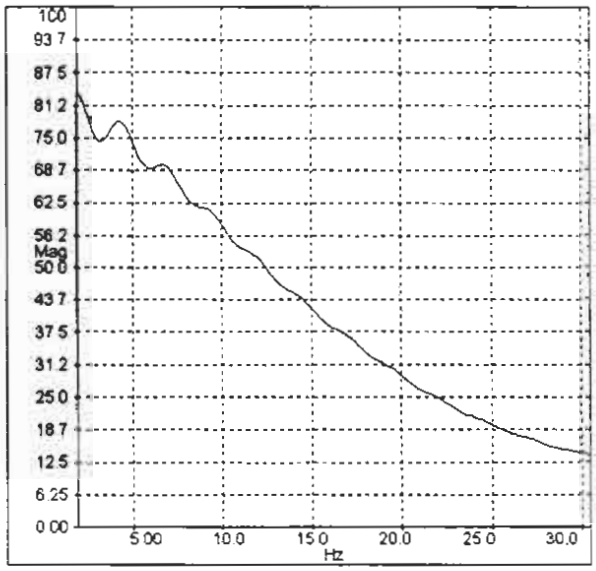

Figure B.18 Frequency spectrum of impact

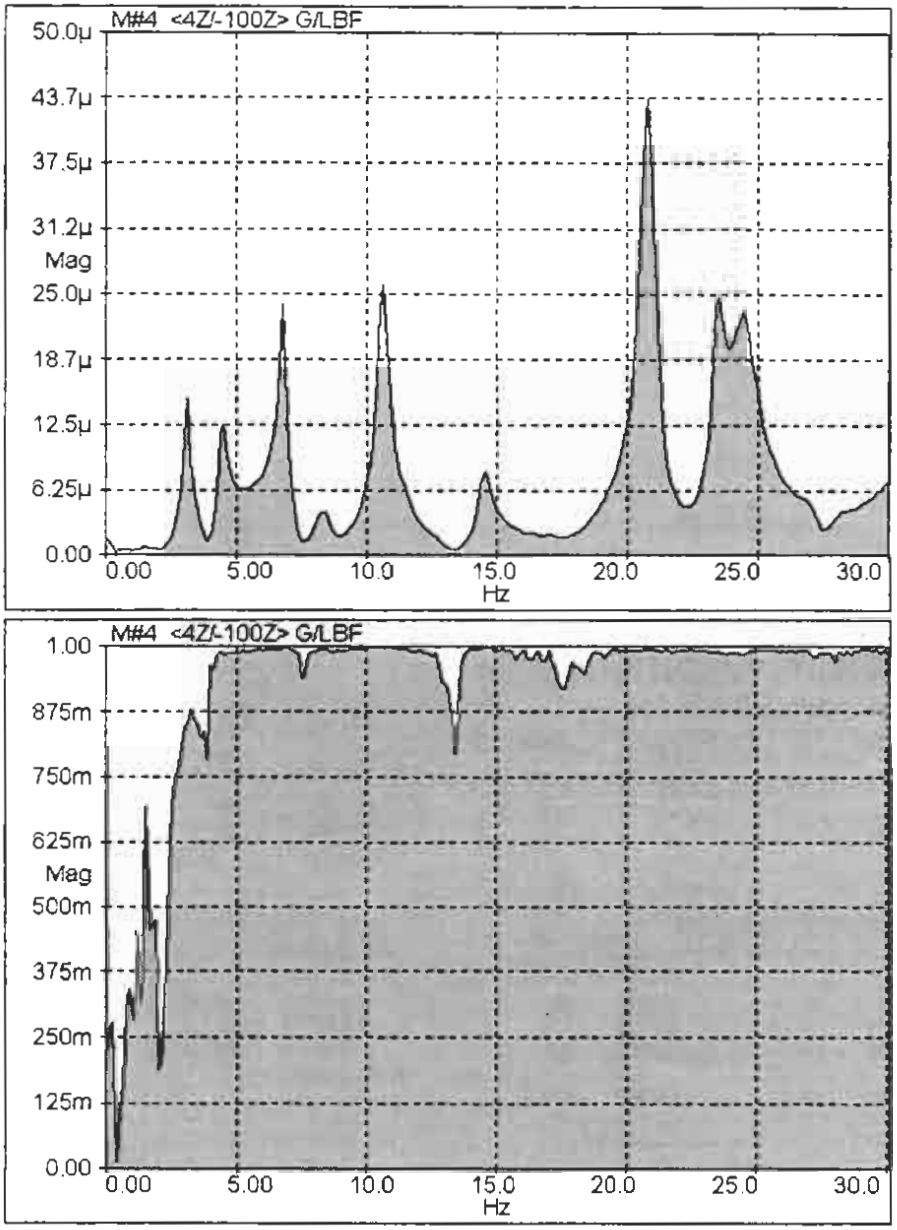

Figure B.19 Typical vertical FRF for deck response point and corresponding coherence function

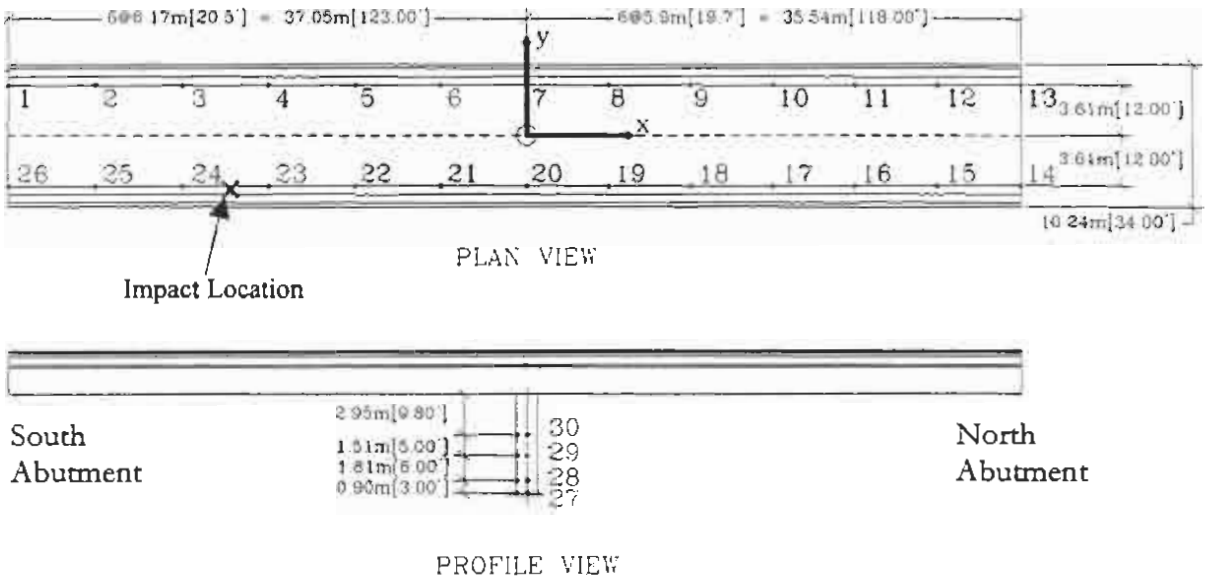

Figure B.20 Location of modal response points on superstructure

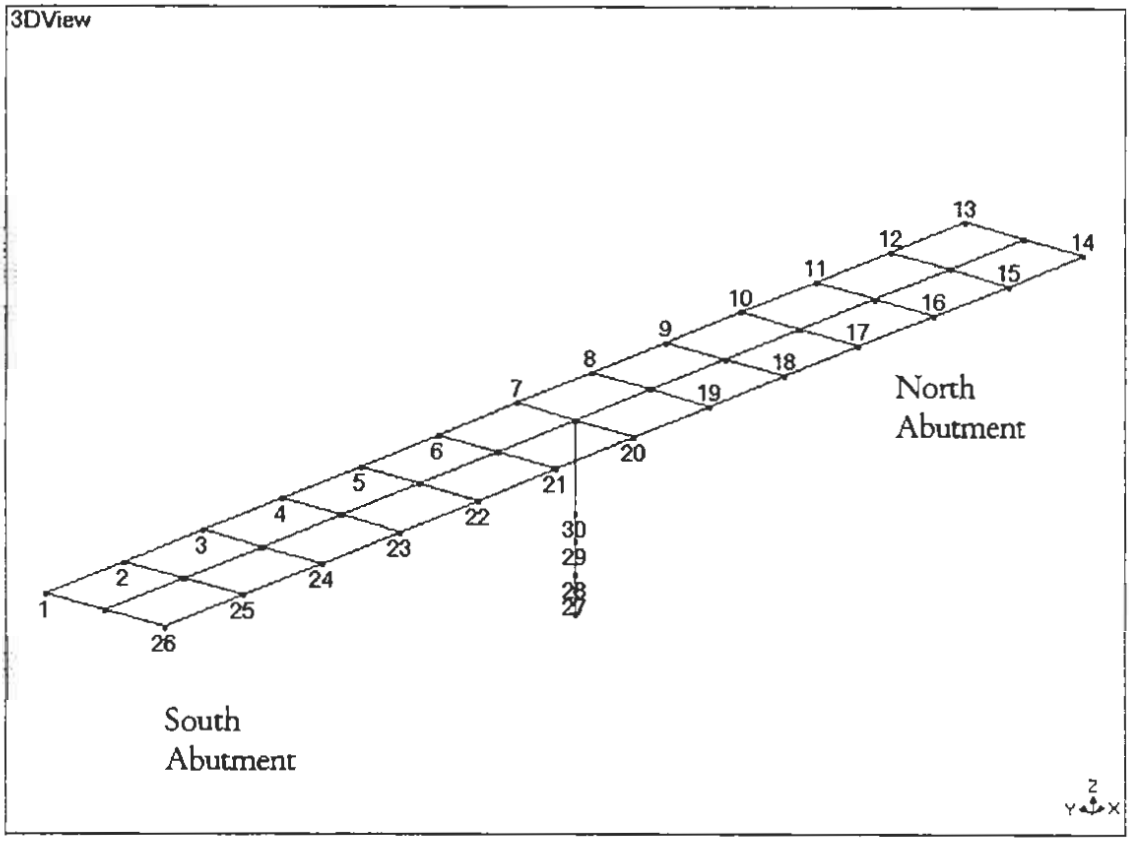

Figure B.21 Wireframe model for analysis of modal field data with response point locations shown

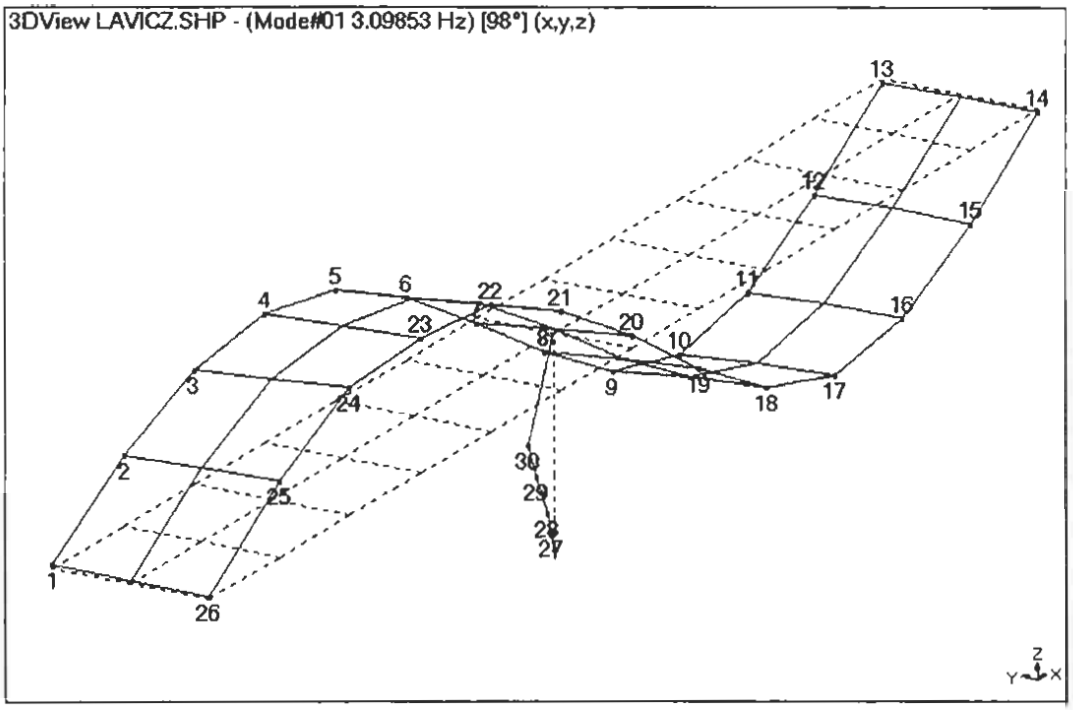

Figure B.22 Mode 1 -- 1st longitudinal bending (1997)

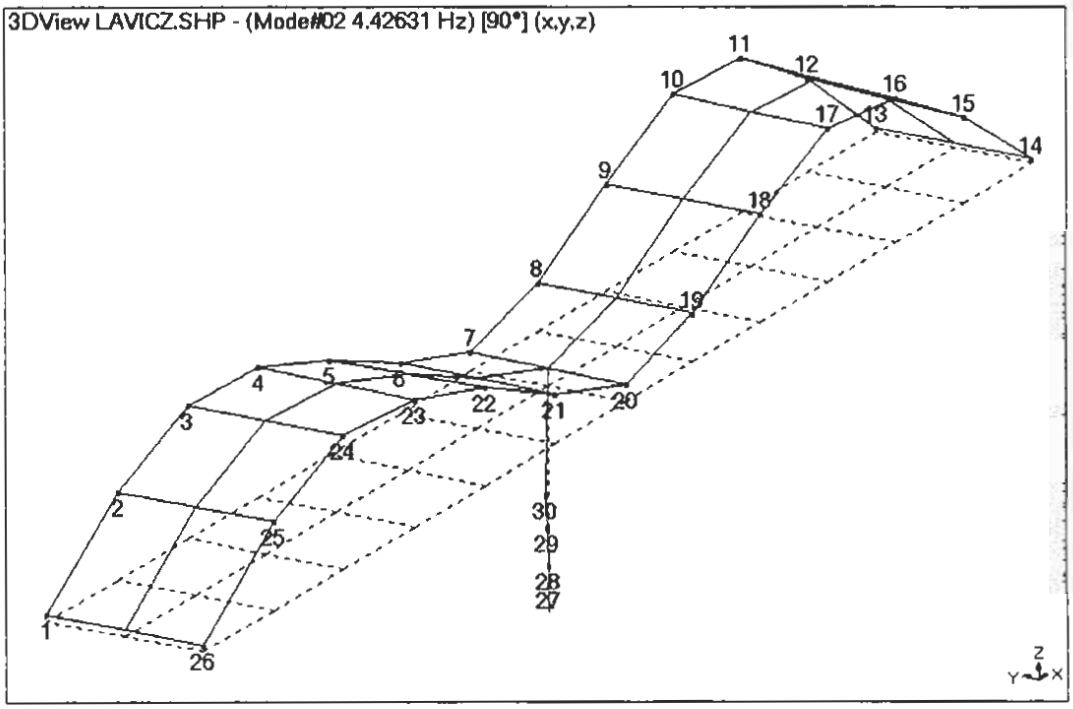

Figure B.23 Mode 2 -- 2nd longitudinal bending (1997)

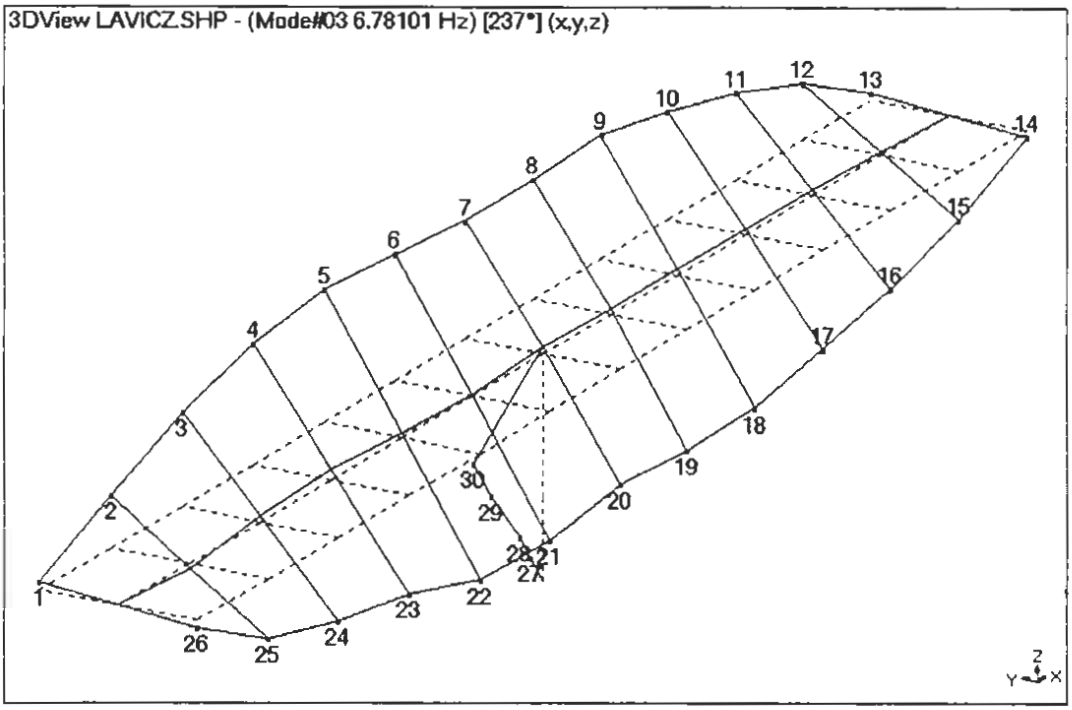

Figure B.24 Mode 3 -- 1st torsion mode (1997)

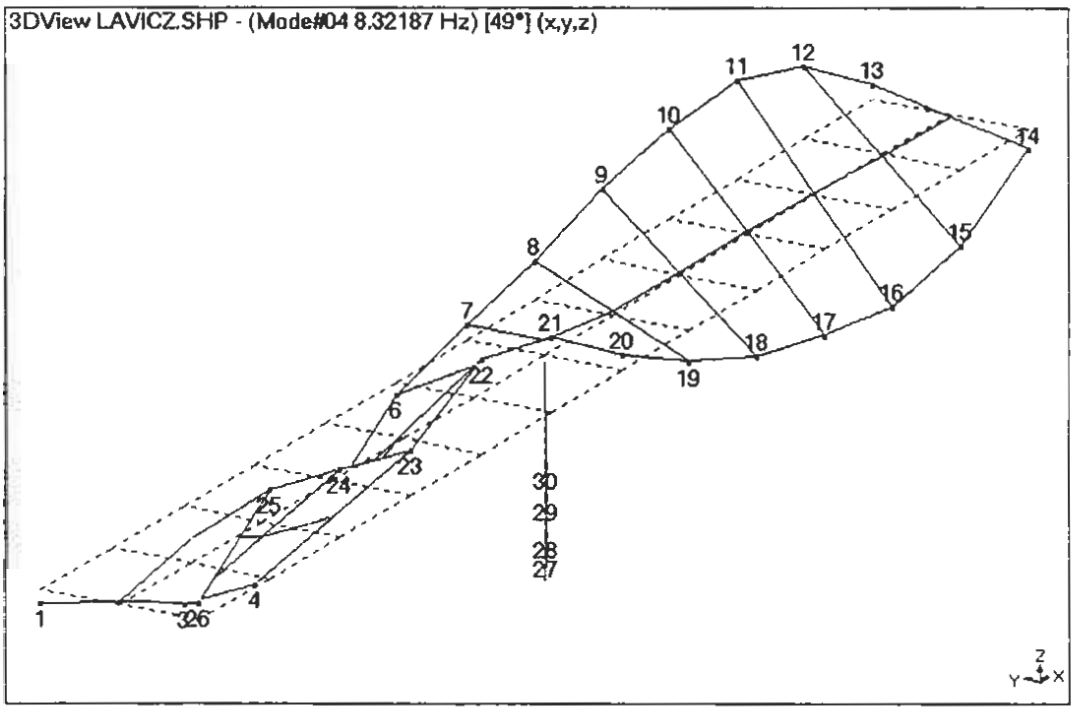

Figure B.25 Mode 4 -- Complex 2nd torsion mode some bending (1997)

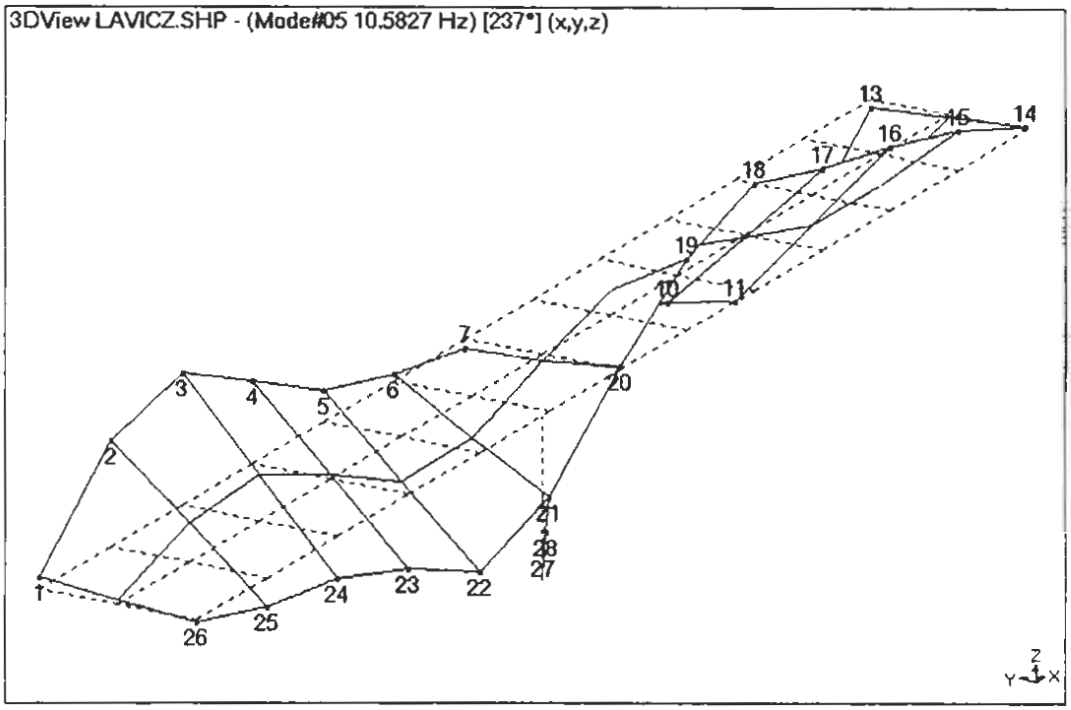

Figure B.26 Mode 5 -- Complex 2nd torsion + 3rd bending (1997)

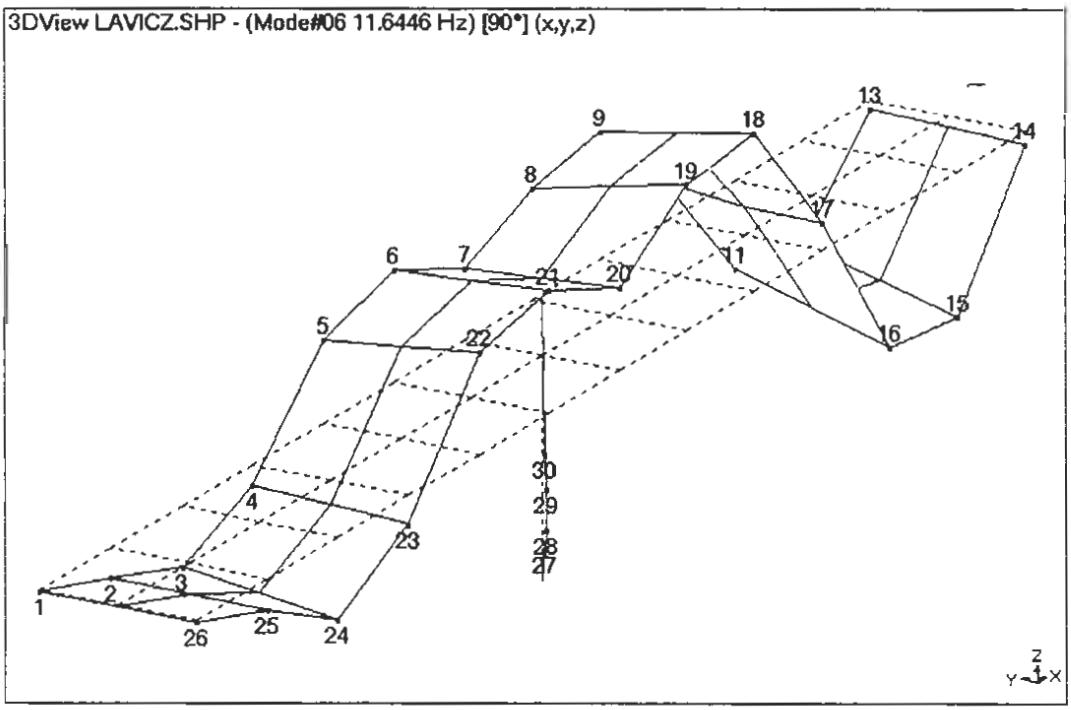

Figure B.27 Mode 6 -- 3rd longitudinal bending mode (1997)

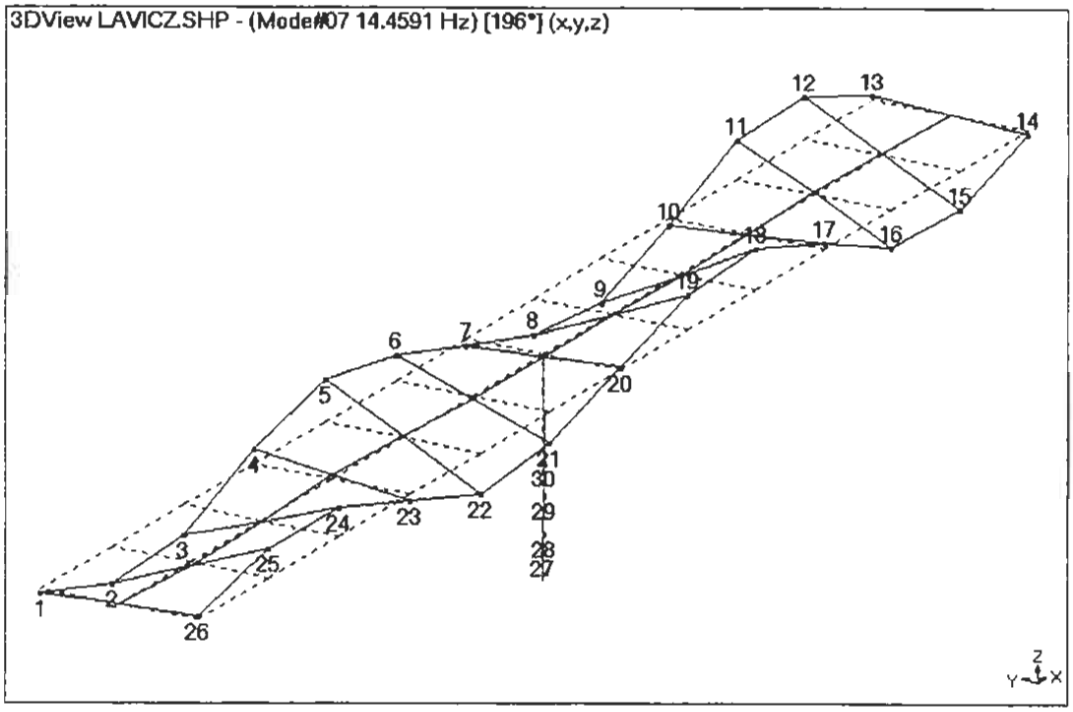

Figure B.28 Mode 7 -- 3rd torsion mode (1997)

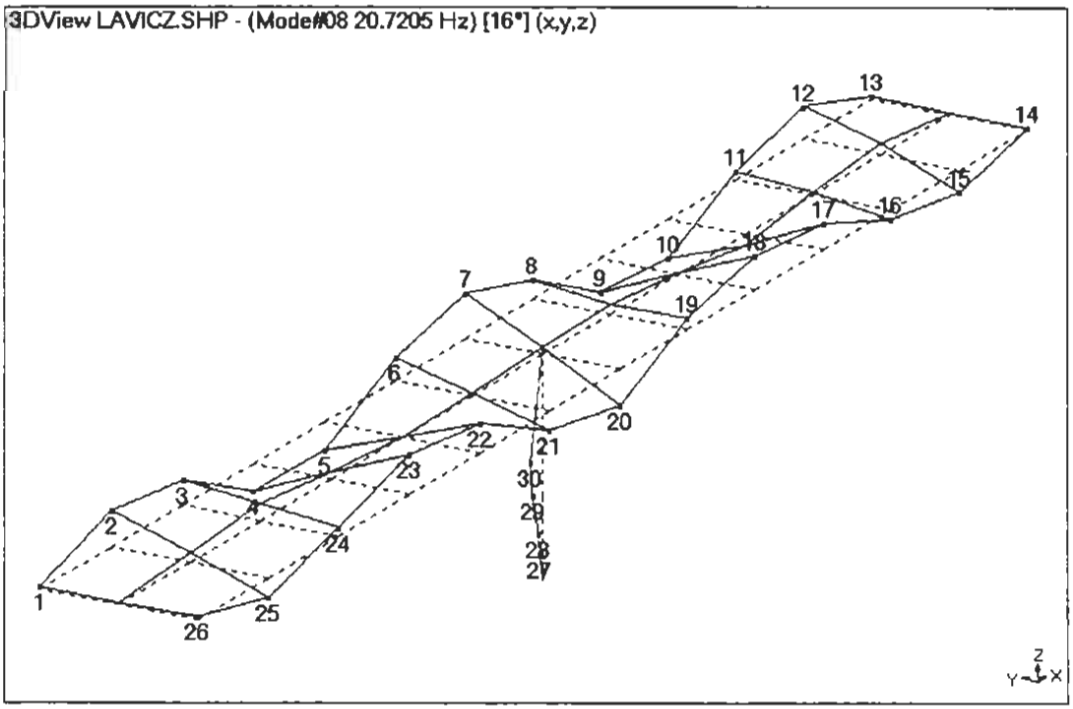

Figure B.29 Mode 8 -- 4th torsion mode (1997)

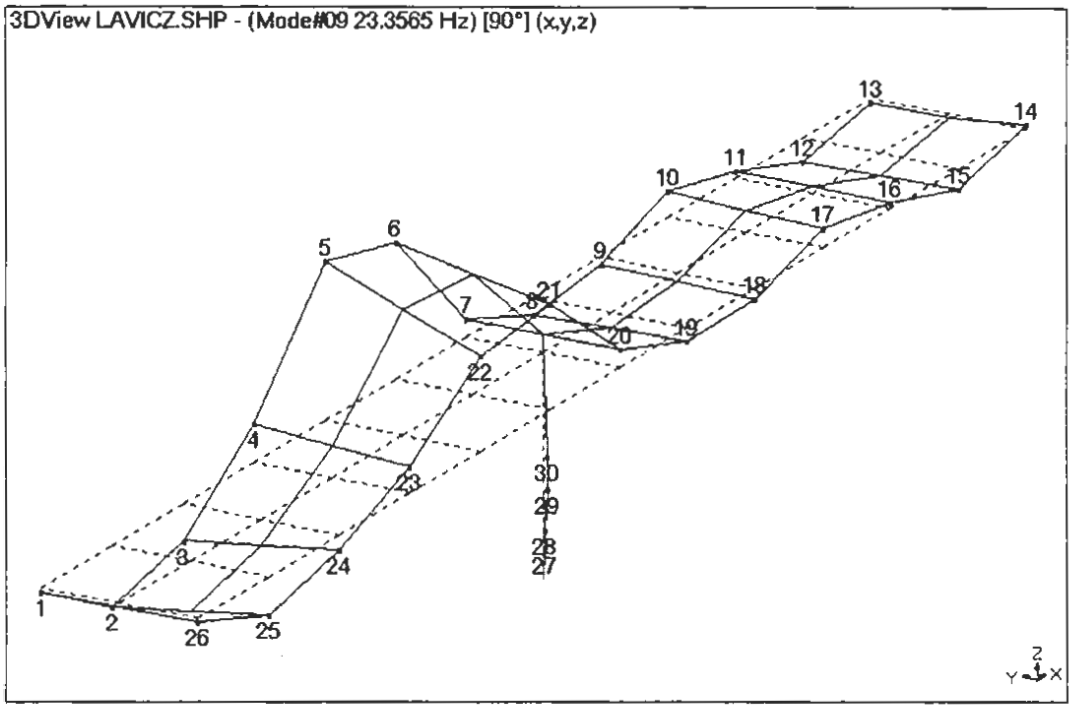

Figure B.30 Mode 9 -- Complex possible harmonic of 3rd bending mode (1997)

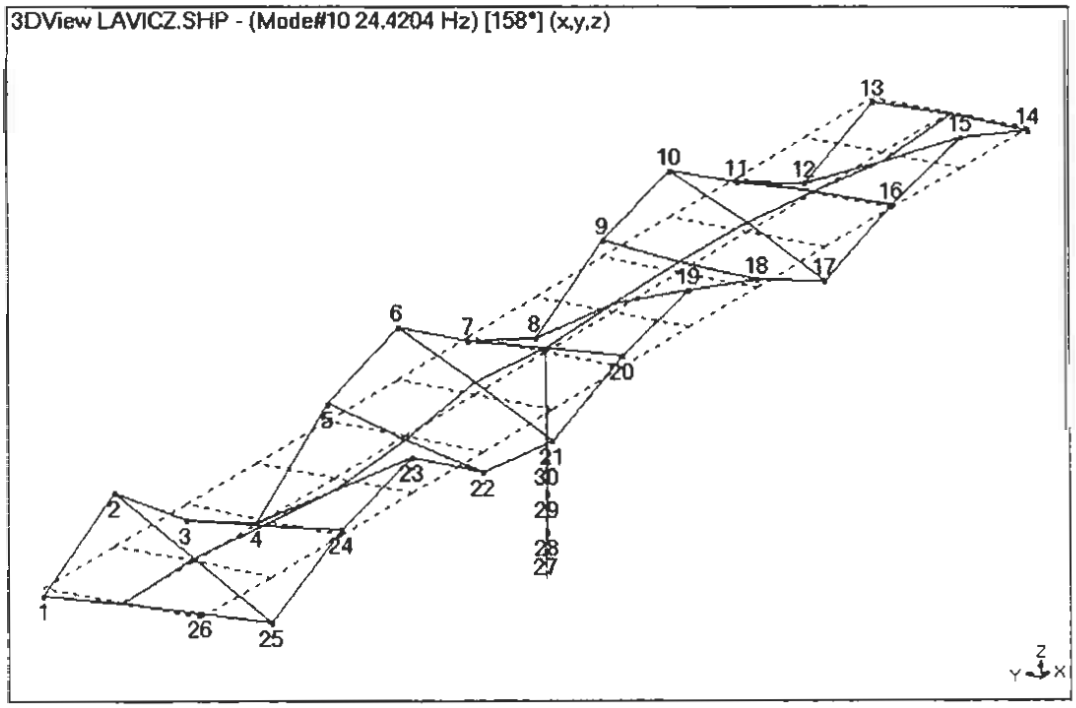

Figure B.31 Mode 10 -- 5th torsion mode (1997)

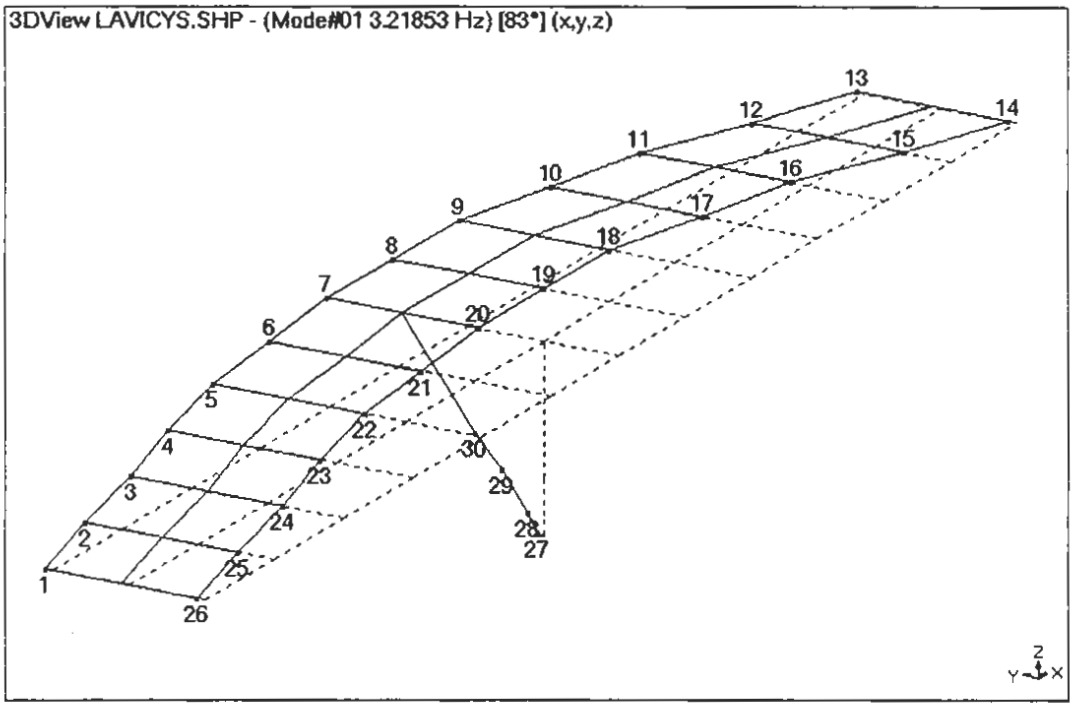

Figure B.32 Mode 1 -- 1st Transverse bending mode (1997)

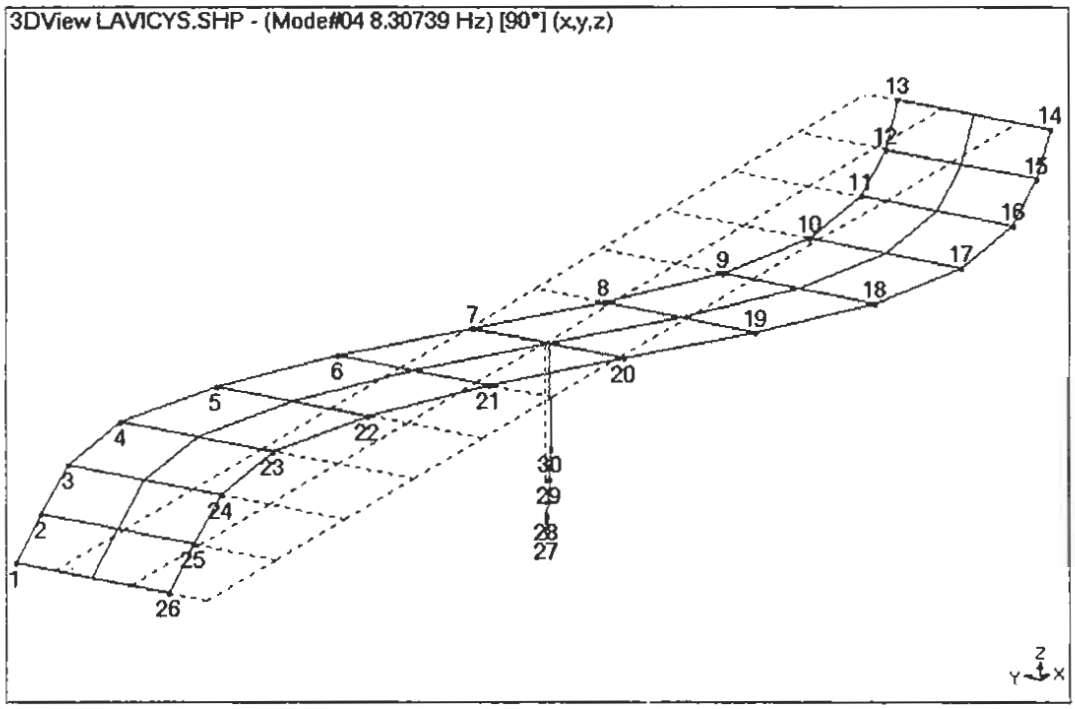

Figure B.33 Mode 4 -- Complex transverse bending mode (1997)

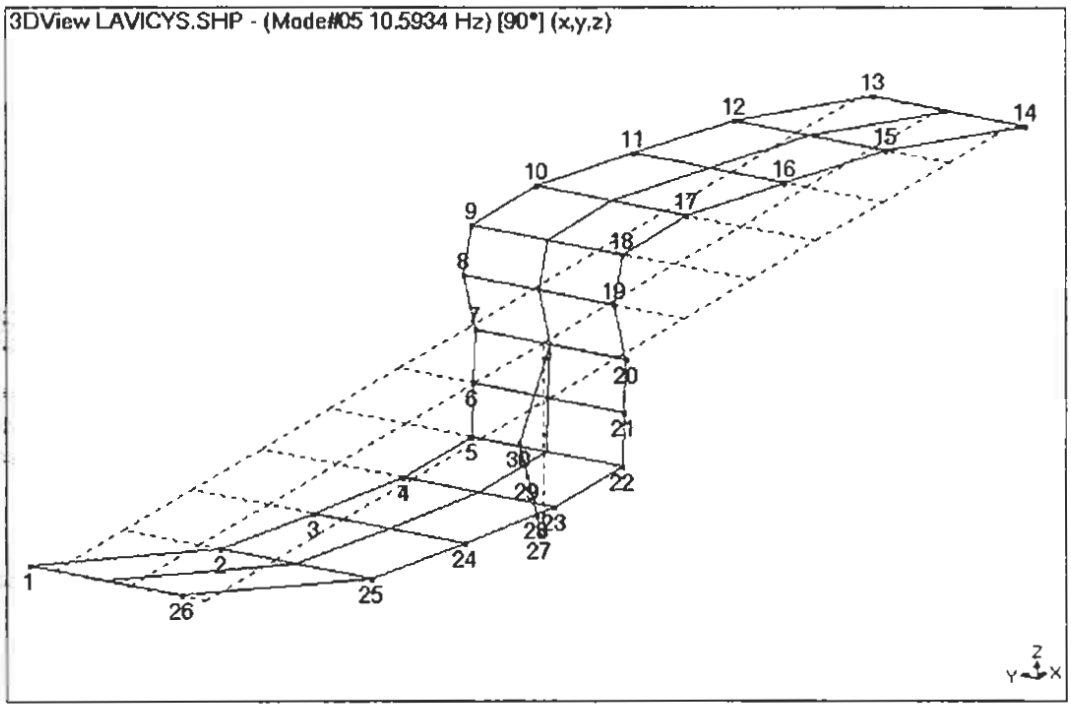

Figure B.34 Mode 5 -- Complex transverse bending mode (1997)

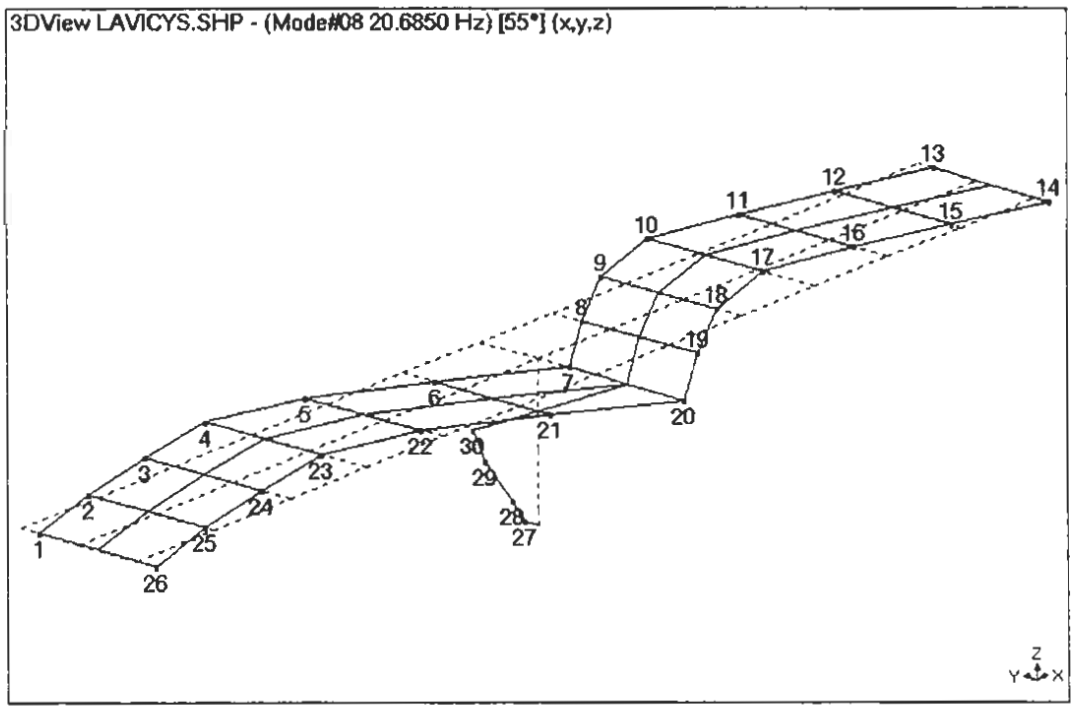

Figure B.35 Mode 8 -- Higher order transverse bending mode (1997)

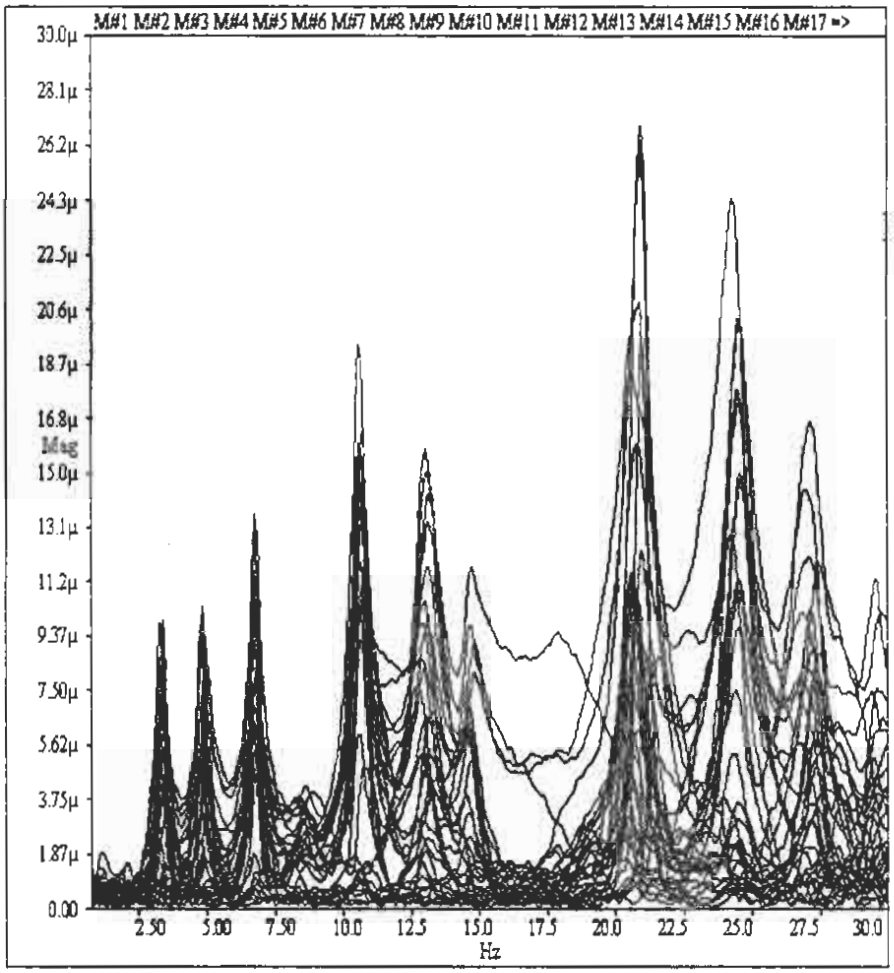

Figure B.36 Composite vertical motion FRF responses for 1998 field test

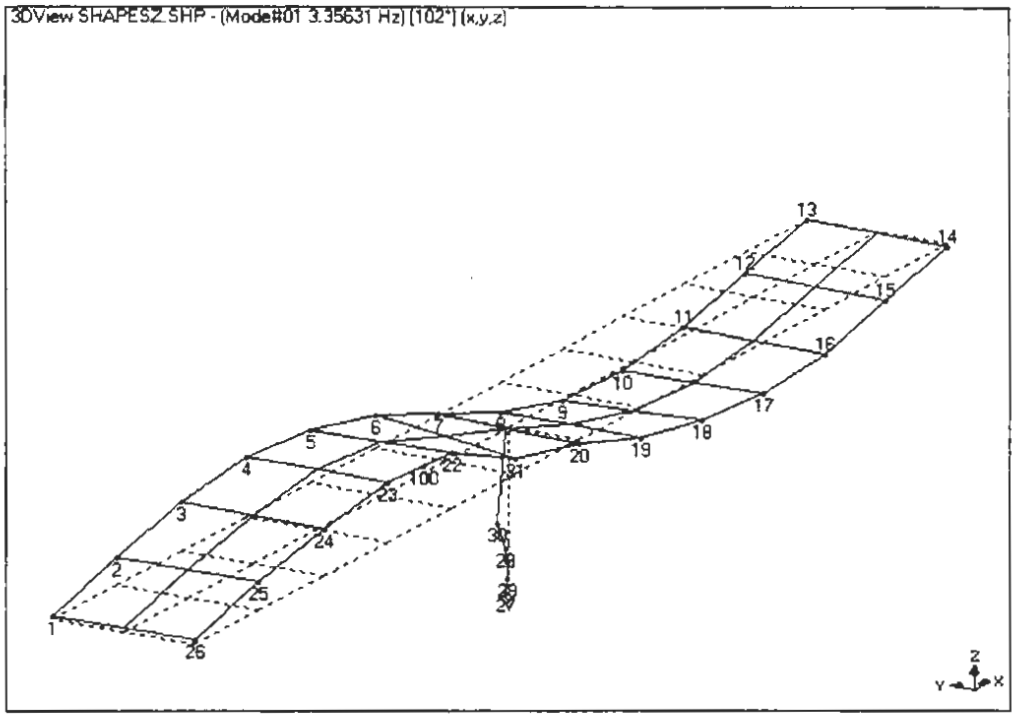

Figure B.37 Mode 1--1st bending mode(1998)

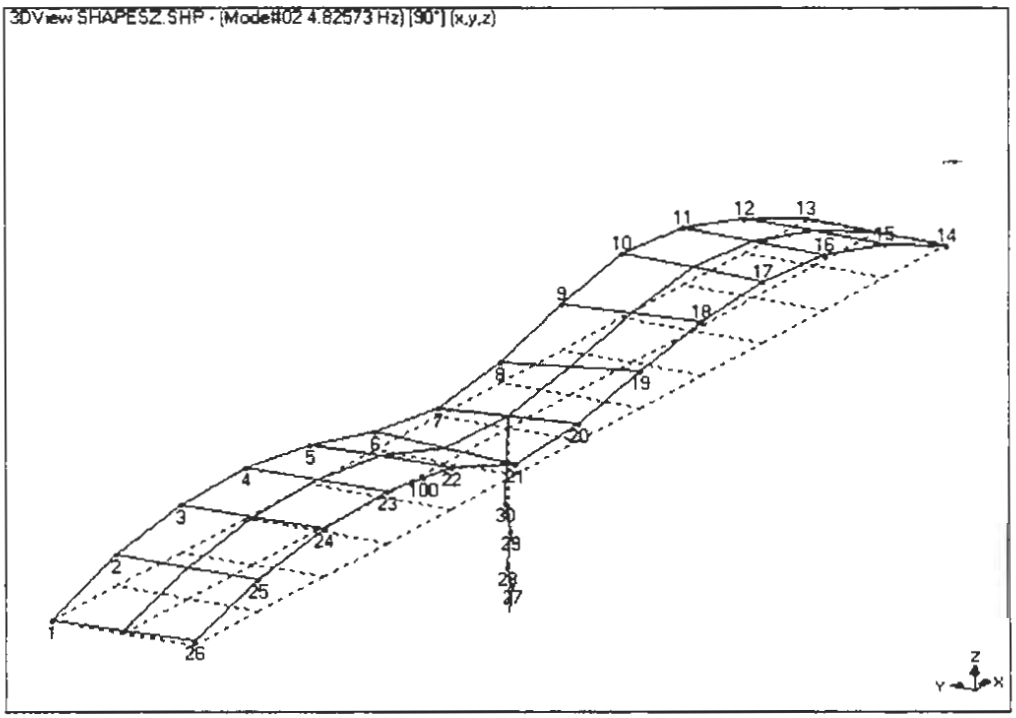

Figure B.38 Mode 2--2nd bending mode (1998)

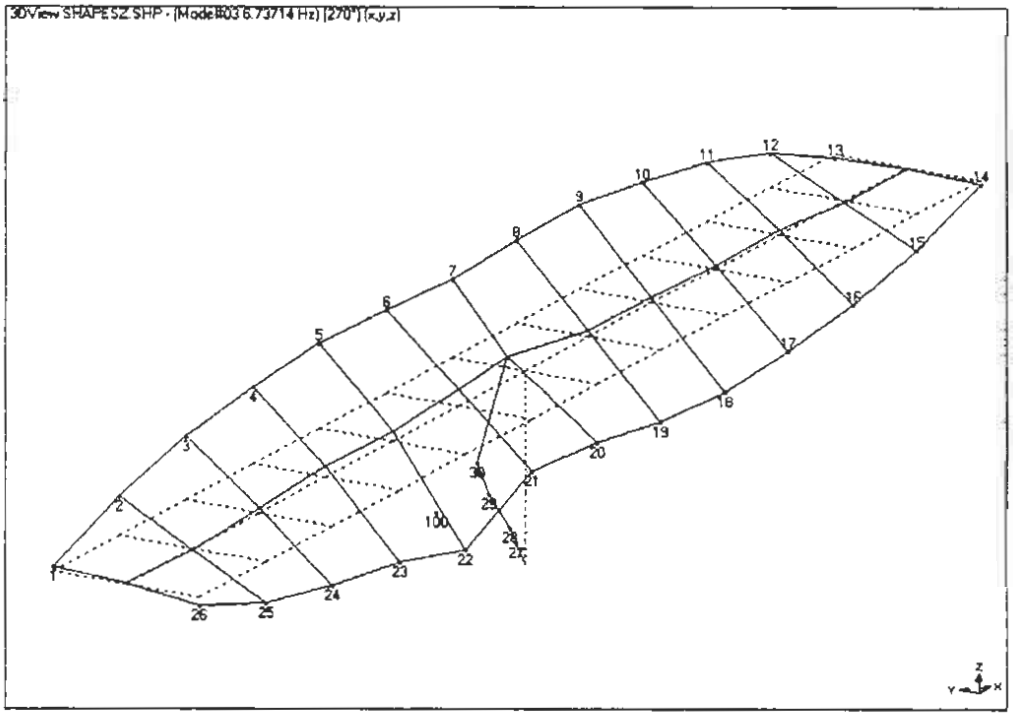

Figure B.39 Mode 3--1st Torsional mode (1998)

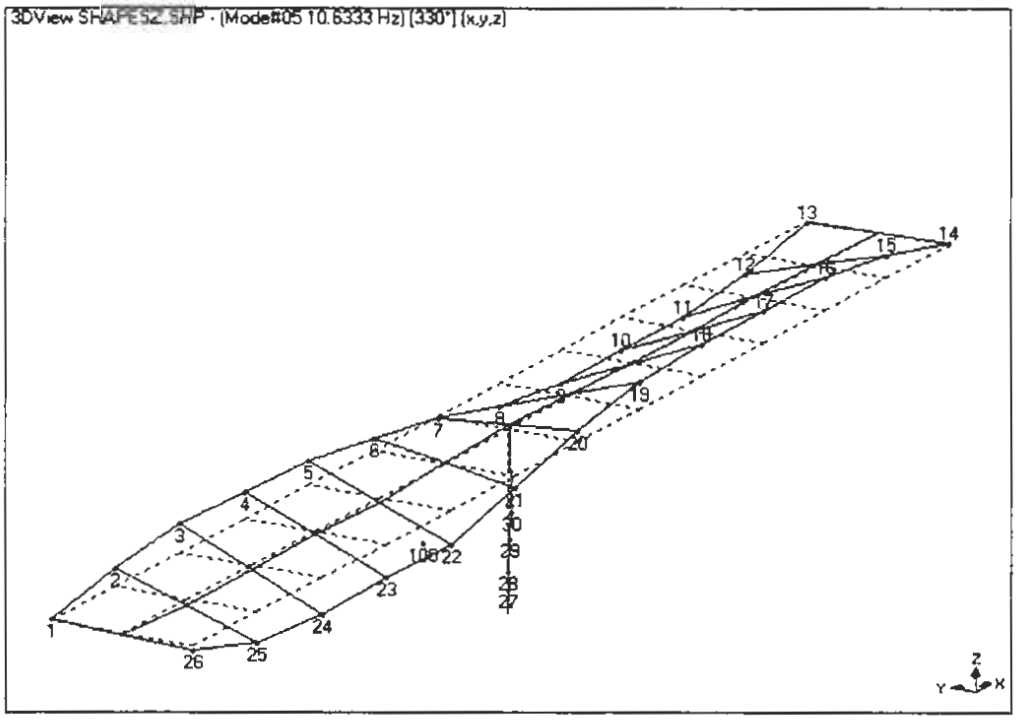

Figure B.40 Mode 4--2nd Torsional mode (1998)

APPENDIX C

MATERIAL PROPERTIES OF LAVIC ROAD OVERCROSSING USING RAYLEIGH WAVE SPEEDS

C.1 Introduction

This appendix documents the portion of the field investigation of the Lavic Road Overcrossing devoted to wave speed measurements of the superstructure and abutments. This investigation was undertaken for the California Department of Transportation (Caltrans) under Contract 59A0022 by the Texas Engineering Experiment Station. The goal of this contract is to develop formal techniques to predict the structural integrity and the remaining service life of existing concrete structures weakened by reactive aggregate used during construction of the bridge.

Experimental field data were collected from the Lavic Road Overcrossing located on Interstate 40, 7.4 miles west of Ludlow, San Bernardino County, California during the period of December 20, 1997 to December 22, 1997, and nine months later during the period of September 27, 1998 to September 29, 1998. The field data collected during these periods included photographic records documenting the overcrossing site, experimental setups, visible abutment/superstructure damage, modal data derived from the excitation of the structure, and wave propagation data at selected locations on the superstructure and abutments. The intent of this appendix is to document measured wave propagation field data and present a corresponding stiffness analysis.

C.2 Theory

The analysis presented here is an adaptation of the work by Lin and Sansalone (1997) who developed a methodology to determine P-wave speed in concrete pavements using measurements of Rayleigh waves (R-waves). Direct measurement of P-wave speed in pavements and abutment walls is hampered by an inability to accurately measure the thickness of these structural elements. The characteristic frequency exhibited by impulse-echo methods which rely on reflections of the wave front is directly affected by variation in thickness and errors in its measurement. This limitation led Lin and Sansalone (1997) to develop an indirect method of P-wave speed that does not rely on knowledge of

material thickness. Once the Rayleigh wave speed is measured P-wave and dynamics modulus can be determined for the structural element.

If a concrete deck, abutment wall or similar planar element is treated as a semi-infinite elastic solid, the relationship between the R-wave speed (C_R) to P-wave speed (C_P) is given by the equation (Sansalone and Carino 1986):

$$C_P = \frac{1+\nu}{0.87+1.12\nu}\sqrt{\frac{2(1-\nu)}{(1-2\nu)}}C_R \tag{C.1}$$

Using a value of 0.18 for Poisson's ratio for concrete reduces Eq. (C.1) to

$$C_p = 1.76C_R \tag{C.2}$$

R-wave speed can be determined using the following relation if the distance, L, between two sensors and the R-wave arrival time, t1 and t2, at each sensor is known:

$$C_R = \frac{L}{t_2 - t_1} \tag{C.3}$$

The elastic modulus is related to P-wave speed by the following relation (Kolsky 1963):

$$E = \rho C_p^2 \tag{C.4}$$

Where E and ρ are, respectively, Young's modulus and the concrete mass density. This relation is used to calculate the elastic modulus of the structure under study.

C.3 Wave Speed Measurements

Two sets of wave speed measurements were obtained for the structure. A preliminary set using the 1997 modal test setup was used for preliminary testing in December 1997. A specialized test setup was developed for the September 1998 test period and an extensive set of Rayleigh wave measurements were taken on the superstructure and abutments.

C. 3.1 December 1997 Test Period

Wave propagation data were collected from the north abutment below the superstructure. A five-channel setup was used to record a wave front passing through the abutment at approximately 5.3 ft. intervals along the wall. Figure C.1 is a layout of the

accelerometer placement on the wall. The wave front was induced with an impact hammer striking the wall approximately 1.9 ft. to the right of accelerometer N4. The modal setup was used in this testing, however the sampling frequency was increased to 2000 Hz per channel. Results of this investigation are shown in Figure C.2. Table C.1 summarizes the results of these measurements, and speeds indicated in the table are characteristic of Rayleigh wave speeds. The severe dispersion of the wave front as it passed through the abutments made the determination of arrival time difficult. These results led to development of a better test setup designed specifically for arrival time measurements. This instrumentation was used in the September 1998 test period.

C.3.2 September 1998 Test Period

Rayleigh wave speeds at twenty-four locations on the superstructure, abutments, and column were investigated. Five impulse-response measurements were made using dual sensors spanning each location. Incremental arrival times and the related material properties are reported later in this section.

Field Instrument Setup for September 1998 Test Period

Two high-frequency pressure sensors designed for arrival time measurements, PCB 132A30 Microsensors, were attached to concrete surfaces approximately 12 inches apart. A Rayleigh wave was generated with a small hardened-steel impactor and the arrival of the wave was recorded with a dual channel 50 MHz Fluke 90B Scopemeter. The fast response of the scopemeter and high-pass filtering of the pressure sensor made arrival time measurements and the corresponding time interval between measurement points relatively easy to determine. Arrival time was taken as first major positive peak in the wave pulse train. Figure C.3 depicts typical dual channel response measurements of a wave.

Wave Propagation Analysis for September 1998 Test Period

Measurements of time interval over a 12 inch distance are presented in Table C.2. The corresponding wave speeds and elastic modulus are also reported. Review of these results indicates significant deterioration in the concrete properties of the abutments and

column. The low elastic modulus in these locations indicate significant deterioration. The average superstructure modulus for the deck rail was 3,400 ksi; for four points on the superstructure near the abutments, the average was 3,450 ksi. The north abutment averaged 2,650 ksi while the south abutment averaged 2,850 ksi. Two points near the column base averaged 3,025 ksi.

C.4 Summary

Review of testing reported here indicates that it is possible to acquire wave speed data of sufficient resolution to accurately determine the modulus of concrete box-girder structures. The results of the wave speed analysis, in general, support the findings reached in this report.

- The results indicated relatively low modulus readings throughout the structure, particularly in the abutments.
- This measurement technique worked well for measurement of wave speeds.
- Automation of the process and a more comprehensive review of instrumentation would probably improve results further.

Table C.1 Preliminary wave speed analysis (1997)

Location	Time (ms)	Distance (ft)	Average Speed (ft/s)	Incremental Speed (ft/s)
N4	.329	1.9	5770	5770
N3	.955	7.23	7570	8520
N2	1.65	12.56	7630	7700
N1	2.34	17.89	7650	7700

Table C.2 Wave speed analysis computations (1998)

Inspection Location	Average Interval Time	STD *u*sec	Average R-wave Speed Ft/sec	P-wave Speed Ft/sec	Dynamic Modulus Psi
E12 Deck Rail	146.7	2.68	6815	11995	3723572
E10 Deck Rail	163.2	4.15	6127	10784	3009871
E8 Deck Rail	164.1	2.97	6093	10725	2976603
E6 Deck Rail	159.3	4.00	6277	11047	3158292
E4 Deck Rail	150.3	2.28	6652	11707	3547201
E2 Deck Rail	141.6	2.61	7062	12429	3998174
NE Super	151.6	2.97	6596	11609	3488107
NW Super	149.2	2.28	6702	11796	3601228
N Abutment 1	178.4	4.10	5605	9865	2518828
N Abutment 2	146.0	2.83	6849	12055	3760820
N Abutment 3	189.6	5.18	5274	9283	2230034
N Abutment 4	198.0	2.83	5051	8889	2044833
N Abutment 5	158.8	1.10	6297	11083	3178976
N Abutment 6	175.6	3.85	5695	10023	2599796
N Abutment 7	182.0	10.68	5495	9670	2420168
SE Super	159.6	2.61	6266	11028	3147186
SW Super	149.6	2.61	6684	11765	3581995
S Abutment 1	146.4	0.89	6831	12022	3740297
S Abutment 2	194.8	1.79	5133	9035	2112566
S Abutment 3	280.8	1.79	3561	6268	1016703
S Abutment 4	167.2	2.68	5981	10526	2867581
S Abutment 5	171.6	1.67	5828	10256	2722411
S Abutment 6	152.8	4.15	6545	11518	3433535
S Abutment 7	140.4	2.61	7123	12536	4066811
Column South Face	156.4	4.10	6394	11253	3277289
Column East Face	170.0	5.83	5882	10353	2773897

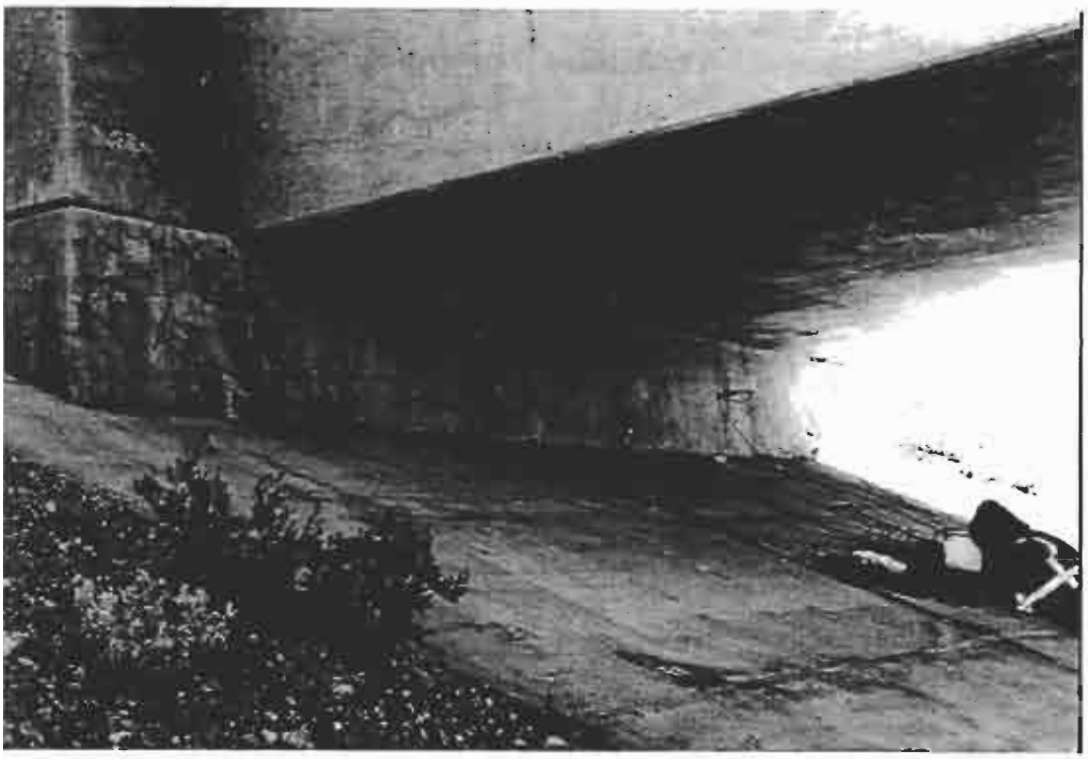

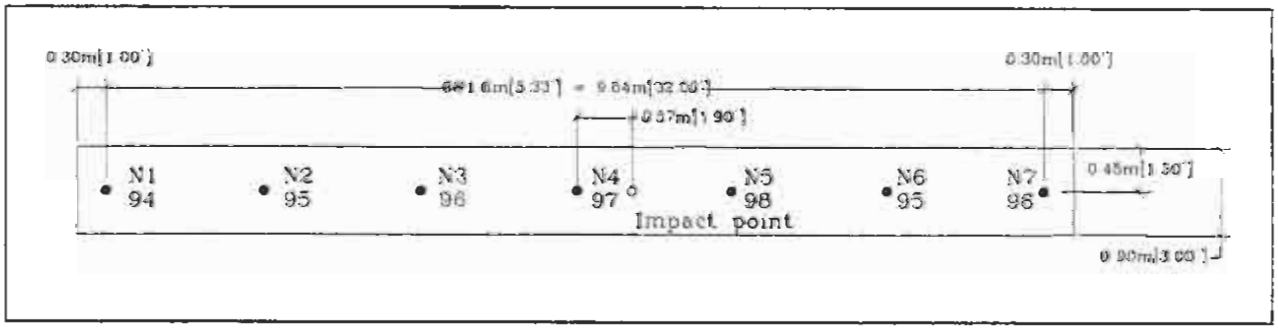

Figure C.1 Accelerometer layout on north abutment wall

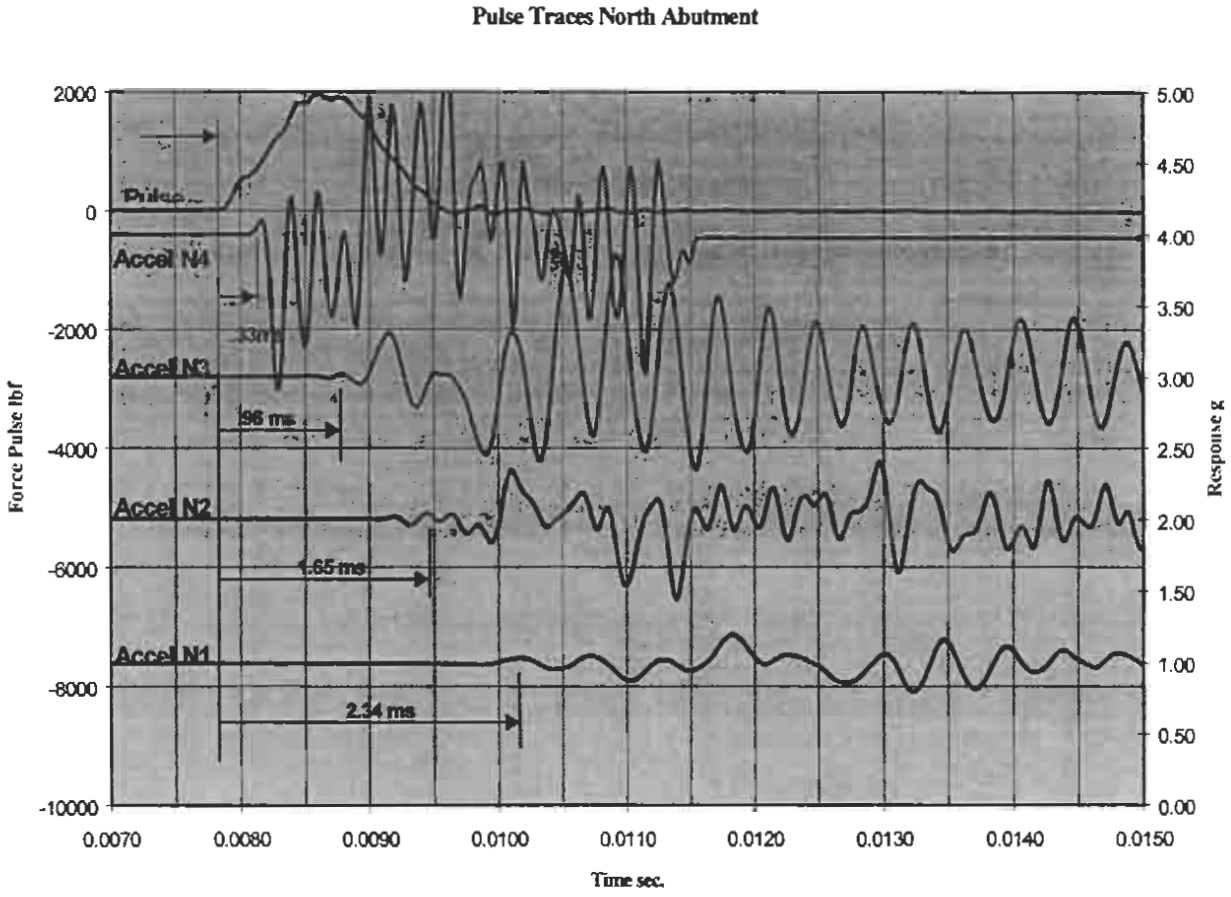

Figure C.2 Wave front times for accelerometers N1 through N4

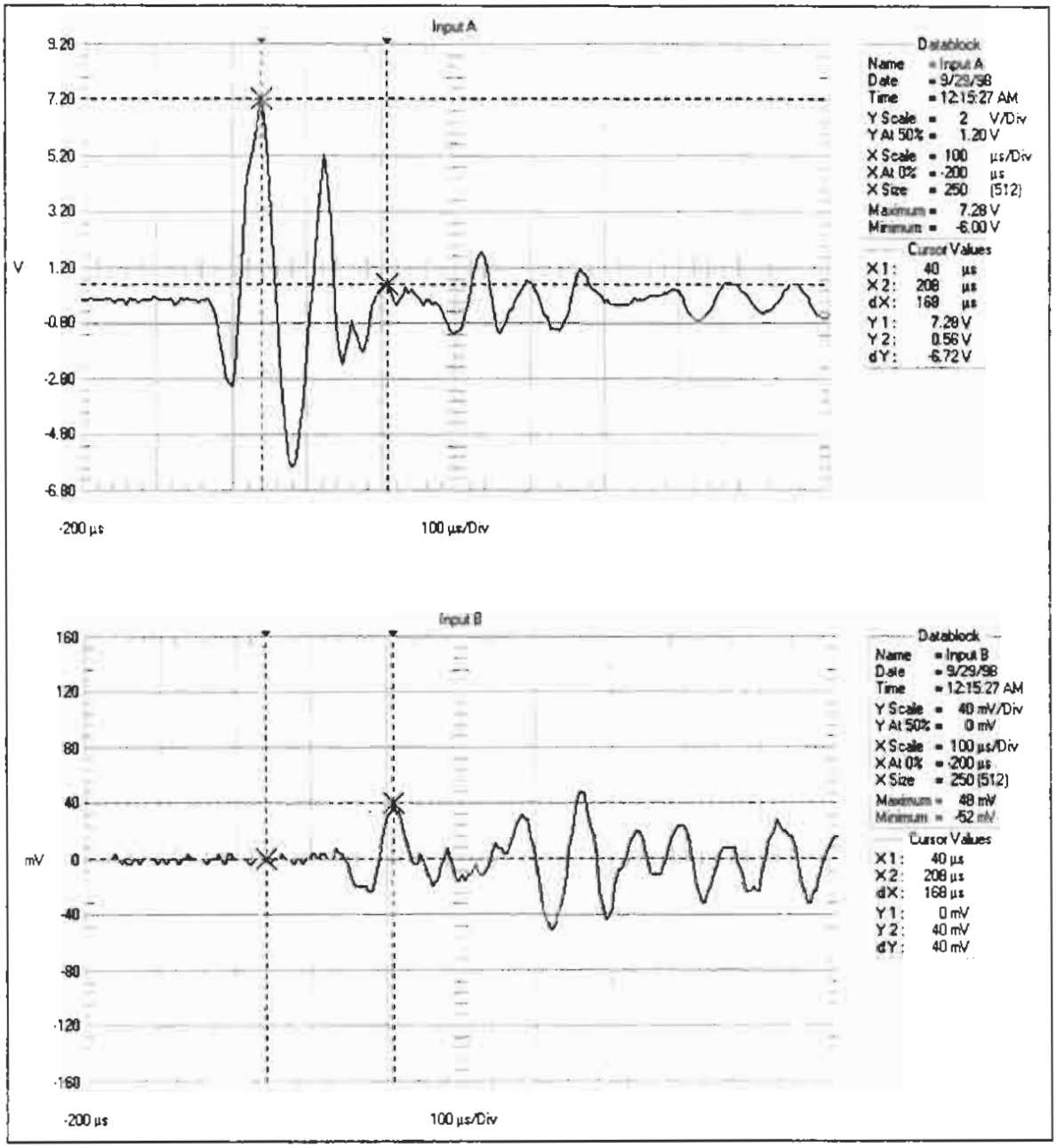

Figure C.3 Typical pulse response of PCB Microsensors